

# Multiscale Toughening Mechanisms in Biological Materials and Bioinspired Designs

Wei Huang, David Restrepo, Jae-Young Jung, Frances Y. Su, Zengqian Liu, Robert O. Ritchie, Joanna McKittrick, Pablo Zavattieri, and David Kisailus\*

Biological materials found in Nature such as nacre and bone are well recognized as light-weight, strong, and tough structural materials. The remarkable toughness and damage tolerance of such biological materials are conferred through hierarchical assembly of their multiscale (i.e., atomic-to macroscale) architectures and components. Herein, the toughening mechanisms of different organisms at multilength scales are identified and summarized: macromolecular deformation, chemical bond breakage, and biomineral crystal imperfections at the atomic scale; biopolymer fibril reconfiguration/deformation and biomineral nanoparticle/nanoplatelet/nanorod translation, and crack reorientation at the nanoscale; crack deflection and twisting by characteristic features such as tubules and lamellae at the microscale; and structure and morphology optimization at the macroscale. In addition, the actual loading conditions of the natural organisms are different, leading to energy dissipation occurring at different time scales. These toughening mechanisms are further illustrated by comparing the experimental results with computational modeling. Modeling methods at different length and time scales are reviewed. Examples of biomimetic designs that realize the multiscale toughening mechanisms in engineering materials are introduced. Indeed, there is still plenty of room mimicking the strong and tough biological designs at the multilength and time scale in Nature.

## 1. Introduction

Throughout human history, engineers have been developing structural materials where strength and toughness are vital properties for performance in multiple applications.<sup>[1]</sup> It has been known that these two materials properties are usually mutually exclusive.<sup>[2]</sup> The strength of a material is defined as its ability to withstand a certain load without plastic deformation or failure, while material toughness is the total amount of energy absorption during its deformation until failure or fracture occurs.<sup>[3]</sup> Toughness can be also defined using fracture mechanics methodologies as the stress intensity factor required to initiate and propagate a crack which will lead to the final fracture of a material.<sup>[2]</sup> This toughness is also known as fracture toughness, which is a material property.<sup>[4]</sup> Stronger materials such as ceramics tend to have limited plastic deformation, which will cause high stress concentrations and finally lead to material fracture. Thus, materials with higher

Dr. W. Huang, Prof. D. Kisailus  
Department of Chemical and Environmental Engineering  
University of California Riverside  
Riverside, CA 92521, USA  
E-mail: david@engr.ucr.edu

Prof. D. Restrepo, Prof. P. Zavattieri  
Lyles School of Civil Engineering  
Purdue University  
West Lafayette, IN 47907, USA

Prof. D. Restrepo  
Department of Mechanical Engineering  
The University of Texas at San Antonio  
San Antonio, TX 78249, USA

Dr. J.-Y. Jung, Dr. F. Y. Su, Prof. J. McKittrick  
Materials Science and Engineering Program  
University of California San Diego  
La Jolla 92093, USA

Prof. Z. Liu, Prof. R. O. Ritchie  
Department of Materials Science and Engineering  
University of California Berkeley  
Berkeley, CA 94720, USA

Prof. Z. Liu  
Materials Fatigue and Fracture Division  
Institute of Metal Research  
Chinese Academy of Sciences  
Shenyang 110016, China

Prof. J. McKittrick  
Department of Mechanical and Aerospace Engineering  
University of California San Diego  
La Jolla 92093, USA

Prof. D. Kisailus  
Materials Science and Engineering Program  
University of California Riverside  
Riverside, CA 92521, USA

 The ORCID identification number(s) for the author(s) of this article can be found under <https://doi.org/10.1002/adma.201901561>.

DOI: 10.1002/adma.201901561

strength are likely to be brittle, while weaker materials are easy to deform, and thus much tougher.<sup>[2]</sup> In our traditional view of making a desired material that is tough and damage tolerant, it is crucial to reach a compromise of the strength and ductility. However, Nature has developed several remarkable ways to build lightweight and strong, yet tough materials over millions of years of evolution.<sup>[4–6]</sup> **Figure 1a** depicts toughness as a function of elastic modulus, highlighting that naturally existing biological materials retain toughness with an increase in stiffness (green banana curve); while the current synthetic engineering materials show an inverted curve (yellow), indicating toughness drops dramatically as stiffness increases. Even though natural materials exhibit modest material properties compared with the engineering materials, they tend to achieve a better trade-off. This significant difference primarily stems from the hierarchical structure of biological materials and their associated multiscale toughening mechanisms.

Unlike synthetic materials, biological materials have had to develop very select architectures due to the limited selection of elements and restricted growth environments. Furthermore, these structures are constructed via well-orchestrated bottom-up synthesis processes, yielding hierarchical structures with organized building blocks architected from the atomic to macroscale level.<sup>[1b,7]</sup> The subsequent hierarchical structures and features found in these biological materials that were determined to contribute to the toughness of materials has been summarized in previous studies as intrinsic and extrinsic toughening mechanisms.<sup>[2,8]</sup> For example, in bone, the intrinsic toughening mechanism works ahead of the crack tip, including features from atomic to nanoscale, such as molecular uncoiling, fibrillar sliding, and microcracking. While the extrinsic toughening mechanisms are located behind of the crack tip; these include fibril bridging and crack deflection and twisting, which are at larger length scales (micro- to macroscale) compared to intrinsic mechanisms.<sup>[9]</sup> As a result, the fracture toughness of bone is almost 10 times higher than its component hydroxyapatite



**Wei Huang** is a postdoctoral researcher in Prof. David Kisailus's Biomimetic and Nanostructured Materials Laboratory at the University of California, Riverside. He received his Ph.D. from the materials science and engineering program of the University of California, San Diego. His research focuses on impact resistant and struc-

tural biological materials as well as bioinspired designs of advanced materials.



**David Kisailus** is the Winston Chung Endowed Chair of Energy Innovation and Professor in Materials Science and Chemical and Environmental Engineering at the University of California, Riverside. He is a Kavli Fellow of the National Academy of Sciences and directs a Multi-University Research Center focused on

bioinspired impact resistant materials. His "Biomimetic and Nanostructured Materials Laboratory" investigates synthesis/structure/property relationships in biological composites and nanomaterials to develop advanced materials for structural, energy and environmental-based technologies.

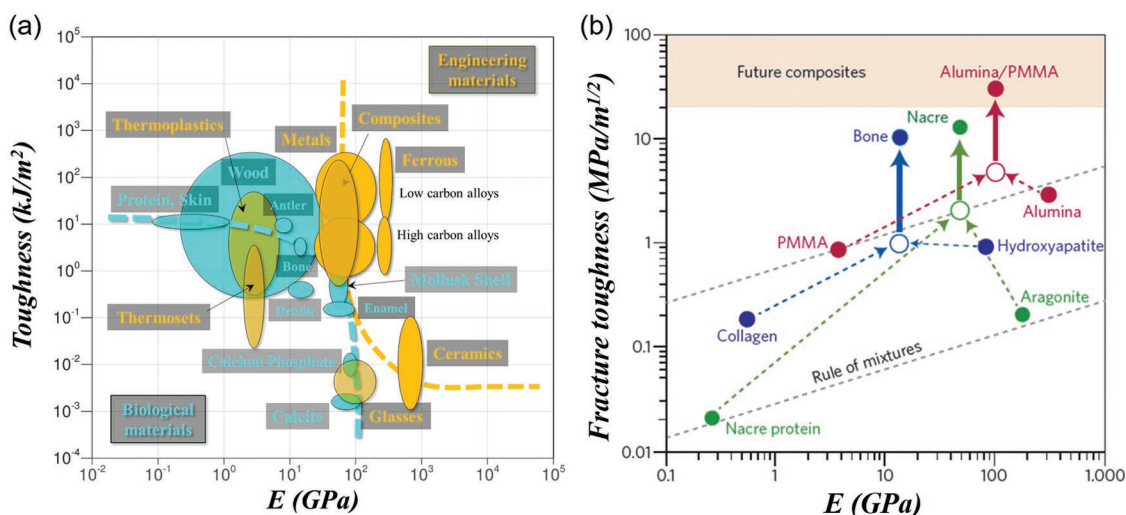


**Figure 1.** Toughness of natural and engineering materials. a) Ashby plot of toughness and elastic modulus of biological and engineering materials. These biological materials show high stiffness, but at the same time retain toughness. b) Significant increases in toughness are realized by materials from nature such as bone and nacre, by applying different design strategies and toughening mechanisms. b) Adapted with permission.<sup>[5a]</sup> Copyright 2015, Springer Nature.

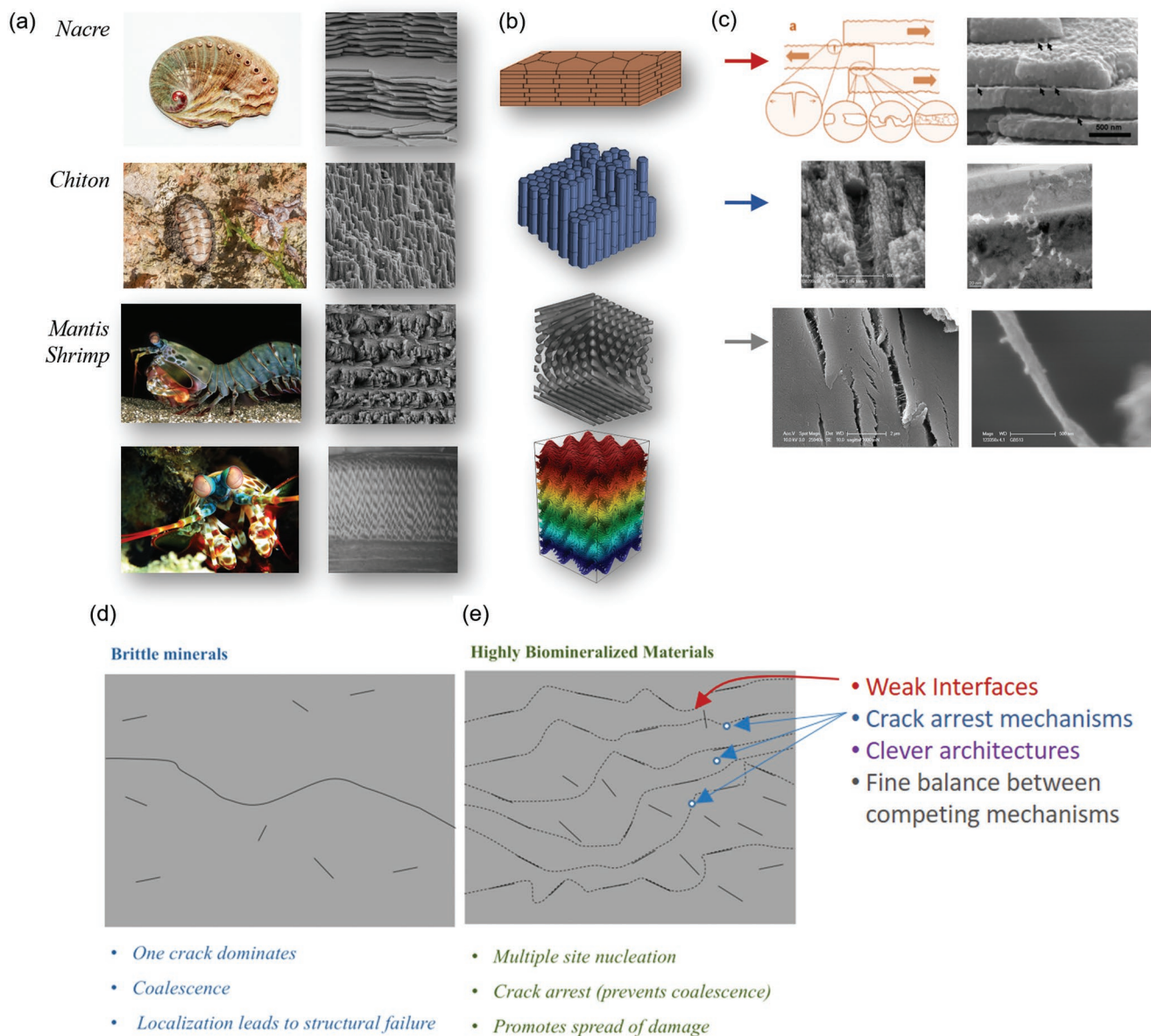


**Figure 2.** a) Naturally occurring architectures found in the shells of abalones, teeth of chitons, and the dactyl clubs of the mantis shrimp, b) simplified schematics of architectures from (a), c) relatively weaker interfaces and bridges found in some of these architectures, d) schematic depicting typical brittle crack behavior in brittle materials (i.e., minerals), e) crack behavior found in biomineralized composite materials. a) The left images for “Nacre” and “Chiton” are from Pixabay. Right image for “Chiton”: Reproduced with permission.<sup>[10b]</sup> Copyright 2009, Elsevier. Mantis shrimp images (top row, left and right): Reproduced with permission.<sup>[14a]</sup> Copyright 2012, American Association for the Advancement of Science. Mantis shrimp (bottom row, left and right) and bottom image in (b): Reproduced with permission.<sup>[70]</sup> Copyright 2016, Wiley-VCH. c) Top row: Reproduced with permission.<sup>[10f]</sup> Copyright 2009, Elsevier. Middle row: Reproduced with permission.<sup>[74]</sup> Copyright 2014, Wiley-VCH.

nanocrystals.<sup>[5a]</sup> Some of the recent work has been focused on heavily biomineralized systems such as those in **Figure 2a,b**. In most cases, these systems have a very high content of mineral, are known for their brittle mechanical behavior, and yet, it is found that these materials contain an important population of features that otherwise act as stress concentrators. These features are channels/pore canals, relatively weaker interfaces, defects, and all of types of flaws that otherwise will lead to the stress localization. For instance, **Figure 2c** shows that nacre and chiton<sup>[10]</sup> have weaker interfaces with mineral bridges that hypothetically modulate their interfacial strength. This

is contrary to what it is expected in what is otherwise a material that has a high content of very brittle material. **Figure 2d** illustrates the expected behavior of a monolithic brittle material: given a population of defects, once an external tensile load is applied, some of the defects will grow into microcracks and, eventually, one crack will dominate the behavior of the material leading to catastrophic failure. However, highly biomineralized materials show an entirely different behavior: while it is true that the materials contain defects and other sources of stress concentrators, the underlying architecture and presence of relatively weaker interfaces provide a robust template

for multiple cracks to initiate, grow (without coalescence), and still promote multiple initiation sites for more microcracks (Figure 2e).<sup>[11]</sup> These architectures provide a template of relatively weaker interfaces for crack initiation (i.e., local softening) and arrest (local hardening), which in turn, promotes other cracks to nucleate and grow. This leads to delocalization and helps spread the damage to vast regions, improving the toughness of the material. The general behavior of the material typically is a product of competing mechanisms that maximize energy dissipation and stress alleviation through the synergistic roles of the architecture and interfaces.

Indeed, experimental observations at different length scales have provided a plethora of useful information on how the different features synergistically work toward some beneficial behavior of the material. In turn, these observations, carefully examined, lead to a well-thought hypothesis on what key mechanisms are active during a specific type of loading condition.

Utilizing experimental observations is critical in revealing multistructural features and mechanical properties, while modeling becomes an important tool to provide insight toward the most likely explanation of how these structures might lead to some specific emerging behavior. In this regard, a model is nothing else than a group of ingredients that a researcher put together to best describe the behavior of the material to validate such hypotheses. Subsequently, these ingredients can be selectively turned on and off to carry out systematic and parametric analyses.

Beyond computational modeling, additive manufacturing methods are being developed to help validate these models as well as translate key mechanistic insights to scalable and manufacturable engineered products. Based on an understanding of some of the toughening mechanisms at different length scales in biological materials (such as bone and nacre), researchers have been utilizing fabrication methods such as freeze casting and 3D printing of synthetic engineering materials to mimic biological architectures and thus replicate their toughening mechanisms.<sup>[12]</sup> The brick-and-mortar lamellar structure found in nacre was successfully adapted using  $\text{Al}_2\text{O}_3$  and poly(methyl methacrylate) (PMMA) components to form a synthetic ceramic composite by freeze casting. The toughness of the final product was more than 300 times that of its constituents, indicating the efficiency of the toughening mechanisms discovered in natural biological composites (Figure 1b).<sup>[12a]</sup> Thus, there has been a significant increase in motivation to applying the toughening mechanisms found in natural organisms to synthetic material systems to create damage-tolerant materials.

When referring to the mechanical properties of materials, the loading strain rate (how fast the load is applied to a material's surface) is also a crucial factor that can affect the material behavior (i.e., toughness and damage tolerance).<sup>[13]</sup> A vivid illustration from a textbook shows the difference of material behavior at different loading rates: a sandbag used by the soldiers can stop bullets with the flow of sand, while it can be easily destroyed by a knife; a metal plate can stop a sharp knife, but can never withstand the penetration of a high-speed bullet.<sup>[13b]</sup> Interestingly, Nature has also evolved materials and structures that are sufficiently tough while demonstrating the ability to withstand forces under a very broad range of strain rates: from quasi-static ( $\approx 10^{-3} \text{ s}^{-1}$ ) to high-speed impact ( $\approx 10^4 \text{ s}^{-1}$ ).

The impacting speed of the dactyl clubs in mantis shrimp can reach  $\approx 20 \text{ m s}^{-1}$ , which leads to a loading strain rate of  $\approx 10^4 \text{ s}^{-1}$ .<sup>[14]</sup> The intraspecies flying speed of bighorn sheep is  $\approx 9 \text{ m s}^{-1}$ , and it can cause an impact strain rate  $\approx 10^2\text{--}10^3 \text{ s}^{-1}$ .<sup>[15]</sup> Conversely, bones and teeth face quasi-static loads and fatigue (strain rate  $\approx 10^{-3} \text{ s}^{-1}$ ). Unlike the high strain rate impacts, many quasi-static loads are continuous forces whose durations are for relatively long time periods of time.<sup>[16]</sup> In this case, investigating the toughening and energy dissipation mechanisms in natural materials at different time scales (loading rates) will give us further insights and inspiration toward the design of impact and fatigue resistant engineering materials.

Here, we identify and summarize a range of architectural features and toughening mechanisms that exist in mineralized and nonmineralized biocomposites at multiple length scales and at different time scales. The organisms and structures subsequently described can be seen in **Figure 3** and **Table 1**. The features and toughening mechanisms in different organisms are identified in four proposed length scales, which will be discussed as follows:

- Atomic-scale (<1 nm): Natural materials often contain both mineralized and nonmineralized components. Macromolecules such as chitin, cellulose, collagen, keratin (and other proteins) as well as water molecules will contribute to the toughness at the atomic scale through chemical bonds and molecular deformation. Crystal imperfections in nanocrystals within mineralized tissues, especially those introduced under high strain rates, will also contribute to the energy dissipation.
- Nanoscale (1 nm to 1  $\mu\text{m}$ ): Nanoscale biominerals (e.g., isotropic particles, anisotropic rods, and platelets) are the primary strengthening features of mineralized tissues at the nanoscale. Polymer fibrils and amorphous polymer matrices comprise the nonmineralized components. Toughening mechanisms such as fibril bridging and reorientation as well as particle rotation at this level will also be identified. Additional toughening mechanisms included are found at the interfaces between these nanoparticles.
- Microscale (1  $\mu\text{m}$  to 1 mm): Architectural designs and features such as lamellar, cellular, gradient, tubular, Bouligand/herringbone structures observed at this length scale can serve in toughening and energy dissipating roles. Crack deflection, twisting and reorientation at different loading rates will be discussed. Modeling work on crack stopping and arresting mechanisms will also be introduced.
- Macroscale (>1 mm): The size of entire organisms or their structures are at this length scale. They are usually combinations of different materials and structures with specific designs (i.e., morphologies and shapes), which are integrated for toughening and energy dissipation purposes. Based on the loading nature of specific organisms/structures: mantis shrimp dactyl club, woodpecker beak, antler, and bighorn sheep horn are placed among the high-speed impact materials. Wood, nacre, and hooves are exposed to relatively lower-speed impacts. Structures such as bone, tooth, fish scales are usually under quasi-static loading. The material composition and organism morphology at the macroscale will be investigated in terms of energy dissipation purposes.

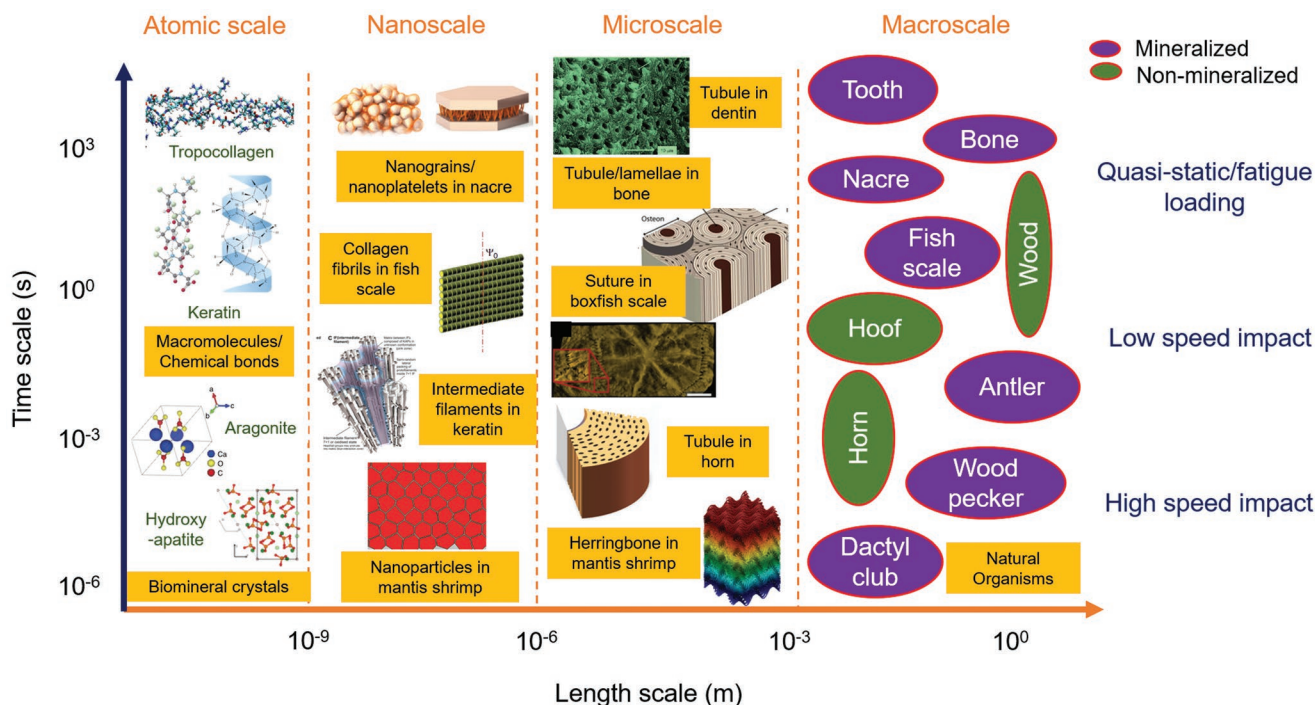


**Figure 3.** Multiscale features of biological materials. At the macroscale, natural organisms under different loading environment are classified. Tubular, lamellar, suture, and herringbone structure are features of organisms at the microscale. At the nanoscale, nanograins, nanoplates, polymer fibrils are found. Biopolymer macromolecules and mineral crystal domains provide the main building blocks of biological composite materials at the atomic scale. Atomic scale images: Tropocollagen: Reproduced with permission.<sup>[100a]</sup> Copyright 2013, Springer Nature. Keratin: Adapted with permission.<sup>[27b]</sup> Copyright 2015, Elsevier. Aragonite and hydroxyapatite: Adapted with permission.<sup>[154a]</sup> Copyright 2009, Elsevier. Nanoscale images from top to bottom: Nacre: Adapted with permission.<sup>[5a]</sup> Copyright 2014, Springer Nature. Fish scale: Adapted with permission.<sup>[62]</sup> Copyright 2013, Springer Nature. Keratin: Adapted with permission.<sup>[28]</sup> Copyright 2017, Elsevier. Mantis shrimp: Adapted with permission.<sup>[70]</sup> Copyright 2016, Wiley-VCH. Microscale images: Tubule in dentin: Adapted with permission.<sup>[154a]</sup> Copyright 2009, Elsevier. Tubule/lamellae in bone: Adapted under the terms of the CC-BY Creative Commons Attribution 4.0 International License (<http://creativecommons.org/licenses/by/4.0/>).<sup>[154c]</sup> Copyright 2016, Springer Nature. Suture in boxfish scale: Adapted with permission.<sup>[90a]</sup> Copyright 2015, Elsevier. Herringbone in mantis shrimp: Adapted with permission.<sup>[70]</sup> Copyright 2016, Wiley-VCH.

Researchers have also been developing new multiscale models and bioinspired methods to mimic the multiscale structures and have realized the toughening mechanisms

in synthetic materials.<sup>[12a,17]</sup> We believe a thorough summary of the toughening mechanisms at multiple length and time scales will lead to the development of strong, tough and

**Table 1.** Compositions, structures, and loading features of different organisms.

Organism	Composition	Feature at microscale	Feature at nanoscale	Loading condition	Reference
Mantis shrimp dactyl club	Chitosan/calcium phosphate minerals	Bouligand/gradient/herringbone	Chitin fibrils/HAP nanoparticles	Impact $\approx 20 \text{ m s}^{-1}$ , strain rate $\approx 10^4 \text{ s}^{-1}$	[14,70]
Woodpecker beak	Keratin/hydroxyapatite	Lamellar/cellular	Keratin intermediate filaments and amorphous matrix	Impact $\approx 7 \text{ m s}^{-1}$	[87]
Bighorn sheep horn	Keratin	Lamellar/tubular	Keratin intermediate filaments and amorphous matrix	Impact $\approx 9 \text{ m s}^{-1}$ , strain rate $\approx 10^3 \text{ s}^{-1}$	[15,32,33,92]
Horse hoof	Keratin	Lamellar/tubular	Keratin intermediate filaments and amorphous matrix	Impact $\approx 3\text{--}4 \text{ m s}^{-1}$ , strain rate $\approx 10^2 \text{ s}^{-1}$	[64,158]
Antler	Collagen/hydroxyapatite	Lamellar/tubular/cellular	Collagen fibrils/hydroxyapatite nanoplatelets	Impact $\approx 11 \text{ m s}^{-1}$ , strain rate $\approx 10^3 \text{ s}^{-1}$	[77–79b]
Wood/bamboo	Cellulose/lignin	Lamellar/cellular	Cellulose fibrils	Impact or static load	[44b,45,66b,157]
Nacre/shell	Aragonite/calcite/Protein	Lamellar	Calcite nanograins	Impact or static load	[10a,47a,c,d,71b,72b,73]
Fish scales	Collagen/hydroxyapatite	Bouligand	Collagen fibrils	Static load	[61b,c,62,90a]
Bone	Collagen/hydroxyapatite	Lamellar/tubular/cellular	Collagen fibrils/hydroxyapatite nanoplatelets	Continuous/ fatigue	[9a,16,76]
Tooth	Collagen/hydroxyapatite/magnetite	Tubular	Hydroxyapatite nanorods/nanoparticles	Continuous/ fatigue	[10b,53a,74,75,88,89b]

impact resistant synthetic materials in a more efficient way. By identifying the toughening mechanisms and features in Nature and comparing them with the current state of bioinspired work, this current review will be able to shed light on the future directions toward fabricating bioinspired strong and tough materials for both impact and fatigue resistance applications.

## 2. Atomic Scale

Materials utilized by natural systems are fabricated from a limited selection of elements due to the environment in which they are synthesized (i.e., aqueous solution, ambient temperature and pressure, near-neutral pH).<sup>[7]</sup> As a result, the primary organic components at the atomic and molecular scales include: collagen, cellulose, lignin, chitin, keratin, and other proteins. Similarly, inorganic constituents are primarily limited to calcium, iron and silicon-based minerals (e.g., calcium carbonates, calcium phosphates, iron oxides, silicas). These organic macromolecules and inorganic mineral phases display different behavior under different loading conditions (loading strain rate, loading mode: tension or compression). Their specific deformation and toughening mechanisms will confer the toughness to larger length scales.

### 2.1. Biopolymer Macromolecules, Orientation, Confirmation, and Chemical Bonds

#### 2.1.1. Collagen

Collagen has been considered as one of the most abundant structural proteins in many biological organisms, particularly in mammals. It is the main constituent of bone, skin, cartilage, tendon, and many organs of mammals.<sup>[18]</sup> These tissues show remarkable toughness, with a significant contribution from collagen.<sup>[19]</sup> Among the different types of collagen in the human body, type I collagen is one of the most important and deeply studied, as it is the main component of bones and skin.<sup>[19]</sup> Bone is a nanocomposite material formed from hydroxyapatite nanocrystals templated by and formed within collagen fibers.<sup>[5a,20]</sup> The relative rigid hydroxyapatite cannot dissipate much energy to keep bone from fracturing under impact, and thus, the soft collagen fibrils play an important role in the energy absorption. At the molecular level, type I collagen is mainly formed by glycine, proline, alanine and hydroxyproline amino acids. The primary sequence is arranged such that well-ordered  $\alpha$ -helix secondary structures are formed. Three of these  $\alpha$ -helix strands twist together to form a tropocollagen structure (Figure 4a)<sup>[18b]</sup> that is  $\approx 1.6$  nm in diameter and 300 nm in length. Finally, tropocollagen is subsequently arranged in a staggered formation and assembled to yield collagen fibrils with a characteristic gapping band  $\approx 67$  nm, which can be easily identified through transmission electron microscopy (TEM) imaging.<sup>[18a]</sup> Due to the molecular arrangement and interactions of collagen molecules with other materials such as hydroxyapatite mineral platelets in a specific environment,

toughening mechanisms of collagen at the molecular level were reported.<sup>[21]</sup> Figure 4b shows a load–displacement curve of a short tropocollagen molecular chain ( $\approx 8.5$  nm) under tension.<sup>[21]</sup> It was reported that interchain hydrogen bonds exist and act to stabilize the conformation of the triple-helix structure.<sup>[22]</sup> The sawtooth-like load-displacement curve is indicative of the breaking and reforming of hydrogen bonds between polypeptide chains, which suggests a potential energy dissipation mechanism for tropocollagen under tension. A typical load displacement curve of a collagen fibril is shown in Figure 4c.<sup>[23]</sup> Starting from a flat toe region, the collagen molecules undergo uncoiling and uncrimping. This is followed by a load increasing region (heel), in which the molecular chains start straightening and sliding. Reconfiguration of molecular chains occurs in these two regions.<sup>[1b,23]</sup> As the load increases, collagen fibrils show reversible elastic and irreversible plastic deformation, including breakage of crosslinked bonds and fibrils.<sup>[23]</sup> Since the uncoiling of collagen molecules has been described as one of the main energy dissipation mechanisms at the molecular scale, more details regarding the sacrificial bonds discovered by previous studies need to be addressed.<sup>[24]</sup> Sacrificial bonds in organic molecular networks are defined as bonds that are weaker than, and can therefore be broken before, those within the main structural backbone.<sup>[24a,25]</sup> A hidden length exists within the molecular chains, and can be stretched after the breakage of these sacrificial bonds, contributing to the toughness of the organic materials. Figure 4d shows possible calcium-mediated sacrificial bonds in bones: the connection between two polymer fibrils, two binding sites on one fibril, binding between hydroxyapatite plates within a collagen fibril.<sup>[26]</sup> The amount of energy dissipation of collagen fibrils with calcium-mediated sacrificial bonds can be four times larger than those without sacrificial bonds. A force-displacement plot indicates the extra toughness increased by the sacrificial bonds and the stretch of the hidden lengths after the breakage of sacrificial bonds (Figure 4d).<sup>[25]</sup>

#### 2.1.2. Keratin

In addition to collagen, keratin is another abundant structural protein-based biopolymer found in Nature, and is among one of the toughest known biological materials (based on the Ashby plots).<sup>[4]</sup> It is produced in epithelial cells that are found in, for example, hair, horns, hooves, feathers, and skin. Two crystalline phases exist: crystalline  $\alpha$ - or  $\beta$ -keratin, and are embedded in an amorphous keratin matrix.<sup>[27]</sup> Figure 4e shows the typical molecular structures of  $\alpha$ - and  $\beta$ -keratins.  $\alpha$ -keratin has a helical structure with a rotational periodicity of 0.51 nm, while  $\beta$ -keratin shows a sheet-like structure with a periodicity of 0.31 nm between the residues along the molecular chain.<sup>[27b]</sup> Figure 4f illustrates the arrangement of crystalline keratin intermediate filaments (IFs, composed of  $\alpha$ - or  $\beta$ -keratin coiled coils) embedded in an amorphous matrix.<sup>[28]</sup> The crosslinking bonds in these molecules are both weak hydrogen bonds, which are formed between amino and carboxy groups and water molecules as well as strong disulfide bonds (Figure 4g).<sup>[29]</sup> As one of the main toughening mechanisms found in keratin at the molecular scale, water molecules

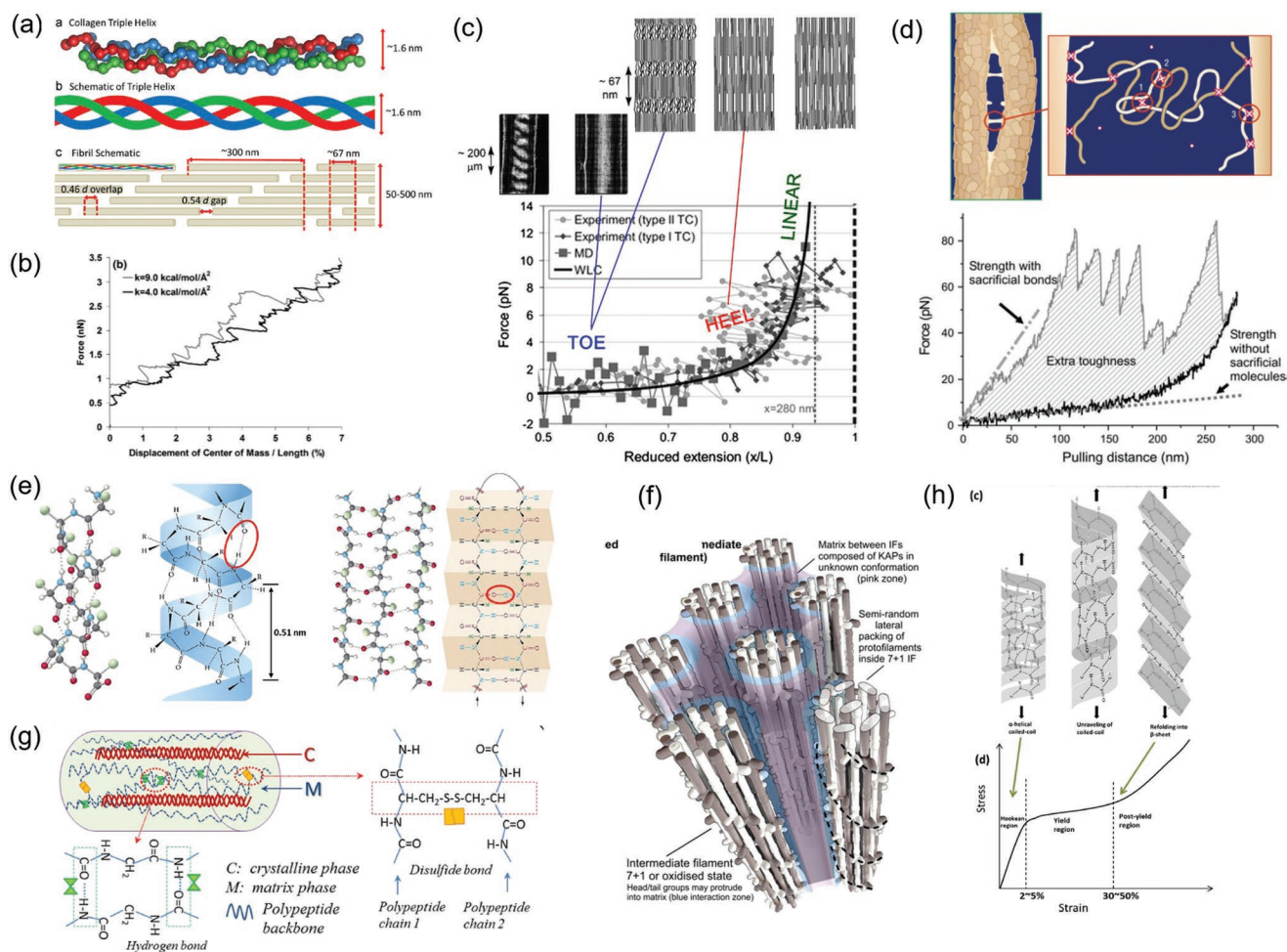


**Figure 4.** Collagen and keratin molecular structures and toughening mechanisms. a) The tropocollagen structure of collagen. Adapted with permission.<sup>[18b]</sup> Copyright 2015, Elsevier. b) Force–displacement curve of an  $\approx 8.5$  nm tropocollagen chain under tension, displaying a zigzag shape indicating of intermolecular hydrogen bonds breaking and reforming. Adapted with permission.<sup>[21]</sup> Copyright 2011, American Society of Civil Engineers. c) A typical stress–strain curve of collagen with a toe region, in which collagen molecules are straightening and uncoiling. As the force increases, chains start sliding and stretching. Ultimately, inelastic deformation such as fibril breakage occurs. Adapted with permission.<sup>[23]</sup> Copyright 1998, Elsevier. d) Sacrificial bonds between collagen fibrils and hydroxyapatite nanoplatelets. Extra toughness is gained from the breakage of sacrificial bonds and stretching of the hidden length features within fibrils. Upper image in (d): Adapted with permission.<sup>[25]</sup> Copyright 2006, Elsevier; Lower image in (d): Adapted with permission.<sup>[26]</sup> Copyright 2005, Springer Nature. e) Molecular structure of two crystalline forms of keratin:  $\alpha$ -helix and  $\beta$ -sheet. Adapted with permission.<sup>[27b]</sup> Copyright 2016, Elsevier. f) Crystalline keratin intermediate filaments embedded within an amorphous matrix. Adapted with permission.<sup>[28]</sup> Copyright 2017, Elsevier. g) Hydrogen and disulfide bonds between crystalline chains and within the amorphous matrix. Adapted with permission.<sup>[29]</sup> Copyright 2016, Springer Nature. h) Typical stress–strain curves of keratin fibrils under tension, showing the  $\alpha$ - to  $\beta$ -keratin phase transformation. Adapted with permission.<sup>[27b]</sup> Copyright 2016, Elsevier.

could break and reform hydrogen bonds in the amorphous matrix, thus increasing the plasticity as well as the energy dissipation.<sup>[29,30]</sup> It was found that water reduced the stiffness of an oryx horn from 6.1 to 1.8 GPa after hydration.<sup>[31]</sup> Tomblato et al. showed the compressive yield strength and elastic modulus decreased significantly after full hydration.<sup>[32]</sup> Tensile tests of wet horns showed 60% tensile strain before failure, which is far greater than 5% in dry horns. Under a tensile strain rate as high as  $1000\text{ s}^{-1}$ , the strain can reach 70% in wet horns compared with less than 5% strain in dry horns.<sup>[33]</sup> Thus, water as a second phase in keratin can increase the plasticity of the amorphous matrix, thus making the whole structure more energy absorbent.<sup>[34]</sup>

Phase transformations from the  $\alpha$  to  $\beta$  phase occurs when keratin fibers, such as hair and wool, undergo large tensile deformations (Figure 4h).<sup>[27b,35]</sup> This phase transformation is the main energy absorption mechanism for keratin materials under tension. Based on the significant differences in molecular structures, the mechanical behavior of the crystalline keratin and amorphous matrix are very different. The IF can be stretched 2.5-fold, indicating high extensibility due to its coiled-coil nanostructure. The amorphous keratin matrix is rich in proteins with cysteines that provide stiffness due to the strong disulfide bonds.<sup>[35a,36]</sup> As a result, this nanostructure can provide both stiffness as well as toughness by changing the number ratio of IFs in the amorphous matrix.

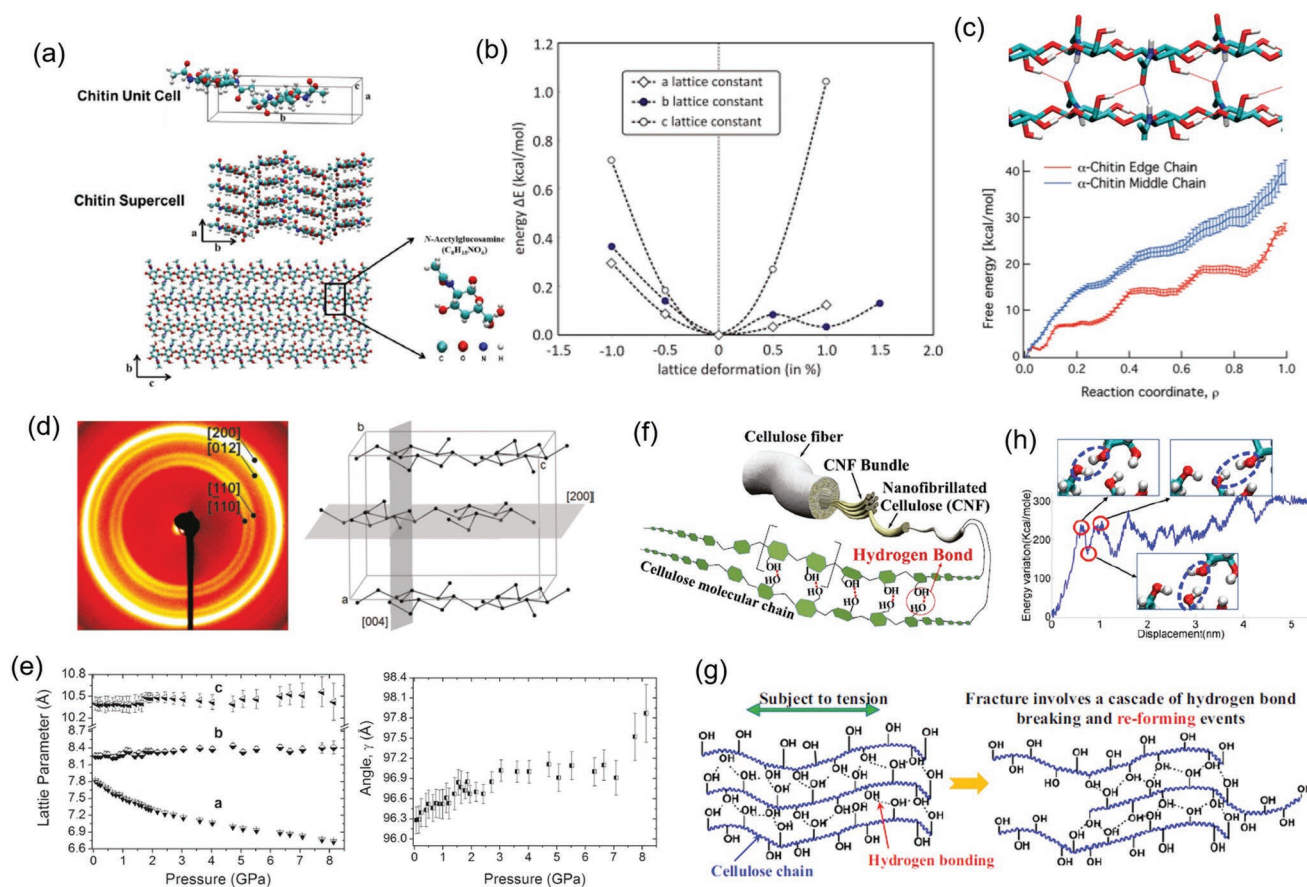


**Figure 5.** Molecular structure and toughening mechanisms of cellulose and chitin macromolecules. a) Structure of the chitin unit cell and molecular chains. Adapted with permission.<sup>[41]</sup> Copyright 2015, Elsevier. b) Strain energy as a function of crystal deformation in different orientations. Adapted with permission.<sup>[42]</sup> Copyright 2011, Elsevier. c) Bifurcated hydrogen bonds between chitin chains. Free energy as a function of reaction coordinate (decrystallization degree), indicating that the “peeling off” of the middle chain needs higher energy. Adapted with permission.<sup>[43]</sup> Copyright 2011, American Chemical Society. d) X-ray diffraction of the cellulose crystal and cellulose unit cell. e) Lattice parameters  $a$ ,  $b$ ,  $c$  and the monoclinic angle  $\gamma$  as a function of pressure, indicating deformation of chitin unit cells. d,e) Adapted with permission.<sup>[45]</sup> Copyright 2011, American Chemical Society. f) Hydrogen bonds between cellulose molecular chains. g) Breaking and reforming of hydrogen bonds between cellulose chains under tension. h) Energy as a function of displacement of cellulose molecular chains, indicating breaking and reforming of hydrogen bonds. f–h) Adapted with permission.<sup>[46b]</sup> Copyright 2015, National Academy of Sciences.

### 2.1.3. Chitin

Chitin is a structural, polysaccharide-based biopolymer mainly found in cell walls in fungi as well as the exoskeletons of arthropods, such as insects and crustaceans.<sup>[37]</sup> It is one of the most ubiquitous polysaccharides in Nature.<sup>[38]</sup> As the main component of defense armor in most insects and crustaceans, chitin has a high fracture toughness that is comparable to natural materials such as bone.<sup>[5b,39]</sup> Chitin can be found in three polymorphic forms:  $\alpha$ ,  $\beta$ , and  $\gamma$ .<sup>[40]</sup> The basic unit of these crystals is  $\beta$ -1,4-*N*-acetyl-D-glucosamine (GlcNAc) ((C<sub>8</sub>H<sub>13</sub>O<sub>5</sub>N)<sub>n</sub>).<sup>[38b]</sup> The polymer chains in  $\alpha$ -chitin have an antiparallel arrangement (Figure 5a), while  $\beta$ -chitin have a parallel arrangement.  $\gamma$ -chitin crystals have both parallel and antiparallel assemblies.<sup>[41]</sup> In this review, we will focus on  $\alpha$ -chitin as it is the most abundant form found in Nature. Due to its molecular arrangements,  $\alpha$ -chitin shows anisotropic mechanical properties. Figure 5b is a plot showing the energy associated with the deformation of the crystals

in different directions.<sup>[42]</sup> Molecular dynamic simulations show that the stiffness in the  $c$ -axis is almost an order of magnitude higher than the other two axes, which is likely due to covalent bonding within molecular chains along the  $c$ -axis, and hydrogen bonding in the  $a$  and  $b$  axes. In addition, hydroxymethyl –CH<sub>2</sub>OH side groups located along the  $a$ -axis can form rotational conformers and induce intra- and intermolecular hydrogen bonds. This could provide energy dissipation mechanisms at the atomic scale in crystalline  $\alpha$ -chitin molecules.<sup>[42]</sup> However, further experimental studies are needed to verify these suggested mechanisms. In terms of the hydrogen bonding configuration between  $\alpha$ -chitin molecule chains, Beckham et al. reported bifurcated hydrogen bonds between the layers of chains.<sup>[43]</sup> (See Figure 5c, where the blue and red dashed lines indicate the bifurcate hydrogen bonds.) It is also verified that due to these interlayer hydrogen bonds, it is harder (needs higher energy) to “peel” off the middle chains (i.e., core chains) than chains on the sides of the structure (Figure 5c).<sup>[43]</sup> As a tough and strong biological material in Nature, the

breakage of hydrogen bonds with different conformations in chitin could provide a potential for energy dissipation.

#### 2.1.4. Cellulose

Cellulose is the main component of cell walls of plants, providing structural support to different plant organisms. Similar to keratin, cellulose fibers consist of crystalline and amorphous domains.<sup>[44]</sup> Materials made from cellulose such as wood show promising mechanical properties (toughness and stiffness) based on Ashby plots and have been used as structural components for millennia.<sup>[5b]</sup> The molecular structure of cellulose is a chain-like structure formed by hundreds to thousands of  $\beta(1,4)$  linked D-glucose units  $((C_6H_{10}O_5)_n)$ .<sup>[44a]</sup> Figure 5d shows the X-ray diffraction pattern of crystalline cellulose and a schematic of the unit cell of cellulose crystals, highlighting the (200) and (004) planes.<sup>[45]</sup> Researchers have investigated the toughening mechanisms of cellulose fibers at a molecular scale using X-ray diffraction and Raman spectroscopy. The molecular chains remain stable under high compressive pressure (8 GPa), while the relative position of different chains (i.e., the (002) planes) are displaced, indicating a distortion of cellulose chains under shear stress. Figure 5e shows the lattice parameter,  $a$ , decreases and the monoclinic angle,  $\gamma$ , changes abruptly at a pressure of  $\approx 8$  GPa, verifying the distortion of cellulose chains. This shear distortion of (002) planes is plastic and unrecoverable, and is thus considered as an energy dissipation mechanism at the molecular scale.<sup>[45]</sup>

In addition to energy absorption mechanisms provided by the molecular crystal structure, hydrogen bonds were also found to contribute to the toughness of cellulose nanofibrils at the molecular scale.<sup>[46]</sup> Figure 5f shows the hydrogen bonds between the molecular chains of cellulose nanofibrils. Under tensile loading, the hydrogen bonds between the molecular chains are breaking and reforming because of the sliding between adjacent chains (Figure 5g). Figure 5h demonstrates the potential energy as a function of the displacement of the molecular chains. As the hydrogen bonds (blue circle) stretch to the furthest position under tension, the potential energy increases to the first peak. The hydrogen bonds are then broken and relocated to a new site, forming a new bond, at which the potential energy decreases to the first trough. This process occurs repeatedly until the molecular chain was pulled out, corresponding to the zigzag shape of the potential energy curve in Figure 5g.<sup>[46b]</sup>

## 2.2. Biomineral Crystals Deformations and Imperfections

### 2.2.1. Calcite and Aragonite

In many strong and tough biological materials, biopolymers usually provide ductility and toughness, while most of the strength and stiffness come from integration of biominerals. The Young's modulus of biominerals such as calcite and hydroxyapatite can reach  $\approx 100$  GPa, while most structural biopolymers are in the range of  $\approx 1$ –10 GPa.<sup>[5a]</sup> Interestingly, although biominerals cannot dissipate a large amount of energy through molecular reconfiguration or breaking of chemical bonds and reforming (as most biopolymers do), researchers

found other energy absorption mechanisms in the mineral crystals while under compression or impact.<sup>[47]</sup>

As one of the most well-studied research topics in the biological and bioinspired materials fields, mollusk shells provide strong and tough armor. Their primary constituent is calcium carbonate ( $CaCO_3$ ), with a small fraction of biopolymer.<sup>[8,48]</sup> There are three crystal polymorphs of calcium carbonate found in Nature: calcite (rhombohedral), aragonite (orthorhombic), vaterite (hexagonal), as well as amorphous mineral. Figure 6a shows the basic components of nacre (mother of pearl): aragonite nanoplatelets with thickness of  $\approx 500$  nm, and a diameter of  $\approx 5$ –10  $\mu m$ . The nanoplatelets are composed of  $\approx 30$  nm nanograins glued together by biopolymers.<sup>[5a]</sup> Toughening mechanisms at the atomic scale were reported by a previous study indicating that the imperfections in the nanocrystals introduced by high strain rate impact could dissipate energy thus increasing the strength and toughness. Partial dislocations (Figure 6b), deformation twinning (Figure 6c), and amorphization (Figure 6d) were observed in nacre nanocrystals through high-resolution TEM (HRTEM) after high strain rate ( $\approx 10^3$  s<sup>-1</sup>) impacts using a split-Hopkinson pressure bar (SHPB).<sup>[47d]</sup> Interestingly, these crystal imperfections only existed in samples under high strain rate impact and were not generated after quasi-static compression.

Another effective natural armor, the shell of the bivalve *Placuna placenta*, also composed of calcium carbonate (calcite polymorph) shows almost an order of magnitude higher energy dissipation density than single-crystal geological calcite.<sup>[10d,47a]</sup> Similar to nacre, the shell of *P. placenta* is composed by layers of elongated diamond-shaped calcite crystals with a thickness  $\approx 300$  nm. Each nanoplatelet is a single crystal with the [108] planes facing the outer surface of the shell (Figure 6e). Nanoindentation was performed to study the energy dissipation mechanisms at the nano- and atomic scales (Figure 6f). Deformation twinning, misoriented nanocrystals as well as amorphization were observed in the plastic deformation zone (Figure 6g).<sup>[47a]</sup> Different from the *P. placenta*, growth twinning was found in the *Strombus gigas* conch shells.<sup>[47c]</sup> The crossed-lamellar hierarchical structure of aragonite platelets and TEM imaging of growth nanotwins are shown in Figure 6h. Figure 6i plots the crack tip opening displacement (CTOD) as a function of crack extension under in situ TEM fracture toughness testing. The CTOD in the natural conch is much larger than single crystal aragonite, indicating that a blunt and plastic deformation occurs in conch shell, while the single crystal aragonite is undergoing brittle fracture. The extra toughness observed in conch shell is due to the pre-existing nanotwins, which was verified to initiate and form multiple nanocracks at the crack tip, thus blocking the primary crack propagation. Also, nanograin rotation as well as amorphization were found in the plastic zone under indentation (Figure 6j).<sup>[47c]</sup> The toughening mechanisms such as deformation twinning, dislocation and amorphization at the atomic scale were also reported in engineering ceramics such as alumina, zirconia, and boron carbide.<sup>[49]</sup>

### 2.2.2. Hydroxyapatite

Hydroxyapatite ( $Ca_{10}(PO_4)_6(OH_2)$ ) (HA) is another prevalent natural occurring mineral. It is the main component of bone

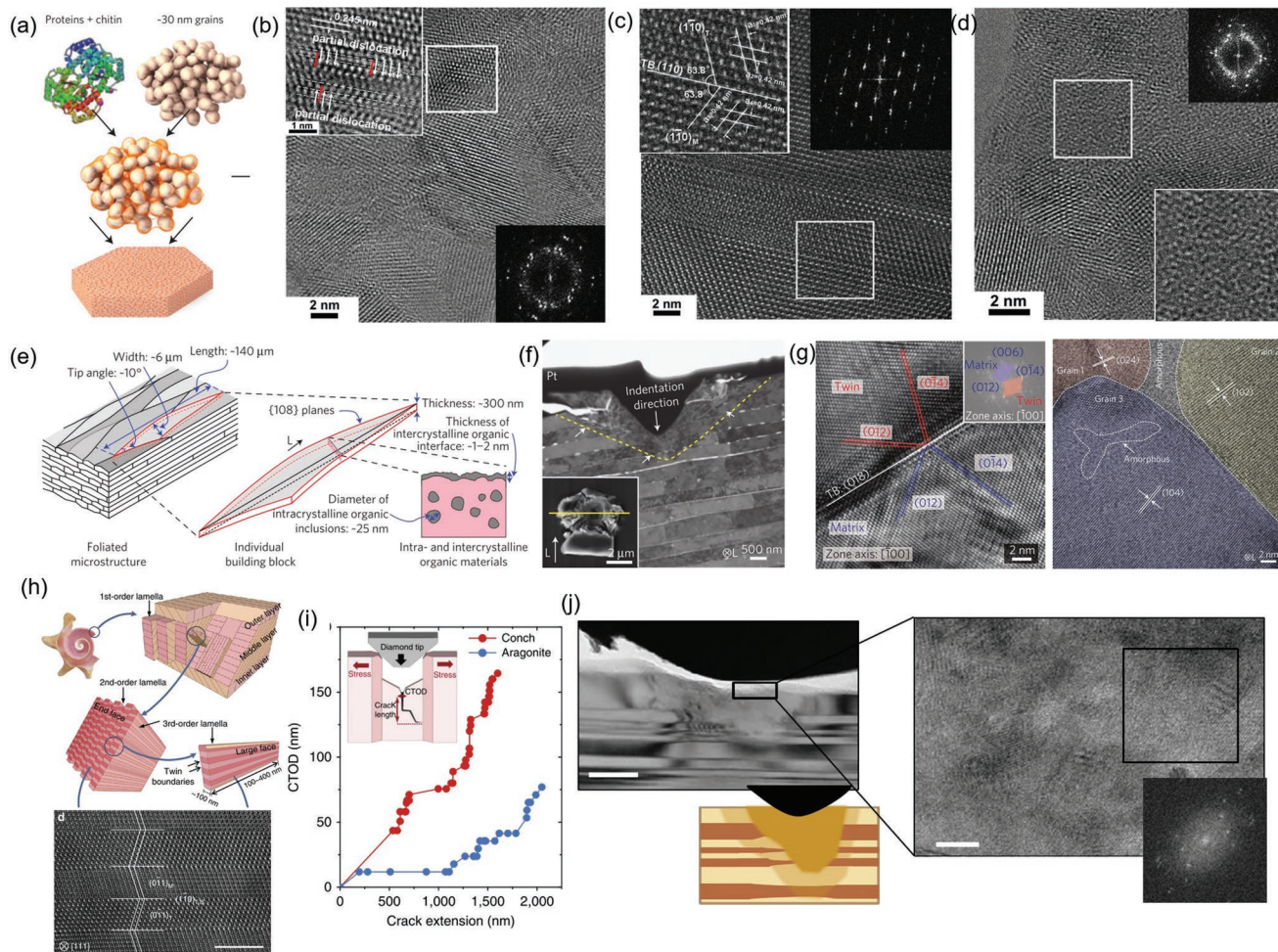


**Figure 6.** Atomic scale deformation and toughening mechanisms in calcium carbonate biominerals. a) Nanograins and the polymer matrix in the nanoplatelets of nacre. b) Dislocations, c) nanotwinning, and d) amorphization in nacre after high strain rate impacts with split-Hopkinson pressure bar (SHPB). e) Nanostructure of the bivalve, *Placuna placenta*, shell. f) TEM micrograph after a nanoindentation test on the *P. placenta* shell. g) Deformation twinning, amorphization and misorientation of nanocrystals in the plastic zone caused by nanoindentation. h) Lamellar structure and growth twinning in *Strombus gigas* conch shells. i) Plot of the crack tip opening displacement as a function of crack extension in conch and single crystal aragonite, indicating the fracture resistance in conch shell is higher than that in the single crystal aragonite. j) Amorphization in the plastic zone after indentation on conch shell surface. a–d) Adapted with permission.<sup>[47d]</sup> Copyright 2011, Springer Nature. e–g) Adapted with permission.<sup>[47a]</sup> Copyright 2014, Springer Nature. h–j) Adapted with permission.<sup>[47c]</sup> Copyright 2016, Springer Nature.

and teeth.<sup>[5a]</sup> in which collagen molecules were found as a scaffold assisting the formation of hydroxyapatite nanocrystals.<sup>[50]</sup> Most of the toughness in bone is contributed by the collagen phase, while the energy dissipation or deformation mechanisms of hydroxyapatite nanocrystals remains unknown.<sup>[2,8]</sup> Hydroxyapatite has a hexagonal crystal structure.<sup>[51]</sup> Anisotropy of mechanical properties of hydroxyapatite single crystals were identified by previous studies.<sup>[52]</sup> The *c*-axis ([0001] direction) shows the highest stiffness and yield strength, which corresponds to the loading orientation in bones. Plastic deformation of single crystals was noticed by nanoindentation experiments on both basal (0001) and prismatic (1010) planes, indicating energy dissipation could occur within HA crystals.<sup>[52b,c]</sup> Displacement burst, pile up, and crushed slip steps provide direct evidence of plastic deformation under indentation.<sup>[52b]</sup> The fracture toughness acquired by nanoindentation was 0.65 MPa m<sup>1/2</sup>

in prismatic planes ([1010] direction), compared to only 0.4 MPa m<sup>1/2</sup> in basal planes ([0001] direction). Thus, HA crystals do have some degree of ductility, which could provide energy dissipation in biological materials such as bones and teeth.<sup>[52b]</sup> It will be of great interest to investigate the deformation and energy dissipation mechanism of HA nanocrystals in bones and teeth under compression or impact, which will complement knowledge of the current toughening mechanisms of bones and teeth at the atomic scale.

### 2.2.3. Magnetite, Goethite, and Silica

Unlike calcium carbonate and apatite, magnetite (Fe<sub>3</sub>O<sub>4</sub>), goethite (FeOOH), and silica (SiO<sub>2</sub>·*n*H<sub>2</sub>O) are biominerals that exist in specific organisms but are less widespread. These minerals afford

more specific function, such as providing wear resistance in chiton and limpet teeth, and enabling toughness and flexibility in sea sponges.<sup>[10b,53]</sup> Apart from acting as a navigation sensor in the skulls of tuna, pigeons and some bacteria, magnetite (which has a cubic inverse spinel structure and octahedral crystal morphology) is the hardest biomineral found in Nature. Besides functioning as a compass for bacteria (chain like magnetite nanoparticles found in a bacterial, *Magnetospirillum magnetotacticum*<sup>[54]</sup>), it is especially purposed for chiton teeth, which are used to grind on rock to access food. The hardness and elastic modulus of these teeth can reach 12 and 175 GPa, respectively, which are three times higher than those of hydroxyapatite in enamel and aragonite in nacre.<sup>[10b]</sup> Multiple twin structures were identified in magnetite. It would be of interest to know how the crystal morphology as well as crystal twins affect the resulting hardness and toughness. Toughening mechanisms of magnetite at the atomic scale need to be further investigated. Similar to magnetite, goethite also has a high hardness and stiffness, which are comparable with magnetite. Researchers reported that the limpet tooth, mainly consisting of goethite, had a tensile strength of 4.9 GPa, which is higher than the 4.5 GPa of the strongest spider silk.<sup>[53b]</sup>

Silica is mainly found in diatoms and sea sponges.<sup>[53c,55]</sup> The silica precipitation and biosilicification process has been studied by researchers and chitin as well as collagen were found as templates in the mineralization.<sup>[56]</sup> Highly flexible spicules of the marine glass sponge *Rossella fibulata* has been reported.<sup>[57]</sup> The basic constituents of these spicules are organic fibers (either chitin or protein) and amorphous silica nanoparticles.<sup>[58]</sup> It was shown that silica nanoparticles were embedded in the crystalline organic chitin matrix.<sup>[57]</sup> It was proposed that the silica nanoparticles bind with chitin fibers through hydrogen bonds.<sup>[57]</sup> However, the size of silica nanoparticles ( $\approx 50\text{--}200$  nm in diameter) is much larger than the characteristic size of ceramic materials ( $\approx 10\text{--}30$  nm) that could be insensitive to defects and thus flaw tolerant.<sup>[53c]</sup> The flexibility and toughness of silica glass sponges are attributed to their hierarchical structure based on previous studies.<sup>[53c,59]</sup> The toughening mechanisms of silica and the interaction bonds with the organic matrix at the atomic scales remain unknown. Additionally, the mix of different minerals (multiphases) such as calcite, aragonite, and silica were found in some species of marine sponges, which may yield novel toughening mechanisms that needs further investigation.<sup>[60]</sup>

### 3. Nanoscale

Features at the nanoscale are the basic assembly units of molecules and minerals: polymer macromolecules tend to form crystalline fibrils or amorphous matrices, while the mineral component (amorphous, nanocrystalline, single crystalline) can be synthesized as nanoparticles, nanoplatelets, nanorods, or form a continuous amorphous matrix around these fibers. The viscoelastic properties and interactions within and between fibrils of biopolymer will provide toughness to organisms with polymer-rich structures. In addition, these organic structures often have functionality beyond mechanical support: they can be modified or coupled with other chemically modified organics that are used as scaffolds to template the synthesis and assembly of mineral. These mineral nanoparticles,

nanoplatelets, and nanorods usually act as structural supports because of their high stiffness and strength. The redistribution and reorientation of the mineralized phases are additional toughening mechanisms found in mineralized tissues.

#### 3.1. Biopolymer Fibrils and Matrices

##### 3.1.1. Straightening, Reorientation, and Stretching of Collagen Fibrils

Nanoscale toughening mechanisms of collagen fibrils including fibril rotating, straightening, sliding, and bridging of the constituent nanofibrils have been reported in various biological structures such as skin, fish scales, and bones.<sup>[61]</sup> Figure 7a shows the deformation and failure of rabbit skin, with an edge notch, loaded under uniaxial tension. Cracks did not propagate through the skin sample but just opened up, indicating the tear resistance of skin. The SEM micrographs and schematic illustrate the different deformation mechanisms of collagen fibrils in skin under tensile loading (Figure 7b). Fibrils initially rotate (I), straighten (II), but then undergo stretching, sliding and delamination (III), and finally fracture (IV).<sup>[61a]</sup> The reorientation of fibrils under tensile loading was examined by in situ synchrotron small-angle X-ray diffraction (SAXS). SAXS is an efficient technique that detects the orientation and tensile strain on the collagen fibrils.<sup>[62]</sup> Similarly, researchers have been applying in situ SAXS methods to study the deformation mechanisms of collagen fibrils in coelacanth scales.<sup>[61c]</sup> The diffraction pattern of collagen is shown in Figure 7c, which is the result of the helicoidal arrangement of collagen fibrils. Figure 7d is a plot of the fibril strain as a function of the azimuthal angle, indicating the actual fibril strain is different in different orientations. The fibril strain is the largest in the loading direction, and decreases to 0% at an angle of  $\approx 40^\circ$ , indicating all the deformation in this direction is fibril sliding. The collagen fibrils are also found reorienting along the loading direction.<sup>[61c]</sup> The toughening mechanisms of collagen fibrils at the nanoscale are summarized in Figures 7e–i. Curved and entangled collagen fibril bundles are first straightened and separated into individual collagen fibril under tensile loads. Interfibrillar gaps and fibril lamellae rotation occurred at the same time. Rotation and stretching of individual fibrils, which occur until fracture, are also energy dissipation mechanisms.<sup>[61a,62]</sup>

The deformation and mechanical behavior of mineralized collagens such as those in bone are different from the nonmineralized types found in the aforementioned skins and scales.<sup>[61d,63]</sup> Similarly, the toughening mechanisms of mineralized collagen fibrils are also different. Wide-angle X-ray diffraction (WAXD) and SAXS were applied by Gupta et al. to characterize the strain on hydroxyapatite nanoplatelets and collagen fibrils in antler. The plastic deformation and energy dissipation of antler under tension were contributed by the intrafibrillar debonding of the mineral and collagen interface. The different strains observed in the mineral and collagen suggested friction and sliding between the two different phases, which has not been found in unmineralized collagens.<sup>[61d]</sup> Hang and Barber used atomic force microscopy (AFM) to test the tensile properties of collagen fibrils in antler.<sup>[63]</sup> In the antler samples, areas with different degrees of mineralization were determined based on the back-scattering scanning

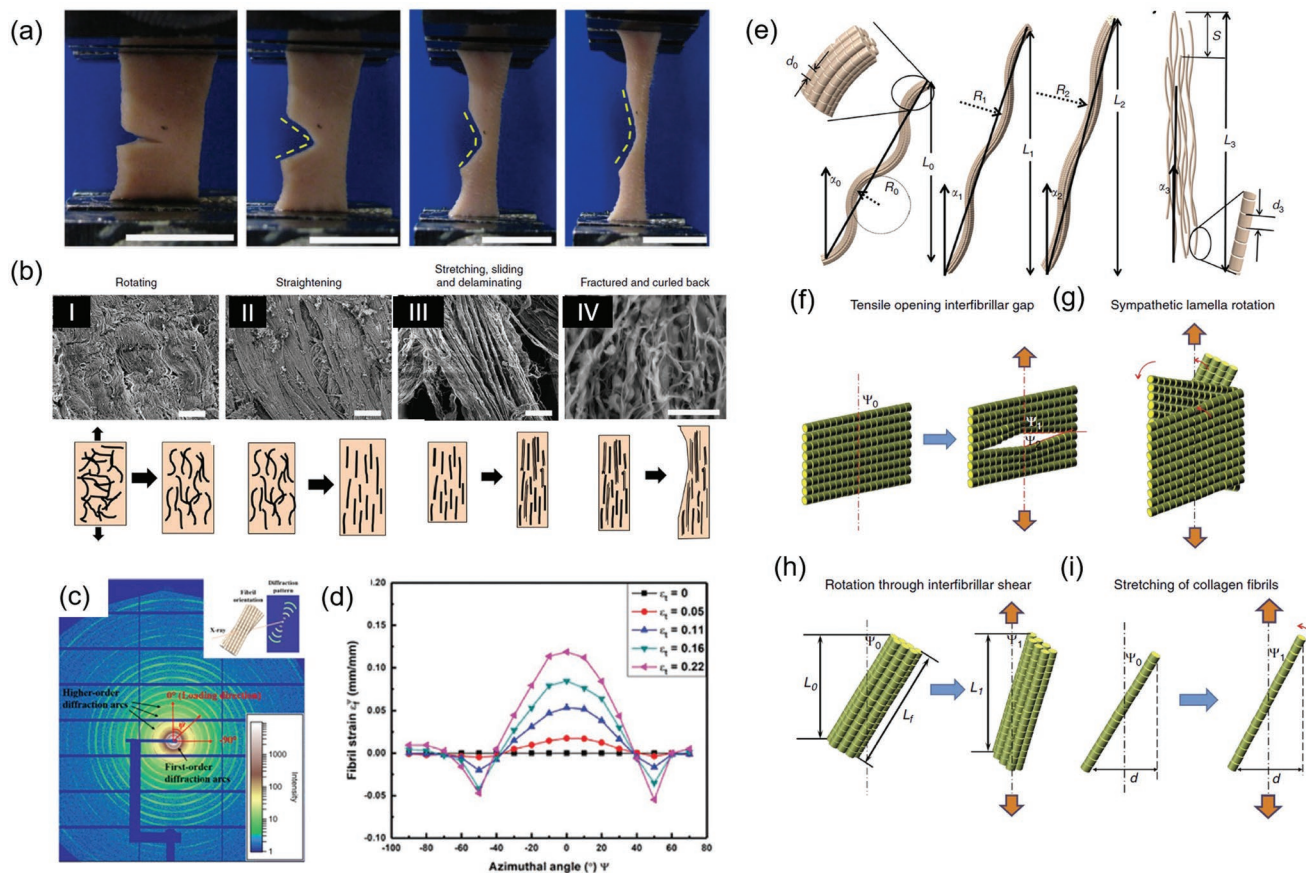


**Figure 7.** Toughening mechanisms of collagen fibrils in skin and fish scales. a) Uniaxial tension of a single edge notched rabbit skin sample, showing cracks opening up, but not propagating through the sample. b) SEM micrographs and schematics showing fibril deformation: I, fibril rotation; II, fibril straightening; III, fibril stretching, sliding and delamination; IV, fibril fracture. c) A typical SAXS pattern of coelacanth scales with a double Bouligand arrangement of collagen fibrils. d) Fibril strain as a function of the azimuthal angle of collagen fibrils under uniaxial tension. e–i) schematic of toughening mechanisms of collagen fibrils: e) straightening and uncoiling of collagen fibrils; f, g) delamination and lamellae rotation; h, i) rotation and stretching of an individual fibril. a, b, e) Adapted with permission.<sup>[61a]</sup> Copyright 2015, Springer Nature. c, d) Adapted with permission.<sup>[61c]</sup> Copyright 2018, Wiley-VCH. f–i) Adapted with permission.<sup>[62]</sup> Copyright 2013, Springer Nature.

electron microscopy (SEM). In samples with greater mineral content, collagen fibrils undergo uncoiling first, followed by an increase in stiffness due to the stress transfer by the minerals. While in samples with less mineral content, sliding of fibrils decrease the stiffness and increase the fracture strain.<sup>[63]</sup> Thus, the tensile behavior and deformation mechanisms of collagen fibrils are highly dependent on the degree of mineralization.

### 3.1.2. Crack Deflection in Keratin Intermediate Filaments and Amorphous Matrices

Keratin materials consist of crystalline IFs ( $\approx 7\text{--}10\text{ nm}$ ) and an amorphous matrix.<sup>[27b]</sup> The structure and mechanical property differences between IFs and matrices provide additional toughness compared with pure biopolymer fibrils. **Figure 8a** shows a schematic of the tubular structure of a horse hoof, which is a tough energy-absorbing material made of keratin.<sup>[64]</sup> The IFs orient along the different directions of the different layers surrounding the tubules (as shown in **Figure 8a**). The tensile stress–strain curves of individual IFs and the matrix, as well as the fiber as a combination of IF and matrix are shown

in **Figure 8b**.<sup>[35a]</sup> The IFs show a higher elastic modulus and tensile strength than the amorphous matrix. Due to the stiffness mismatch, cracks could be redirected and propagate perpendicularly to the original direction, which has been summarized as a Cook–Gordan crack-stopping mechanism.<sup>[65]</sup> **Figure 8c** is a schematic illustrating the toughening mechanism: a crack initiates at the IF and propagates perpendicularly to the fibril direction; the stress ahead of the crack opens up the weak interfaces in the amorphous matrix; cracks then propagate along the IF direction. In addition, the different orientations of IFs in different layers surrounding the tubules could also act as crack deflectors, thus increasing the fracture toughness of the hoof structure.

### 3.1.3. Cellulosic and Chitin Fibril Rotation, Deformation, and Crack Deflection

Wood is considered to be one of the lightest but strongest and tough biological materials.<sup>[5b,44a]</sup> Cellulose fibrils within wood (and other plants) confer stiffness and strength. One of the toughening mechanisms contributed by the cellulose fibrils

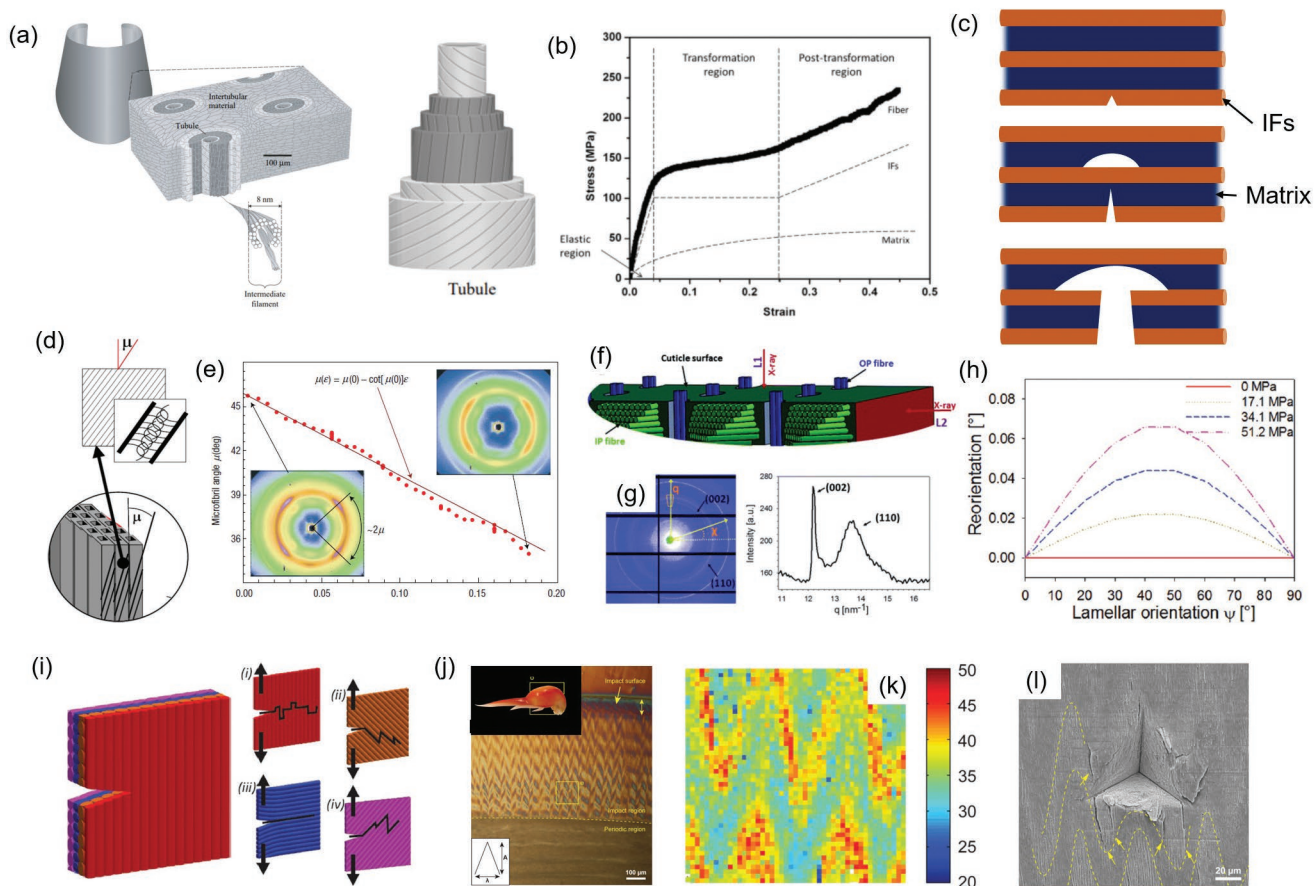


**Figure 8.** a) Tubular structure and intermediate filament arrangements in natural tubules. Adapted with permission.<sup>[64]</sup> Copyright 1999, Company of Biologists. b) Typical stress strain curves of intermediate filaments (IFs) and the amorphous matrix. Adapted with permission.<sup>[35a]</sup> Copyright 2017, Elsevier. c) Schematic of the Cook–Gordan crack-stopping mechanism due to the stiffness difference between IFs and matrix. d) Cellulose microfibril arrangement in the wood cell wall. e) Microfibril angle as a function of tensile strain. d) Adapted with permission.<sup>[66a]</sup> Copyright 2005, Springer. e) Adapted with permission.<sup>[66b]</sup> Copyright 2003, Springer Nature. f) Bouligand structure of in-plane chitin fibrils in the stomatopod cuticle. g) The WAXD pattern shows (002) and (110) crystal planes. h) Fibril rotation angle as a function of lamellar orientation. f–h) Adapted with permission.<sup>[68]</sup> Copyright 2017, Royal Society of Chemistry. i) Schematic of crack propagation in the Bouligand structure. Reproduced with permission.<sup>[69]</sup> Copyright 2015, Wiley-VCH. j) Optical micrograph of the herringbone structure highlighting sinusoidal orientation of chitin fibrils in the outer region of the stomatopod dactyl club. k) Modulus mapping of the herringbone structure, confirming regional out-of-plane stiffness. l) SEM micrograph of the crack profile on the herringbone structure initiated by nanoindentation. j–l) Adapted with permission.<sup>[70]</sup> Copyright 2016, Wiley-VCH.

is the rotation and reorientation of these fibrils.<sup>[66b]</sup> Cellulose microfibrils are usually oriented with a specific angle as a spiral around the wood cell wall, which is known as cellulose microfibril angle (MFA,  $\mu$ ) (Figure 8d).<sup>[67]</sup> The stiffness is correlated to the angle of the fibril, with the highest stiffness when  $\mu = 0$ . In situ synchrotron X-ray diffraction reveals the microfibril angle (MFA) decreases as the tensile strain increases (Figure 8e), indicating the cellulosic microfibrils are rotating into the direction of the tensile force. In addition, the shear stresses caused during the rotation and sliding of cellulose fibrils induces plastic deformation and viscous flow of the lignin-rich matrix between the fibrils,<sup>[66b]</sup> and thus provide toughening to woods.

Similar toughening mechanisms related to fiber rotation was also found in arthropod cuticles consisting of chitin fibers.<sup>[68]</sup> Figure 8f shows the Bouligand or helicoidal architecture (in-plane) of chitin fibrils in the stomatopod cuticle surface. The diffraction pattern of the chitin fibrils highlights the orientations of (002) and (110) planes within the crystalline fibrils

(Figure 8g). Rotation of the chitin fibrils can thus be detected via in situ X-ray diffraction by monitoring the orientational change of these planes. The rotation angles of the fibrils in different orientations are summarized in Figure 8h. Compared to the significant rotation of collagen and cellulose fibrils in previous sections, the rotation angle of the in-plane chitin fibrils under tension are much smaller (less than  $1^\circ$ ), which could be the result of the constraint of assembly or from the out of plane pore canal chitinous fibrils. It was verified that as a tensile stress was applied to the cuticle samples, the out-of-plane fibrils underwent compressive strains, which could explain the resistance to rotation of in-plane fibrils. As a result, the toughness in chitin microfibrils is contributed by the deformation of both the in-plane and the out-of-plane fibrils.<sup>[68]</sup>

In addition to the rotation and deformation of fibrils, crack deflection by chitin fibrils is also an important toughening mechanism found in various fibril-based structures with helicoidal arrangements. The toughening mechanism is summarized by the previous study shown in Figure 8i.<sup>[69]</sup> Cracks tend to

propagate along these fibrils, guided by the helicoidal orientation of nanofibrils. The complicated route of crack propagation, with both crack deflection and crack twisting, results in a significant increase in fracture toughness. In addition to this Bouligand structure, researchers identified a sinusoidal-like herringbone structure consisting of chitin nanofibrils in mantis shrimp dactyl clubs (Figure 8j). The stiffness map indicates that the reorientation of these fibers, which are directed in an out of plane orientation, provide significant stiffening leading to an enhanced ability to transfer momentum in the mantis' offensive strikes (Figure 8k).<sup>[70]</sup> Indeed, by using nanoindentation to initiate cracks, it was found that the cracks were deflected by out-of-plane fibrils (Figure 8l).<sup>[70]</sup>

In summary, toughening mechanisms for materials composed of biopolymers at the nanoscale are straightening, rotation, and deformation of nanofibrils; delamination and crack deflection by fibrils arranged with Bouligand or herringbone structures; crack deflection and reorientation due to the weak interfaces between fibrils and matrix; fibril bridging.

### 3.2. Biomineral Nanoparticles, Nanoplatelets, and Nanorods

#### 3.2.1. Nanoparticle Rotation, Translation, and Deformation

The toughening mechanisms in nacre have been investigated in numerous studies.<sup>[5a,10a,48]</sup> One nanoscale toughening mechanism is attributed to the aragonite nanoparticles and the surrounding organic interfaces, which are the building blocks of the platelets (tablets) in nacre.<sup>[71]</sup> Figure 9a shows

the lamellar structure of these platelets as well as their constituent nanograins ( $\approx 10\text{--}50$  nm in diameter). The fracture of the lamellae after microindentation is indicated in Figure 9b. Cracks marked with dashed lines initiate at the indentation tip and propagate through the lamellae. TEM micrographs of the cracks in the platelets are shown in Figure 9c,d. Cracks propagate through platelets 1–3, occurring at the weak interfaces between the  $\approx 50$  nm nanograins. Separation of adjacent lamellae is also found. An organic fibril bridge is indicated with a white arrow in Figure 9d, which offers another toughening mechanism at the nanoscale.<sup>[71a]</sup> Similar nanograin separation under tensile forces is reported by researchers using in situ atomic force microscopy.<sup>[71b]</sup> The biopolymers between the irregular nanograins are stretched under tension, leaving enough space for the rotation of the nanograins (Figure 9e). The shear stress induced by the rotation of irregular grains leads to further deformation of the individual grains.<sup>[71b]</sup> Thus, the plastic deformation of biopolymer interface, rotation and deformation of nanograins are the main energy dissipation mechanisms of nacre at the nanoscale.

Interestingly,  $\approx 60$  nm size hydroxyapatite nanoparticles glued by organic biopolymer matrix are also found in the outermost surface of mantis shrimp dactyl club, similar to the aforementioned nanograins in nacre platelets (Figure 9f).<sup>[14a,70]</sup> Unlike nacre, the mantis shrimp dactyl clubs are undergo  $\approx 20$  m s<sup>-1</sup> high-speed impacts, in which the strain rate can reach  $\approx 10^4$  s<sup>-1</sup>. It has been found that the nanoparticle pile-up is one of the energy dissipation mechanisms attributed to the nanoparticles and biopolymer matrix (Figure 9g).<sup>[70]</sup> Interfacial sliding, rotation and rearrangement of mineral crystals on the dactyl club surface

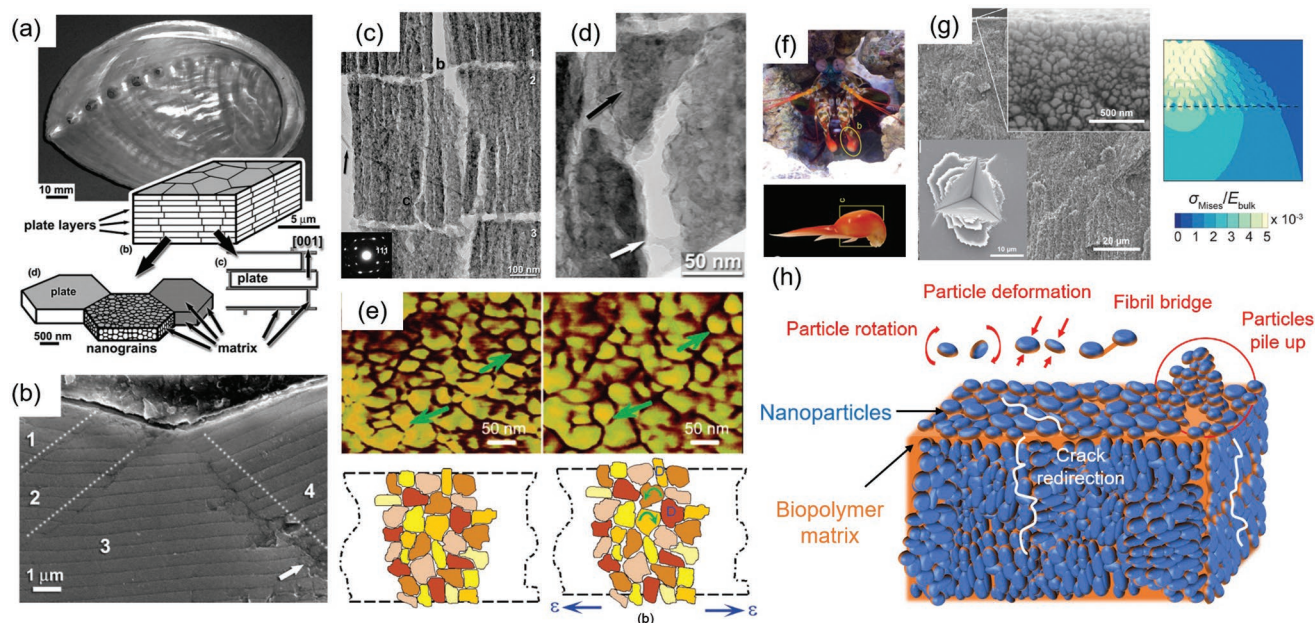


**Figure 9.** Toughening mechanisms of nanoparticles. a) Nanograins within the platelet of nacre. b) Cracks in the nacre lamellae initiated by indentation. c) TEM micrograph of cracks in the areas indicated with white arrows in (b). d) Cracks between nanograins and biopolymer fibrils bridge connections with adjacent grains. e) Rotation and deformation of nanograins under uniaxial tension. f) Photo of a mantis shrimp and its dactyl club. g) Nanoparticles within the outermost region of the dactyl club; particle pile up and stress localization in the particle layer. h) Schematic of toughening mechanisms of nanoparticles: particle rotation, deformation, pile up and fibril bridging, crack redirection. a–d) Adapted with permission.<sup>[71a]</sup> Copyright 2008, Materials Research Society. e) Adapted with permission.<sup>[71b]</sup> Copyright 2006, American Chemical Society. f,g) Adapted with permission.<sup>[70]</sup> Copyright 2016, Wiley-VCH.

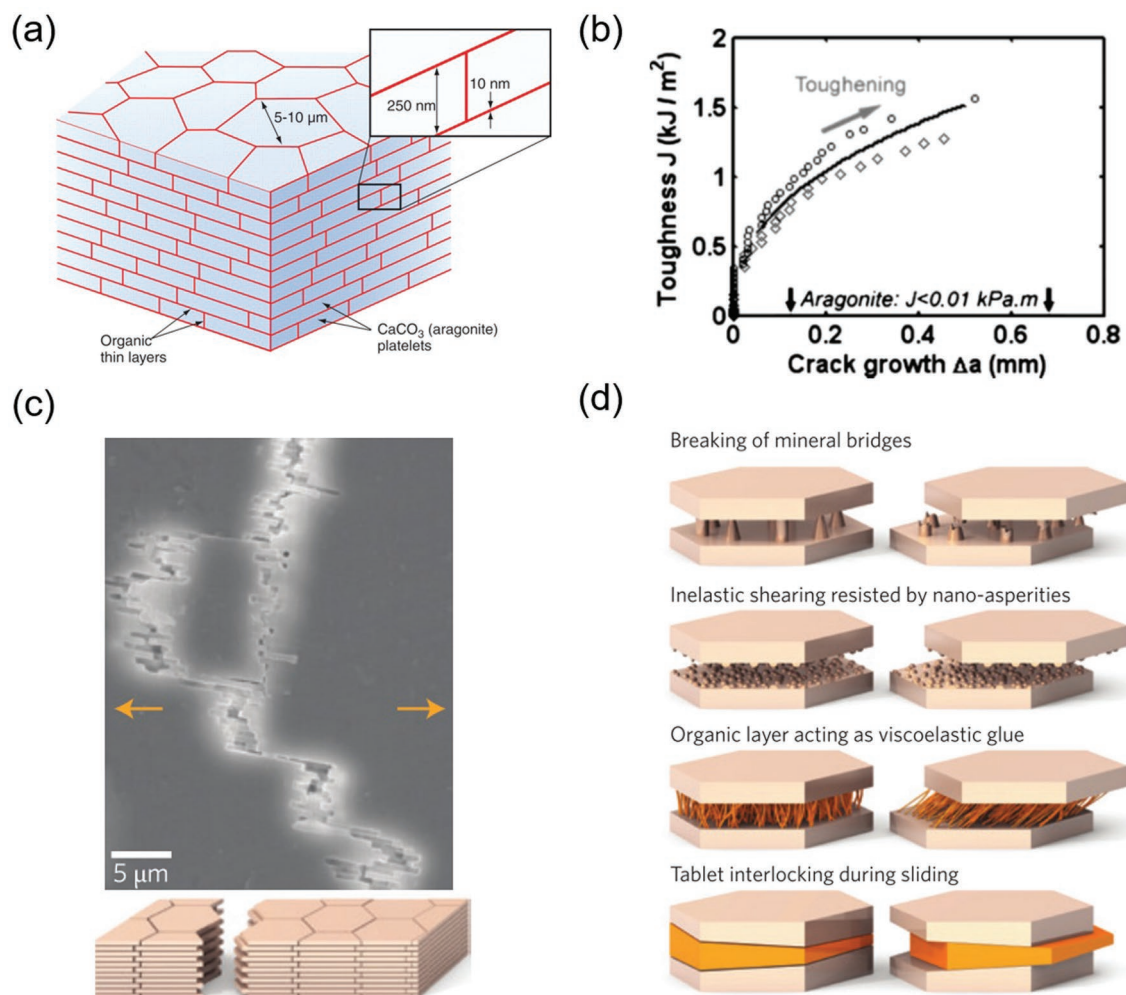


**Figure 10.** a) Aragonite platelets in nacre. b) Toughness as a function of crack growth acquired from a three-point bending test. c) Platelets sliding under tension. d) Schematic of different energy dissipation mechanisms in the platelet sliding process. a) Adapted with permission.<sup>[73]</sup> Copyright 2005, American Association for the Advancement of Science. b) Adapted with permission.<sup>[10a]</sup> Copyright 2007, Elsevier. c,d) Adapted with permission.<sup>[5a]</sup> Copyright 2015, Springer Nature.

were also found in the plastic regime.<sup>[14b]</sup> The stiffness of the nanoparticles is  $\approx 2\text{--}3$  times higher than the structure beneath it, leading to the stress localization on the surface nanoparticle layer, thus protecting the structure from catastrophic failure under high-speed impacts. Figure 9g shows the simulation results of the stress localization in the nanoparticle layer, which corroborates nanoindentation observations. As a summary, the toughening mechanisms afforded by the nanoparticle-based biominerals are illustrated in Figure 9h. Nanoparticles rotate, deform, and pile-up, while biopolymer fibrils bridge cracks as well as provide crack reorientation caused by the modulus mismatch between the mineral particles and polymer matrix.

### 3.2.2. Nanoplatelets Sliding and Energy Dissipation

Apart from the toughening mechanism introduced by the aragonitic nanograins in the tablets of nacre, sliding of the platelets can also dissipate energy in various ways.<sup>[10a,72]</sup> Figure 10a shows a schematic of a tablet arrangement in nacre.<sup>[73]</sup> The dimensions

of the tablets are around  $5\text{--}10\ \mu\text{m}$  wide and  $\approx 500\ \text{nm}$  thick, while the organic interfaces between adjacent tablets are  $\approx 10\ \text{nm}$ . The fracture toughness plotted as a function of crack length is shown in Figure 10b, indicating a growing toughness as the crack propagates (*R*-curve behavior). The fracture toughness of nacre is orders of magnitude higher than that of aragonite mineral.<sup>[10a]</sup> This toughness increase during crack propagation is proposed to be contributed by the sliding of tablets (Figure 10c).<sup>[5a]</sup> The various toughening mechanisms caused by the sliding of tablets has been addressed in previous studies and were summarized by Wegst et al. as shown in Figure 10d: breakage of mineral bridges; the inelastic resistance of the nanoasperities on the surface of tablets; the viscoelastic behavior of the organic layer between adjacent tablets; tablet interlocking during the sliding.<sup>[5a]</sup>

### 3.2.3. Crack Deflection by Nanorods

Besides nanoparticles and nanoplatelets, nanorods are another example of a geometric form of natural biomineral existing in

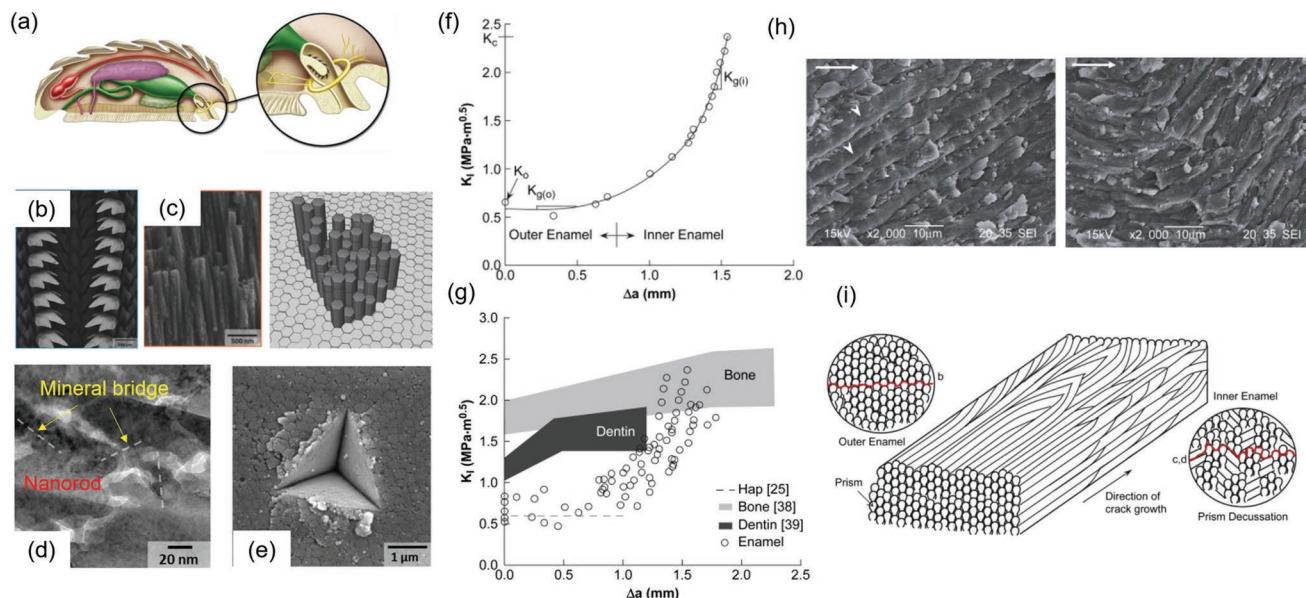


**Figure 11.** Toughening mechanisms in biomineral nanorods. a) Schematic of chitin and chitin teeth. b) Back scattered SEM micrograph of highly mineralized chitin teeth forming two rows. c) SEM image and schematic of nanorods in the mineralized teeth. d) TEM micrograph shows the nanorods and mineral bridges between the rods. e) Crack propagation induced by nanoindentation on the chitin tooth surface. f)  $R$ -curve of human tooth enamel measured by compact tension. g) Comparison of fracture toughness between bone, dentin, and enamel, highlighting the fracture toughness of tooth enamel is comparable with bone. h) Crack profile in outer and inner enamel, showing crack bifurcation and deflection in the inner enamel. i) Schematic showing orientations of prisms within the outer and inner enamel. a) Adapted with permission.<sup>[10b]</sup> Copyright 2010, Elsevier; b–e) Adapted with permission.<sup>[74]</sup> Copyright 2014, Wiley-VCH. f–i) Adapted with permission.<sup>[75a]</sup> Copyright 2009, Elsevier.

various organisms. For example, the ultrahard radular teeth from the chiton (a mollusk, for example, *Cryptochiton stelleri*), consist of tough and wear resistant magnetite, and are used to abrade intertidal rocks to get to epi- and endolithic algae (Figure 11a,b).<sup>[10b,53a]</sup> The cusps of these teeth are architected with magnetite-based nanorods (average diameter  $\approx 200$  nm) that are oriented along the long axis of the teeth. Nanomechanical measurements of the chiton teeth revealed a stiffness  $\approx 130$  GPa and hardness  $\approx 12$  GPa, providing a significant abrasion resistant structure (Figure 11c).<sup>[10b]</sup> The nanorods are surrounded by a veneer of organic fibers which at early growth stages, act as templates for the biomineralization. Mineral growing beyond the organic fibers that dictate the rod diameter yielded additional nanoscale features (i.e., surface asperities and mineral bridges) similar to those observed in nacre (Figure 11d).<sup>[74]</sup> Cracks initiated by nanoindentation with a sharp cube corner tip are found propagating radially and in a tortuous way, around each nanorod (Figure 11e). Thus, the hard and stiff nanorods deflect cracks at the organic interfaces. The asperities on the nanorods provide significant surface roughness, inhibiting the nanorods from sliding, which is a toughening mechanism also found in nacre. In addition, the nanobridges connecting adjacent nanorods interlocking the structure and provide strength to the weak organic interfaces, thus hindering crack propagation and increasing energy dissipation.<sup>[74]</sup>

Another example of a strong and tough nanorod structure is human tooth enamel.<sup>[75]</sup> As the most highly mineralized tissue in the human body, tooth enamel consists of  $\approx 96\%$  hydroxyapatite and  $\approx 4\%$  organic material. The hydroxyapatite is

in the form of nanorods that are  $\approx 25$  nm in diameter and  $\approx 100$  nm in length. These nanorods are hierarchically assembled, forming prisms with a diameter  $\approx 5$   $\mu\text{m}$ . The fracture toughness of tooth enamel was measured and is illustrated having  $R$ -curve behavior (Figure 11f).<sup>[75a]</sup> It is found that as the crack propagates from the outer to the inner region of enamel, the fracture toughness increases dramatically. The fracture toughness of the inner enamel is comparable with bone (Figure 11g). Figure 11h highlights crack deflection and bifurcation in the inner enamel, which are the main toughening mechanisms in the inner enamel. The nanorods in the outer enamel are arranged in a parallel fashion and cracks propagate straight through the weak interfaces, while in the inner enamel, the nanorods are no longer straight and parallel, which forces cracks to deflect and twist (Figure 11i).<sup>[75a]</sup>

#### 4. Microscale

Multiple microscale design elements have been identified in biological structures and reviewed.<sup>[69]</sup> Some of these elements include: fibrous, helical, gradient, lamellar, tubular, cellular, suture, overlapping structures, and materials junctions/interfaces. These elements have been revealed to serve as toughening and energy dissipation roles by redirecting crack propagation or undergoing plastic deformation. Here, crack deflection and energy dissipation by tubular and lamellar structures as well as junctions between materials at the microscale level are discussed.

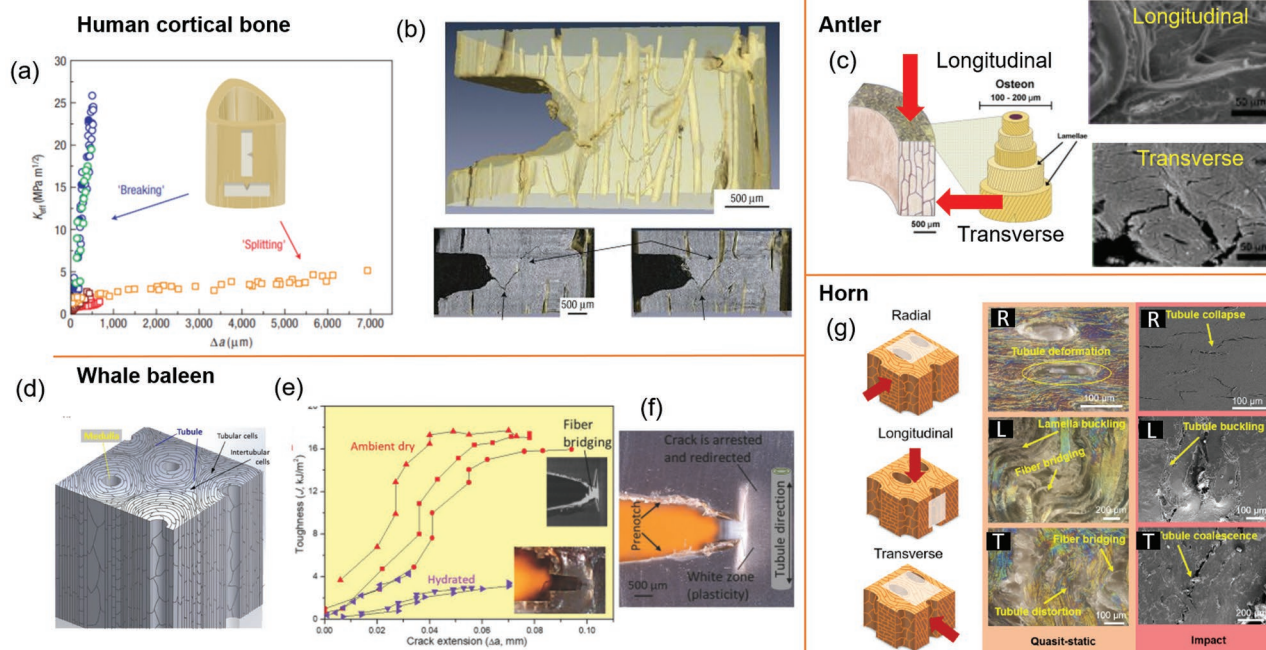


**Figure 12.** Toughening mechanisms in a natural tubular structure. a) *R*-curve of human cortical bone in the direction parallel with and perpendicular to the tubules (osteons). b) Microcomputed tomography showing crack propagation profiles indicating crack deflection by osteons. c) Impact damage of the tubular structures in antler in both longitudinal and transverse directions. d) Tubular structure within whale baleen. e) *R*-curve of whale baleen in the longitudinal and transverse directions. f) Crack arresting and deflection during the propagation through tubules. g) Deformation mechanisms of tubules in bighorn sheep horn under both quasi-static compression and high strain rate impacts along different directions. a,b) Adapted with permission.<sup>[76]</sup> Copyright 2008, Springer Nature. c) Adapted with permission.<sup>[79]</sup> Copyright 2011, Elsevier. d–f) Adapted with permission.<sup>[81]</sup> Copyright 2018, Wiley-VCH. g) Adapted with permission.<sup>[15]</sup> Copyright 2017, Elsevier.

#### 4.1. Crack Deflection/Twist and Plastic Deformation of Tubular Structure

##### 4.1.1. Osteons in Human Bone and Antler

The fracture toughness and toughening mechanisms of bone has been studied intensively. One of the main extrinsic toughening mechanisms is the crack deflection/twisting by osteons.<sup>[2,8,9,76]</sup> The osteons are tubular structures  $\approx 100 \mu\text{m}$  in diameter formed by mineralized collagen lamellae. *R*-curves evaluating the crack growth properties in the directions parallel and perpendicular to the osteons have been acquired (Figure 12a).<sup>[76]</sup> The results show that the toughness perpendicular to the osteons can be 5 times higher than that in the direction parallel with the osteons. The most significant difference in fracture toughness is caused by the crack deflection/twisting by the osteons. Figure 12b shows synchrotron X-ray computed tomography images indicating cracks deflected by  $90^\circ$  when reaching the osteons.<sup>[76]</sup> Similar toughening mechanisms were also found in antlers, which is a bone-like structure that serves as a fighting weapon in animals. The fracture toughness of antler at the direction perpendicular to the osteons is comparable with human cortical bone, and crack deflection by osteons as a toughening mechanism at quasi-static loading rates was identified.<sup>[77]</sup> However, the natural loading rate of antler is in the range of  $10^2\text{--}10^3 \text{ s}^{-1}$ , presenting a more severe stress condition versus those of human bones.<sup>[78]</sup> Thus, in order to determine energy dissipation mechanisms of antlers at

high strain rates, they were investigated using split-Hopkinson pressure bar (SHPB) tests.<sup>[79]</sup> Antler samples were found to withstand  $\approx 300 \text{ MPa}$  compressive stress and  $\approx 20\%$  compressive strain before failure, indicating an impressive amount of energy absorption. Shear band formation around the osteons and microcracking of individual osteons were determined to be the primary energy dissipation mechanisms in the direction perpendicular to the osteons (Figure 12c). Similar to the quasi-static loading condition, crack deflection by osteons was also observed at high strain rate impacts in this direction,<sup>[79b]</sup> while buckling and separation of lamellae in osteons occurred in the longitudinal direction.<sup>[79a]</sup>

##### 4.1.2. Tubules in Whale Baleen and Bighorn Sheep Horn

Tubular structures are also found in biological materials with little or no mineral. It was determined that these structures also act to provide toughening and energy dissipation under quasi-static compression and high strain rate impacts.<sup>[15,64a,80]</sup> One example is found in whale baleen, a filter system in the baleen whale mouth that works by pushing water out while retaining food inside the mouth.<sup>[80]</sup> Baleen is a keratinized tissue with a relative low degree of mineralization (around  $\approx 1\text{--}4 \text{ wt}\%$ ). It was found that these microstructured tubules inside the baleen contributed to the fracture toughness of the whole structure in the direction perpendicular to the tubules.<sup>[81]</sup> Figure 12d shows a schematic of the tubular structure, in which keratinized cells

are indicated in both tubule and intertubular areas. The characteristic diameters of the tubules range from 60 to 900  $\mu\text{m}$ . The fracture toughness of the baleen samples as a function of crack extension ( $R$ -curve) was acquired via three-point bending with single-edge notched samples. It was concluded that in both ambient dry and hydrated conditions, the fracture toughness increases significantly as the crack propagates (Figure 12e). This can be explained by the extrinsic toughening mechanism shown in Figure 12f, where the initial cracks which are perpendicular to the tubules are deflected by  $90^\circ$ , and start propagating along the tubules.<sup>[81]</sup> Crack deflection by the tubular structures is caused by the weak interfaces between the cell lamellae, which is similar to that observed in bone osteons.

Bighorn sheep horn is another keratinized tissue with a tubular structure that shows high energy dissipation properties. However, the loading conditions are at higher strain rates than the whale baleen.<sup>[32,33]</sup> The intraspecific fighting speed between bighorn sheep can reach  $9 \text{ m s}^{-1}$ , which necessitates high impact resistance and energy absorption in the horns. The energy dissipation/toughening mechanisms of the bighorn sheep horn were investigated at different strain rates and loading orientations.<sup>[15]</sup> Figure 12g shows how the tubular structure absorbs energy under both quasi-static compression and high strain rate ( $\approx 10^3 \text{ s}^{-1}$ ) impact. Cross-section analysis of the tubules reveal an elliptical shape, leading to the anisotropic

compressive properties and deformation mechanisms. Compression and impact in the radial direction, which is along the minor axis, could deform and close the tubules. However, when the loading is along the major axis of the tubules, the tubules become distorted. Tubule coalescence and fiber bridges are also found during the shear deformation of the structure. Tubules and lamellae buckle and crack under the loading in the direction parallel with the tubules in both quasi-static compression and high strain rate impact. It was found that the plastic deformation of tubules (closing, coalescing, buckling, and cracking) could dissipate a large amount of energy, which is sufficient for the high strain rate impact caused by the fighting between bighorn sheep.<sup>[15]</sup>

## 4.2. Crack Redirection and Twist in Lamellar Structure

### 4.2.1. Silica Lamellae in Marine Glass Sponge

The extrinsic toughening mechanisms such as crack redirection and twisting are also found in lamellar structures at the microscale level.<sup>[59,82]</sup> One example of the laminated structural design is in the spicules of a sea sponge, *Euplectella aspergillum* (Figure 13a).<sup>[53c]</sup> Microscopic biosilica concentric rings form lamellae in the spicule with organic materials at the interfaces

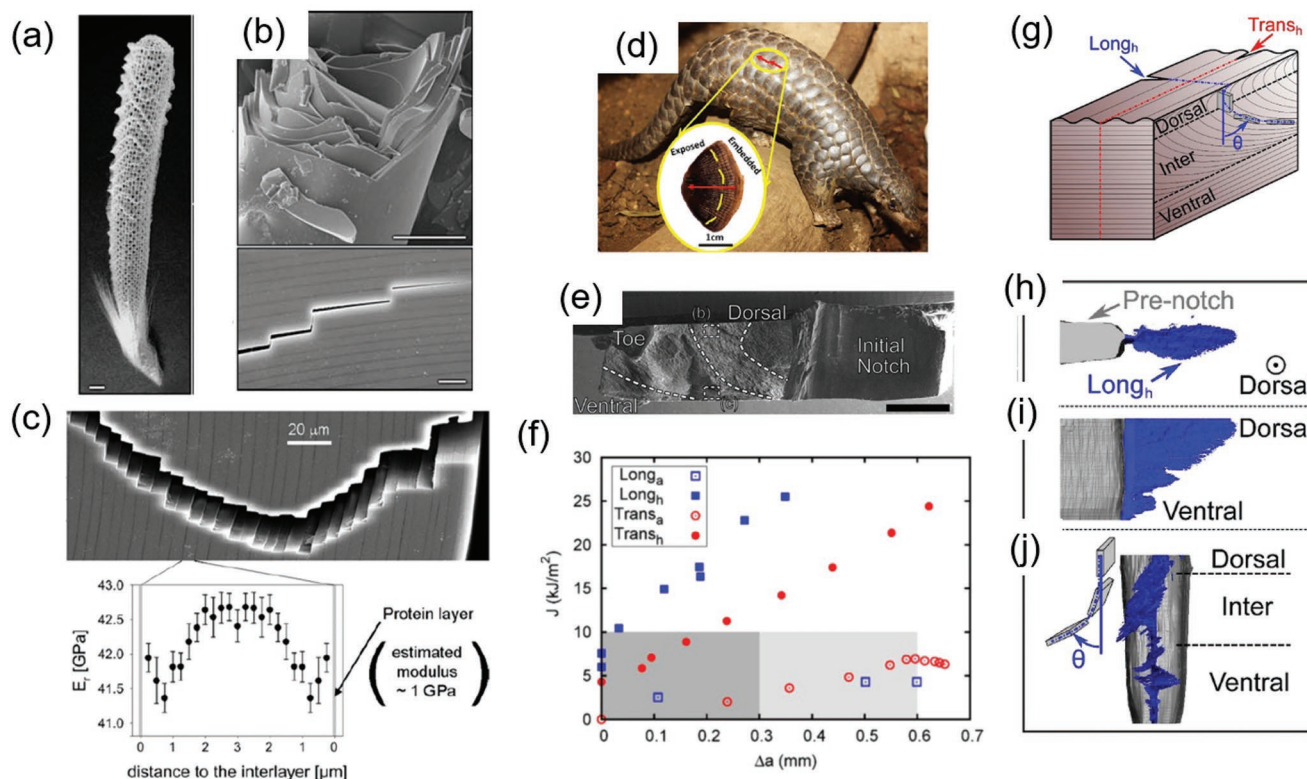


**Figure 13.** Crack deflection and twisting in lamellar structures. a) Photograph of sea sponge *Euplectella aspergillum*. b) Crack surfaces and pathways in a silica spicule. c) SEM micrograph showing crack deflection and the periodic elastic modulus of silica lamellae. d) Photograph of a pangolin and its keratin scales. e) Arrangement and orientation of keratin cells in the scales. f)  $R$ -curve of a pangolin scale in different orientations through three-point bending tests. g) Schematic of a three-point bending test sample and orientation of keratin cell lamellae. h–j) Microcomputed tomography images showing the crack profile in different positions. a,b) Adapted with permission.<sup>[53c]</sup> Copyright 2005, American Association for the Advancement of Science. c) Adapted with permission.<sup>[83]</sup> Copyright 2007, Wiley-VCH. d) Adapted with permission.<sup>[82]</sup> Copyright 2016, Elsevier. e–j) Adapted with permission.<sup>[86]</sup> Copyright 2017, Elsevier.

between the lamellae.<sup>[53c,57]</sup> The crack deviation by the organic layers between the lamellae are shown in the SEM micrograph of a fracture surface and the internal cracks existing in the spicule (Figure 13b).<sup>[53c,59]</sup> Analytical methods were applied<sup>[83]</sup> to verify crack stopping mechanics in lamellar structures with periodic elastic moduli. It was shown that regardless of thickness, crack stopping can occur at the weak interfaces when the ratio of elastic modulus between the stiff lamellae and the weak interface was larger than five. The ratio of the Young's modulus between the silica lamellae and organic interface can reach  $\approx 40$ . This could explain the ability for 5–10 nm thick organic layers between the concentric rings to deflect and deviate cracks, thus increasing the overall toughness of spicule (Figure 13c).<sup>[59,83]</sup> As a comparison, the energy absorption of spicule under three-point bending is an order of magnitude higher than that of silicate glass fibers (EMGO 360). The higher the strain rates, the more energy dissipation is produced in spicules, likely due to an increasing crack deviation and deflection at high strain rates. While the amount of energy dissipation in the glass fiber (EMGO 360) is not affected by strain rates as expected, since there is no such toughening mechanism in the glass fibers.<sup>[84]</sup> Similarly, the crack deflection mechanisms caused by the stiffness differences between organic growth bands and mineral platelets were also reported in the nacre.<sup>[85]</sup>

#### 4.2.2. Keratin Cell Lamellae in Pangolin Scales

Keratinized scales are efficient natural dermal armor found in pangolin that can prevent penetration damage from predators (Figure 13d).<sup>[82]</sup> The basic component of pangolin scales are laminated keratinized cells, with dimension  $\approx 1\text{--}3\ \mu\text{m}$  in thickness and  $\approx 20\text{--}30\ \mu\text{m}$  in diameter.<sup>[82]</sup> The overall fracture toughness is improved through the inherent high fracture toughness of the keratin material itself as well as the microstructured lamellae architecture. The keratin cell lamellae change orientations from the dorsal to the ventral surface (Figure 13e).<sup>[86]</sup> The fracture toughness of the scales was evaluated by single-edge notch three-point bending. Figure 13f shows the *R*-curve of the pangolin scale samples in both longitudinal and transverse directions. A schematic of notch directions relative to the lamellae structure is shown in Figure 13g. It can be concluded from the plots of the *R*-curve that the fracture toughness in the longitudinal direction is five times higher than that in the transverse direction. The high toughness in the longitudinal direction was found to be contributed by the nonuniform crack profiles from dorsal to ventral surface and crack twisting by the keratin cell lamellae. The crack profile is revealed by microcomputed tomography, showing the crack twisting in the longitudinal direction (Figure 13h–j).<sup>[86]</sup>

### 4.3. Crack Arrest and Energy Dissipation at Materials Junction

#### 4.3.1. Tooth Dentin–Enamel Junction

Biological organisms consist of “building blocks” of materials with different mechanical properties that when assembled in a hierarchical manner, can accommodate the different loading

conditions. There are a number of cases where this is exemplified. For example, woodpecker beaks and sheep horns are composed of an outer sheath of soft keratinous material and an inner core of hard cancellous bone to resist multiple impacts; the high toughness and strength of teeth under fatigue are provided by the combination of an outer brittle enamel and an inner tough dentin having a tubular architecture; penetration resistant fish scales consist of rigid mineral layers on their surface together with an underlying region of collagen-based fibers.<sup>[32,61b,75a,87]</sup> It has been shown a junction/interface between the different regions of biological structures could provide fracture toughness to the whole structure. As a representative example, the toughening mechanisms in the tooth dentin–enamel junction (DEJ) will be discussed in the following section.

Figure 14a shows a schematic of the enamel and dentin regions in a human tooth.<sup>[75a]</sup> The width of the junction region between enamel and dentin is  $\approx 100\text{--}150\ \mu\text{m}$ .<sup>[88]</sup> The differences in mechanical properties (including toughness and hardness) between enamel and dentin are illustrated in the plot as shown in Figure 14b. The fracture toughness of dentin is  $\approx 5$  times higher than that of enamel, but is 10 times less hard.<sup>[89b]</sup> Indentation experiments revealed that the cracks initiated at the enamel region, but were arrested at the DEJ. SEM micrographs of the crack profile indicates the cracks can only penetrate  $\approx 10\ \mu\text{m}$  across the junction. Uncracked ligament bridging behind the crack tip was considered as the main reason contributing to the crack arrest and fracture toughness of the DEJ (Figure 14c).<sup>[89b]</sup> In addition, the crack arresting mechanism was further observed and confirmed by researchers in the fatigue tests after  $10^6$  cycles of loading and unloading.<sup>[88]</sup> It was reported that the junction region would decrease the stress concentration and improve load transfer between the enamel and dentin. Due to the significant differences of stiffness between enamel and dentin, crack deflection was considered to be another toughening mechanism in the DEJ proposed in a previous study.<sup>[88]</sup>

#### 4.3.2. Junction and Interface of Boxfish Scutes

Besides junctions that consist of materials with different mechanical properties, the suture interface is a representative type of junction with the same materials or components, providing both flexibility and toughness to the biological structures.<sup>[90]</sup> One example is the junction of adjacent scutes in the boxfish dermal armor (Figure 14d). Figure 14e depicts the hexagonal scutes and suture interfaces between them. It was proposed that these suture mineralized “teeth” act to dissipate energy in various loading modes: penetration, tension, and shearing. Figure 14f illustrates the penetration test on the scutes, showing the shear deformation of collagen fibers and the punch out of the active scute without damage. The breakage of fibers under shear at the interface could absorb energy and thus protect the scute (Figure 14g). Under tension, fibers stretch and pull out at the interface are observed, which is similar as the damage modes in the penetration test: the deformations are limited to the collagen fibers in the suture interface (Figure 14h). The failure and fracture of the mineralized teeth

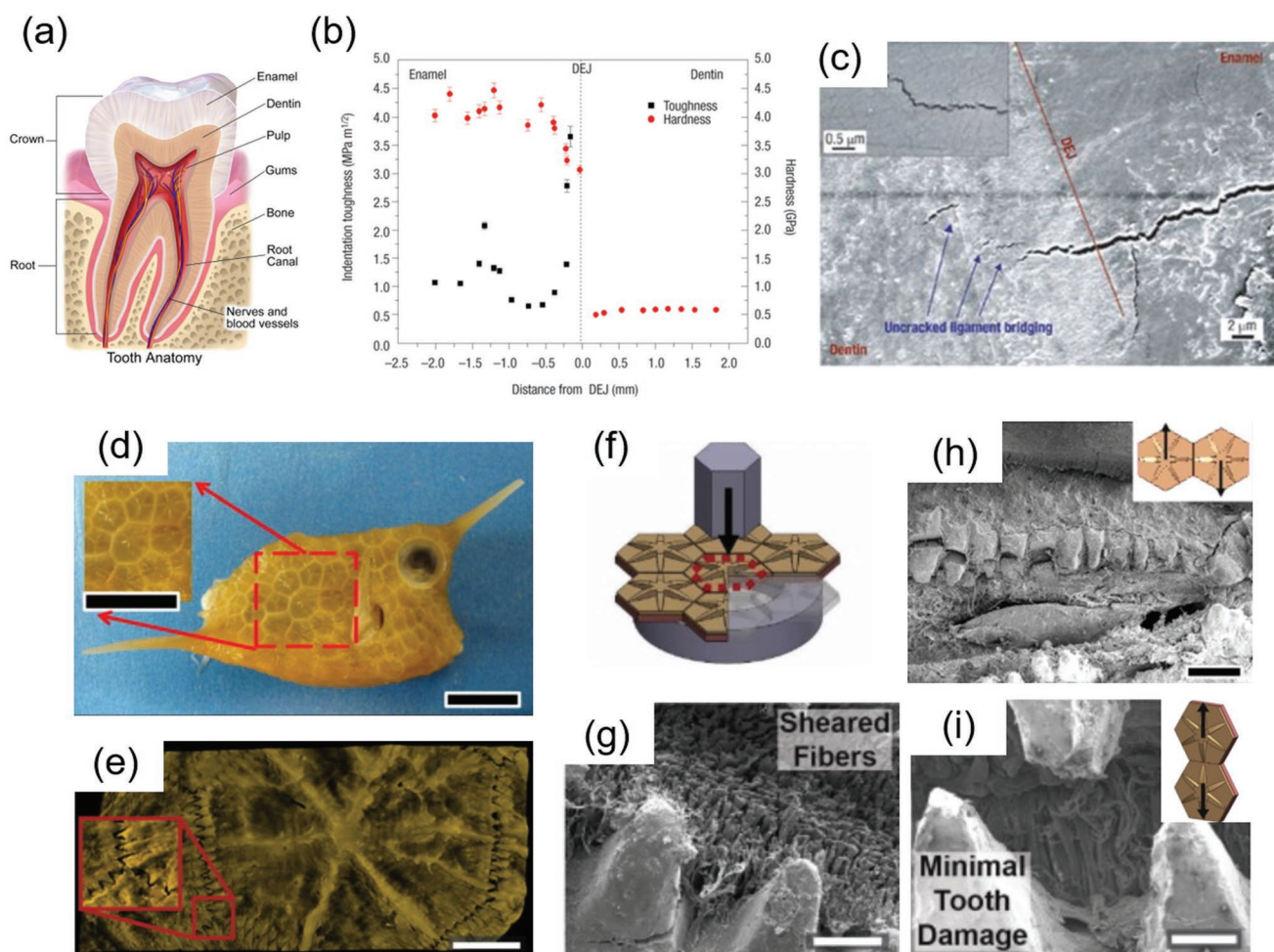


**Figure 14.** Energy dissipation at materials junctions/ interfaces. a) Schematic showing enamel and dentin in a human tooth. b) Fracture toughness and hardness as a function of the distance from the dentin–enamel junction (DEJ). c) Crack propagation profile in tooth enamel, dentin, and DEJ. d) Photograph of a box fish. e) Microcomputed tomography image of single scutes and the suture interface between adjacent scutes. f) Schematic of a penetration test on box fish scutes. g) SEM micrographs of fractured surfaces after penetration testing, showing fibril shearing. h) SEM micrograph of a fractured suture interface after uniaxial tension testing. i) Breakage of mineral teeth in the sutures after shear tests. a) Reproduced under the terms of the CC-BY Attribution 3.0 Unported license (<https://creativecommons.org/licenses/by/3.0/>).<sup>[89a]</sup> Copyright 2014, Blausen.com staff. b,c) Adapted with permission.<sup>[89b]</sup> Copyright 2005, Springer Nature. d–i) Adapted with permission.<sup>[90a]</sup> Copyright 2015, Elsevier.

at the interface is shown in the SEM micrograph of the sample under shear force (Figure 14i). The cracks initiate and propagate within the mineralized teeth and interface. Due to the connection of collagen fibers underneath, the whole structure is still intact after failure occurs in the teeth. In summary, different energy dissipation mechanisms are observed at the scute junctions under different loading modes. The suture interface between scutes could thus protect the overall structure from penetration, tension, and shearing. Interestingly, the suture structure has also been found in other natural armors such as keratin cells in pangolin scales and the turtle carapace.<sup>[91]</sup> It was concluded that the soft suture interface could localize the lateral cracks and thus terminate crack propagation.<sup>[90b]</sup>

## 5. Macroscale

At the macroscale level, the structure, morphology and arrangement of the architecture features could also affect the

mechanical behavior under different loading conditions. Examples include curvatures found in horns and turtle carapace,<sup>[90b,92]</sup> different shapes of cross-sectional designs for hydrodynamic and aerodynamic applications,<sup>[93]</sup> overlapping scales in fish, pangolin, and chiton,<sup>[61b,82,94]</sup> and the tessellated scale arrangements in boxfish armor and mineralized cartilage in the endoskeleton of Elasmobranchii.<sup>[90a,95]</sup> The characteristic morphology and element arrangement at the macroscale in these organisms can provide specific mechanical solutions to adapt to the loading conditions. Although the designs and features at the macroscale level are not directly involved in the improvement of fracture toughness of biological materials, the overall energy absorption can be affected by the macroscale characteristics such as shapes and arrangement.

One examples is found in the design of the seahorse tail.<sup>[96]</sup> The cross-section of the tail has a square shape, which is unlike most animal tails with round cross-sections. The seahorse applies its tail as a flexible grasping appendage, but also acts as bony armor to protect its body. From a mechanical

prospective, energy absorption should be an important requirement for the flexible bony armor of seahorse, which was realized by the design of the tail: four L-shaped platelets forming a flexible square shape. 3D printed models were applied to explain the mechanical optimization of the square tail.<sup>[96b]</sup> Both the strength and compressive displacement are higher in a square shape, indicating the square tails have larger energy absorption and better protection of internal organs. The sliding of the bony platelets in the square tail is the main energy dissipation mechanisms which enable nearly ≈50% compressive deformation on the tails before permanent failure of the vertebral column.<sup>[96b]</sup> Another example of design characteristic of natural organisms at the macroscale is the tapered spiral geometry of the bighorn sheep horns. It has been verified that the tapered spiral curved geometry decreases the translational acceleration in brain cavities under impacts by 49% compared to the geometry of just flat shape.<sup>[92]</sup>

Indeed, biological materials have hierarchical structures, meaning that the toughening mechanisms at different length scales are actually working together to contribute to the overall toughness of the organisms. The mechanical behavior of materials at the macroscale level, are actually a combination of properties from the atomic to the microscale level. Although the fracture toughness is a material property, which is not relevant to the architecture designs at the macroscale level, in terms of the amount of energy absorption and mechanical performance, the designs at the macroscale level do matter.

In terms of the relative importance of the toughening mechanisms at different length scales discussed in previous sections, although no direct quantitative comparisons have been made between different scales, implications can be made based on some of the work. Li and Ortiz showed an increase of energy dissipation by a factor of 10 by introducing atomic to nanoscale toughening mechanisms such as deformation twinning, amorphization, and grain rotation in the shell of bivalve compared to single crystal geological calcite.<sup>[47a]</sup> By introducing the nano- to microscale lamellar and interfaces in Al<sub>2</sub>O<sub>3</sub>/PMMA composites, the fracture toughness of the material increased from ≈2 MPa m<sup>1/2</sup> in a homogenous Al<sub>2</sub>O<sub>3</sub>/PMMA composite to 15–30 MPa m<sup>1/2</sup> in the structure with lamellae and interfaces.<sup>[12a]</sup> In another work, Wang et al. showed the toughness (*J* integral, kJ m<sup>-2</sup>) of whale baleen increased from ≈1.5 kJ m<sup>-2</sup> in longitudinal direction to ≈18 kJ m<sup>-2</sup> in transverse direction because of the crack deflection by tubules occurred in transverse direction at the microscale.<sup>[81]</sup> Although the quantification of contributions of different toughening mechanisms are in different biological systems, it is safe to conclude that the toughening mechanisms at different length scales all have the potential to increase the toughness by an order of magnitude.

## 6. Multiscale Modeling

### 6.1. Computational Modeling

The challenges related to the multiscale experimental characterization of biological materials have made computational modeling an essential tool to enable the understanding of the

underlying mechanisms that allow these materials to exhibit their remarkable properties by creating a link between theoretical descriptions and experimental observations. Typically, the modeling of biological structures are performed one scale at the time; then, the results for each single-scale analysis are used to provide a homogenized bulk behavior of the material. As shown in **Figure 15a**), the appropriate method of analysis for each scale depends on the relevant length and time resolutions. These methods are summarized in this review. A detailed explanation can be found in ref. [97].

**Quantum mechanics (QM):** At the atomic scale level, material properties are obtained by quantum mechanics calculations. The Schrodinger equation is utilized and solved to predict the excitation and reactive properties of molecules in biological materials. In these analyses, the molecules are discretized by wave functions describing the electron and atom positions in the system. To reduce the computational complexity, typically, these problems are solved by replacing electrons by an effective cluster of electrons with the same total density moving in the potential generated by the other electrons and ion cores. In a system of *N*-electrons, the total density is expressed as a sum of the orbitals,  $\phi_i$ ,

$$\rho(r) = \sum_{i=1}^N |\phi_i(r)|^2 \quad (1)$$

where  $\phi_i$  are the solutions of the Kohn–Sham equations

$$\left[ -\frac{\hbar^2}{2m} \nabla^2 + V_{\text{eff}} \right] \phi_i(r) = \epsilon_i \phi_i(r) \quad (2)$$

Here  $V_{\text{eff}}$  is the effective potential due to Coulomb and exchange-correlation contributions. This solution scheme is known as density functional theory (DFT) and is the most widely used method for the calculation of band structures, cohesive energies, chemisorption energies and activation barriers. Quantum mechanics simulations are limited to a size domain no larger than ≈1 nm and time spans no more than ≈1 ns.

**Molecular dynamics (MD):** Molecular dynamics are commonly used to study the mechanisms that control the deformation and rupture of chemical bonds at the nanoscale. The basic concept behind molecular dynamics simulations is to model the trajectory of each atom in the material by considering their atomic interaction potentials. The total energy is then calculated as a function of the nuclear positions of each atom and each atom is treated as a particle that behaves according to Newton's equation of classical mechanics

$$F_i = m_i a_i \quad (3)$$

where  $m_i$  is the mass of the *i*th atom and the force  $F_i$  acting on each atom is calculated from the inter-atomic potential energy

$$F_i = -\nabla_i U \quad (4)$$

Choosing appropriate models for the interatomic interactions is a crucial step, because once these interactions are defined, the complete behavior of the material is determined. Different interatomic potentials have been used at different scales and different types of protein structures in the modeling

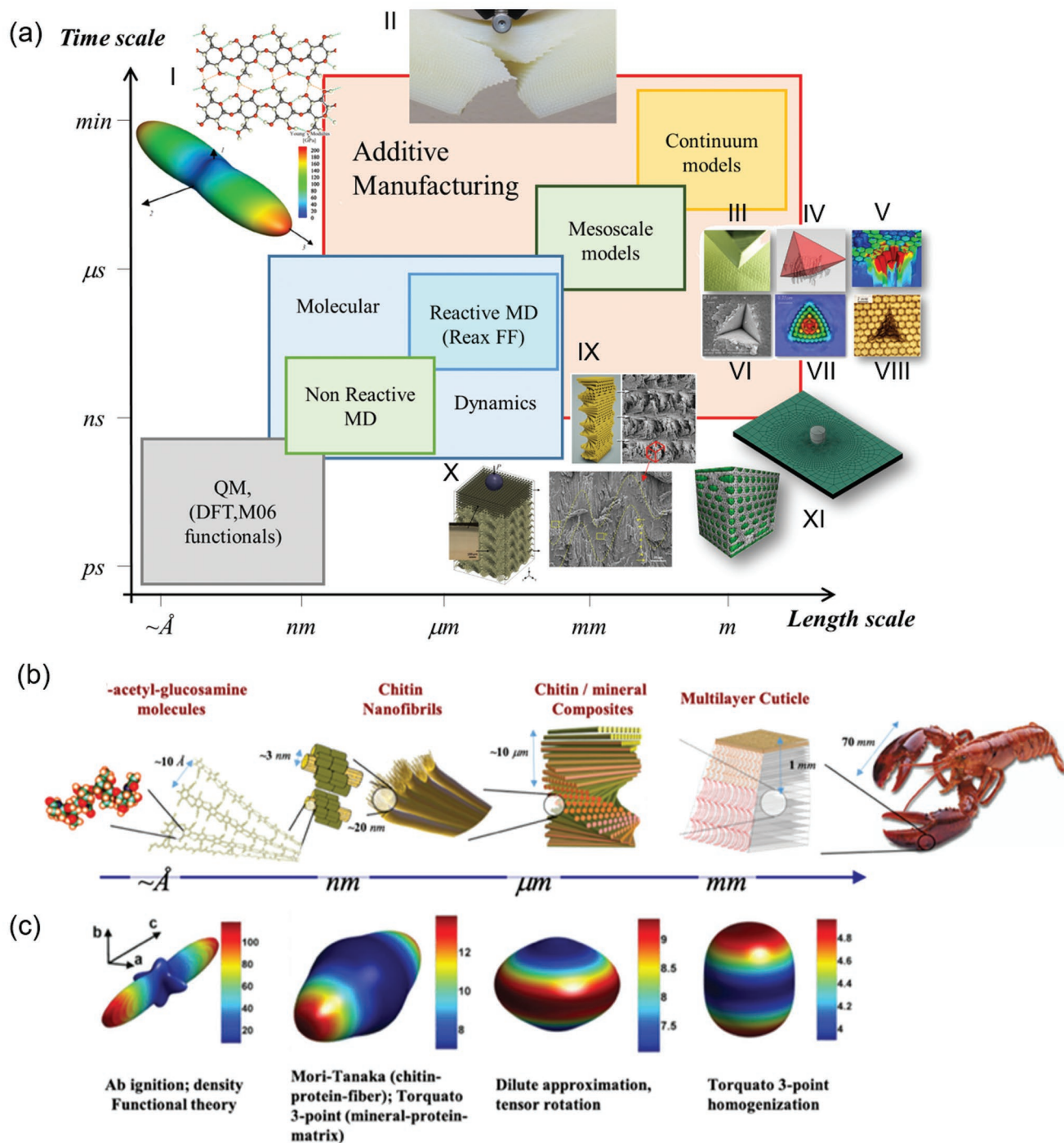


**Figure 15.** a) Time and length scale maps of modeling methods. b) Multiscale modeling of the exoskeleton of the American lobster. Overview of key microstructures found in the cuticle at different length scales. c) 3D maps for elastic behavior and homogenization methods for each relevant architecture. *a*, *b* axes: basal direction of the chitin unit cell. *c* axis: longitudinal (chain) axis of the chitin molecule. Results correspond to a typical mineral content of 70 wt%. a) I) Adapted with permission.<sup>[155]</sup> Copyright 2015, Elsevier. II) Adapted with permission.<sup>[109b]</sup> Copyright 2018, Elsevier. III) Adapted with permission.<sup>[106]</sup> Copyright 2015, Elsevier. IV–VIII) Adapted with permission.<sup>[10a]</sup> Copyright 2007, Springer. IX) Adapted with permission.<sup>[14a]</sup> Copyright 2012, The American Association for the Advancement of Science. X) Adapted with permission.<sup>[70]</sup> Copyright 2016, Wiley-VCH. XI) Adapted with permission.<sup>[152]</sup> Copyright 2014, Elsevier. b) Adapted with permission.<sup>[102]</sup> Copyright 2010, Wiley-VCH. c) Adapted with permission.<sup>[42]</sup> Copyright 2011, Elsevier.

of biological materials. These potentials typically include: CHARMM force field, DREIDING force field, UFF force field,

and reactive force fields like ReaxFF that allow the rupture and formation of covalent bonds.<sup>[98]</sup>

The main challenges in atomistic simulations are the difficulties for interpreting results (which consist of only positions and velocities of particles as a function of time), and the large computational resources necessary to perform such simulations. A proposed solution to reduce the computational cost is the modeling of coarse particles that replace clusters of atoms. In this case, interactions between particles are simulated by considering simple bonded and nonbonded interactions that can be easily calculated at each integration step. This method is known as coarse-grain modeling.<sup>[99]</sup>

**Mesoscale models:** Mesoscale models address the time limitation of MD. In these simulation schemes, the equations of MD are replaced by stochastic transitions for the slow processes in the system. The main use of mesoscale models is in the modeling of dislocation dynamics in metals. To the best of the authors' knowledge, these methods have not been applied for biological materials.

**Macroscopic methods:** Macroscopic methods are using for modeling of the continuum. The best known method is finite element analysis (FEA). In this scheme, the system of interest is discretized with a mesh formed by points called nodes that are connected by entities called elements. Then, a partial differential equation is then replaced by a set of coupled algebraic equations and solved numerically at the nodes.

It is important to note that the analysis of each scale provides fundamental information about the mechanical understanding of biological materials. For instance, in ref. [100] Buehler and co-workers use full atomistic simulations to describe the mechanics of collagen microfibrils, showing that the deformation of collagen microfibrils are mediated through mechanisms involving straightening of disordered and helically twisted molecules at small strains, followed by axial stretching of molecules, and eventual molecular uncoiling. These mechanisms explain the difference in the Young's modulus of collagen microfibril compared with that of single molecules, which is typically  $\approx 10$ – $20$  times greater than that of a collagen microfibril, and the high toughness present in these proteins. The authors used later a similar approach to characterize the mechanisms that provide high stiffness and high toughness to the spider silk.<sup>[101]</sup>

After a single scale of the material has been analyzed, bridging information obtained at different scales is required to understand the link between structure and properties at the different hierarchies observed in biological materials. However, the connection between scales is not trivial. Two main strategies are typically employed for scale bridging: i) matching of physical quantities such as energy and force between two scales, and (ii) volume averaging of the variables computed at the fine scale. For instance, in refs. [42,102] a new approach is presented that combine atomic scale simulations with hierarchical homogenization, allowing the study of structure–property relations including all length scales of the American lobster's exoskeleton. Schematic representations of this homogenization based technique are shown in Figures 15b,c. Similar techniques have also been applied for the study of collagen<sup>[103]</sup> and nanocellulose-based structures.<sup>[104]</sup>

Despite the limitations that exist to date in multiscale modeling of biological materials, the information found with single scale modeling techniques has been successfully integrated with different experimental and manufacturing techniques allowing to analyze the synergistic role between constituent materials, geometry, hierarchy, and size scales on the different

characteristics commonly found in mammals, marine creatures, and even plants.<sup>[1b,62]</sup>

## 6.2. Additive Manufacturing as a Modeling Tool

Despite the limitations in current additive manufacturing processing, 3D printing has emerged as a significant modeling tool that provides validation for both computational modeling and experimental results. This combination of methods accelerates discovery of the synergistic role between constituent materials, geometry, hierarchy, and length scales on the different architectural features commonly found in mammals, marine creatures and even plants.<sup>[1b,62]</sup> Under this approach, 3D printing has become an important tool to help understand and connect the different deformation and fracture mechanisms across length scales providing answers to questions like: i) “Can modest materials be used as building blocks for remarkably strong/tough materials?”. And ii) “Is it possible to obtain the same level of improvement in mechanical properties as Nature does?”. The combined experimental/computational/prototyping framework for the analysis and study of biological materials was first used by Zavattieri and co-workers to test some key morphological features of the microstructure of the nacre that enable its remarkable energy dissipation. For instance, in refs. [72b,105] the authors show that the geometrical parameters can be tuned in conjunction with the size of the building blocks to effectively toughen the composite, without sacrificing strength and stiffness through the transverse dilation effect previously shown in ref. [10a]. In fact, the highest fracture energy that was measured in artificial systems corresponded to the same geometrical characteristics and length scale found in the aragonite platelets in nacre.

Kisailus' and Zavattieri's research groups have used the combined experimental/computational/prototyping framework in the analysis of other biological materials. In refs. [74,106] the authors used this approach to study the rod-like microstructure found in the *Cryptochiton stelleri* radular teeth, elucidating the effect of geometrical features like orientation, volume fraction, and rod aspect ratio on the overall mechanical response (**Figure 16a–c**). In this work, experimental results demonstrated that alignment rod-like microstructures present a higher contact resistance and stiffness compared with randomly distributed fibrous materials. Additionally, it was possible to observe that energy gets dissipated by median cracks when the loading is parallel to the rods, and lateral cracks when the load is perpendicular to the rods in combination to deformation of the rods. The authors also have studied the dactyl club of the smasher stomatopod *Odontodactylus scyllarus* where a new ultrastructure with a herringbone pattern was experimentally determined (**Figure 16d–i**) and hypothesized to provide additional stiffness during club strikes.<sup>[70]</sup> Subsequent finite element simulations in combination with experiments on 3D printed samples were used to evaluate the mechanical response of the herringbone ultrastructure compared with the Bouligand structure typically found within most crustacean exoskeletons. Results from computational simulations revealed that the herringbone structure allows for a greater redistribution of damage over the Bouligand structure preventing catastrophic failure. Subsequent experiments using the 3D printed samples showed that the herringbone pattern allows to accommodate

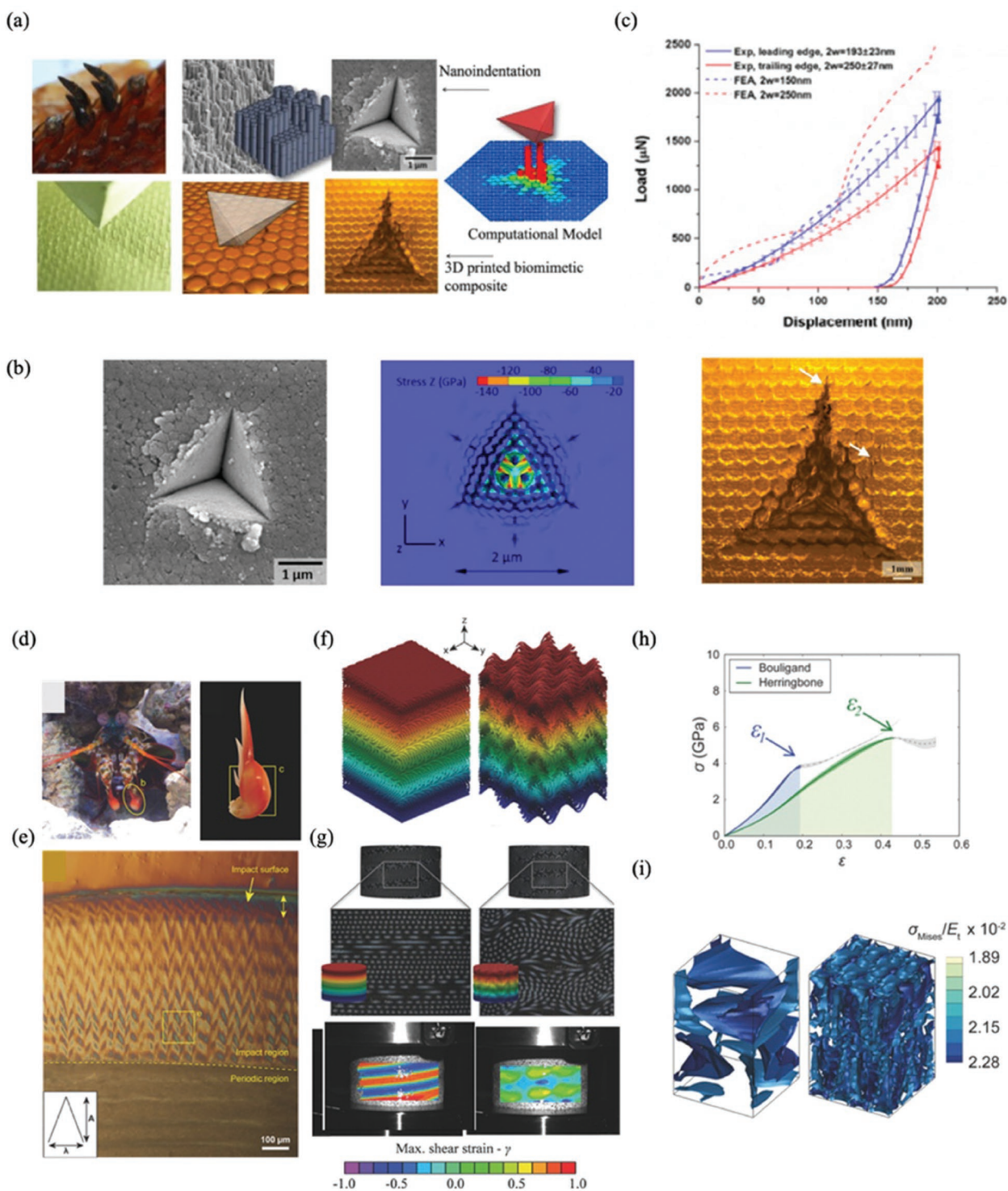


**Figure 16.** a) Radular teeth of the chiton, *Cryptochiton stelleri*. Schematics of an experimental/ computational/ prototyping/ analysis framework. b) Comparison of indentation marks at the leading edge of the tooth with finite element simulations and validating experiments using 3D printed structures. c) Indentation data of experimental curves at the leading and trailing edges compared with the elastic-plastic FEM. d) Anterior view of the stomatopod, *Odontodactylus scyllarus*, and view of the dactyl club separated from its raptorial appendage. e) Higher-magnification differential interference contrast image from a sagittal section of the dactyl club. f) Schematics of the geometry and fiber orientation for the Bouligand and herringbone structures. g) Digital image correlation showing the strain redistribution in 3D printed samples with Bouligand and herringbone patterns. h) Compression tests of the 3D printed samples highlighting the increased toughness of the herringbone structure over the Bouligand structure. i) Results from finite element simulations show redistribution of the von Mises stress in the Bouligand structure compared with the herringbone pattern. a,b-right) Adapted with permission.<sup>[106]</sup> Copyright 2015, Elsevier. b-left,b-middle, c) Reproduced with permission.<sup>[74]</sup> Copyright 2014, Wiley-VCH. d-i) Reproduced with permission.<sup>[70]</sup> Copyright 2016, Wiley-VCH.

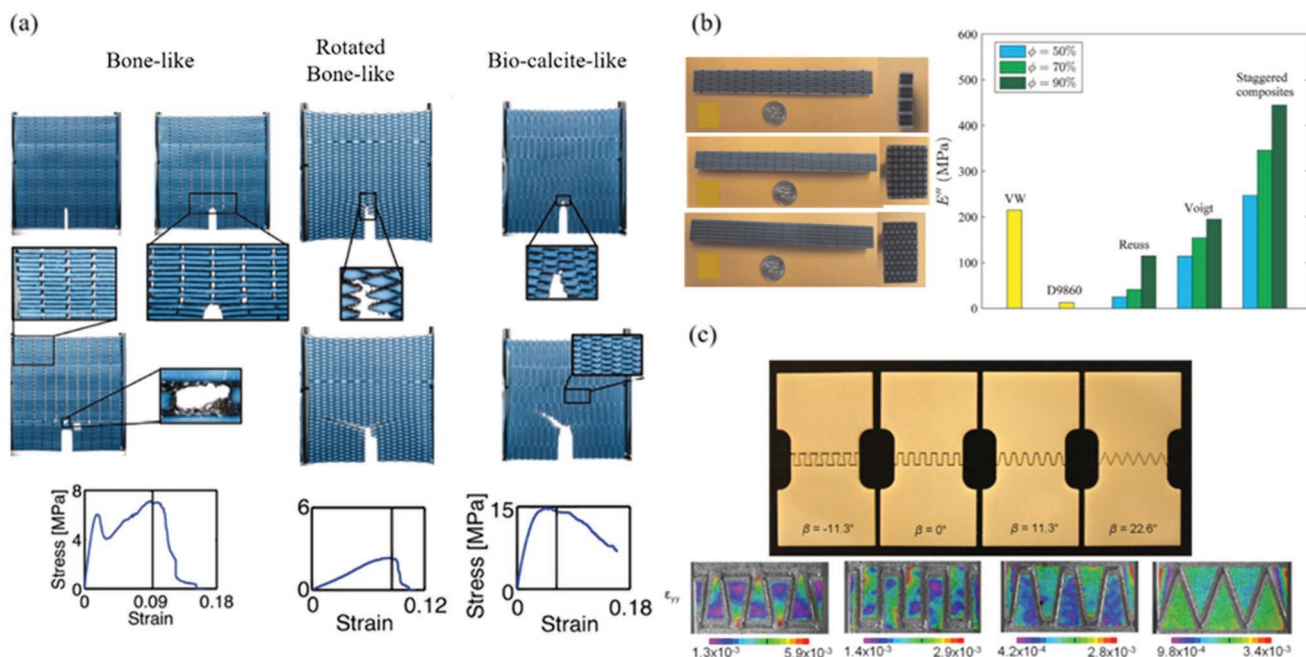


**Figure 17.** Additive manufacturing provides and allows easy comparison of the mechanical behavior between different ultrastructures. a) Fracture toughness evaluation of bone-like, rotated bone-like, and bio-calcite-like 3D printed composites. Reproduced with permission.<sup>[12c]</sup> Copyright 2013, Wiley-VCH. b) Damping evaluation of soft matrix/hard fiber composites inspired in nacre and bone structures. Reproduced with permission.<sup>[107]</sup> Copyright 2015, Elsevier. c) Evaluation of the mechanical performance of bioinspired sutures with trapezoidal, rectangular, antitrapezoidal, and triangular shapes. Reproduced with permission.<sup>[108]</sup> Copyright 2014, Elsevier.

larger deformations under compressive load which ultimately translates into more energy absorption when compared with the Bouligand structure. These results are key in providing new inspiration and design guidelines for the fabrication of next-generation impact-resistant composite materials.

Another advantage of using 3D printing as a modeling tool is that it allows easy comparison of the overall mechanical response of different ultrastructures. For example, in ref. [12c] mechanical tests were performed to determine the fracture toughness of 3D printed composites mimicking the structure of the bone, rotated bone, and biocalcite were performed showing that these microstructures allow to redistribute the stress and strain, and can scale the toughness of its constituents up to 20 times (Figure 17a). In ref. [107], the damping of 3D printed staggered composites with soft matrix and hard fibers based in the structure of the nacre and bone is compared with Reuss and Voigt models. Results from test and analytical models indicate that biological staggered composites exhibit enhanced damping responses that originate from large shear deformation on the matrix (Figure 17b). The influence on stiffness, strength, and toughness of bioinspired sutures is presented in ref. [108]. By tensile testing of 3D printed dogbone compounds with suture interfaces at the center of the gauge length with trapezoidal, rectangular, antitrapezoidal and triangular shapes, the authors determined that triangular waveforms are optimal for high stiffness, strength, and toughness and allows uniform distribution of the stress (Figure 17c).

In a more recent work, Suksangpanya et al.,<sup>[109]</sup> revealed additional details of the mechanical advantages of the Bouligand architecture from the dactyl club of the smashing mantis shrimp. Experimental observations highlighted its capability to

withstand repetitive high-energy impact without exhibiting signs of catastrophic failure. In fact, the initial experimental findings by Weaver et al. using electron charge contrast imaging in SEM, as well as experimental observations of polished and fractured surfaces have shown that cracks tend to form multiple nested twisting cracks that developed between the fibers of the Bouligand architecture. These twisting cracks are just a manifestation of the Bouligand template that guides these cracks to follow that pattern.<sup>[14a]</sup> The initial results presented by Weaver et al. on the mantis shrimp<sup>[14a]</sup> and Grunfelder et al. using biomimetic carbon fiber composites<sup>[152]</sup> were combined with the analytical, computational, and 3D-printing results by Suksangpanya et al.<sup>[109]</sup> to unveil the role of crack twisting in the overall fracture toughness of the Bouligand architecture. This was achieved through carefully designed specimens in which the crack propagation path was controlled (Figure 18a–c). These tests were able to replicate the same type of crack twisting patterns found in the actual dactyl club (Figure 18d–f).<sup>[14a]</sup> Carefully designed 3D printed beams together with computational analysis using finite elements and cohesive zone model were used to explore the nature of crack propagation (Figure 18g–h). As a result of the computational analysis, Suksangpanya et al. concluded that twisting cracks growing along a Bouligand architecture tend to grow faster in the direction parallel to the rotational axis (e.g., rotational axis is the axis perpendicular to the fiber layers). These results agree well with the theoretical models and provided additional insights into the fracture behavior of Bouligand structures. Moreover, this study revealed that changes in the local fracture mode at the crack front is expected to lead to a reduction of the local strain energy release rate, which translates to an increase in

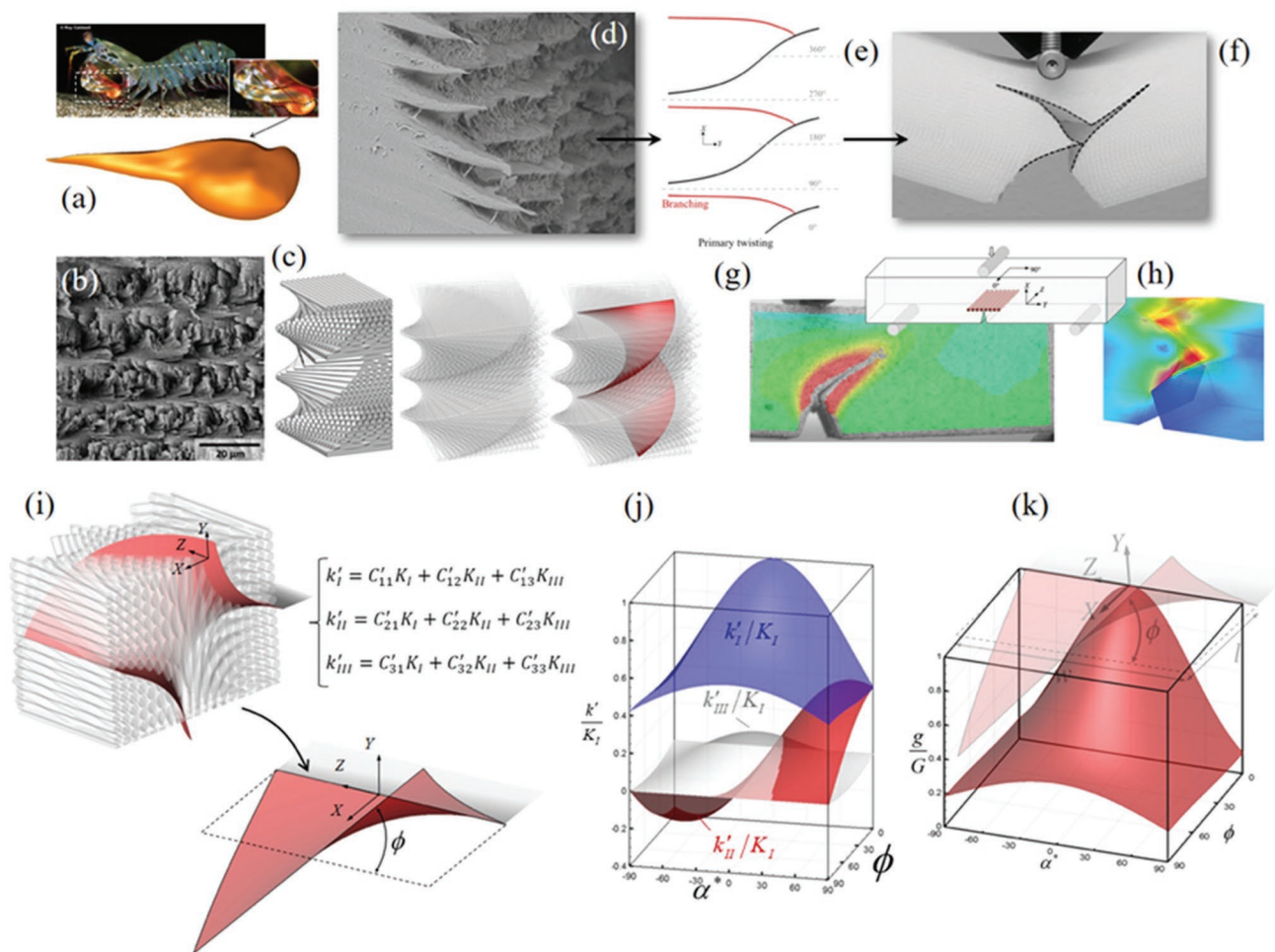


**Figure 18.** a) Photograph of mantis shrimp and its raptorial appendage, highlighting the location of dactyl club. b) SEM micrograph of the fractured transverse section of the periodic region. c) 3D schematic of the Bouligand structure identified in the periodic region of the dactyl club showing the potential crack twisting mechanism. d) Fractured flexural specimen of the Bouligand structure after being loaded under 3-pt bending. High magnification micrograph of the crack, showing periodic zigzag crack twisting. e) Crack twisting pattern in an infinite domain of a helicoidal structure estimated from the experimental observation. f) Similar crack pattern found in the 3D printed models. g) Digital Image correlation strain distribution measured from the 3D printed samples. h) Comparison with the computational models. i) General description of the analytical models proposed by Suksangpanya, 2017. j) Local stress intensity factor at the crack front of a twisting crack. k) General energy release rate or driving force of a twisting crack. a–h) Reproduced with permission.<sup>[109b]</sup> Copyright 2018, Elsevier; i–k) Reproduced with permission.<sup>[109a]</sup> Copyright 2017, Elsevier.

the necessary energy release rate required to propagate the crack (Figure 18k). Additionally, the driving force is also reduced as a function of the distance from the rotation axis of the twisting crack, making it more difficult for the crack to grow laterally. In turn, these results indicated that a single twisting crack tends to isolate itself and therefore does not promote the coalescence with other growing twisting cracks leading to delocalization and local hardening, helping the spread of damage. Future work using similar concepts have given positive results in intrinsically brittle 3D printed materials.<sup>[110]</sup> However, the analysis of larger systems will require more powerful computational tools, such as discrete element methods, or coarse grained models.<sup>[104]</sup>

Discrete and coarse-grained models to consider larger computational domains are beginning to exhibit the potential to study biological and bioinspired materials.<sup>[10e,104,111]</sup> Recently Barthelat and co-workers have developed a discrete element method (DEM) approach to validate some of the hypothesis

established by previous modeling work.<sup>[10a,72b,105]</sup> The discrete element method allowed them to consider larger representative volume elements (RVE)<sup>[111]</sup> (Figure 19). These models enable the analysis of statistical variations on the fracture mechanisms such as different tablet arrangements, variations in the interface properties, etc. One of the main conclusions of this work was that indeed hardening is an important component to promote delocalization of damage. In fact, local hardening provides the necessary components to promote multiple site crack initiation and growth leading to larger regions of damage and energy dissipation. They also found that these statistical variations, enabled by the DEM model, leads to increased toughness. However, such variations have a lower and upper bound: that is, low statistical variations lead to localization, and large variations lead to weaker structures. Moreover, DEM models allow to reduce the level of complexity achieved by high-fidelity finite element models, and yet can have the necessary details

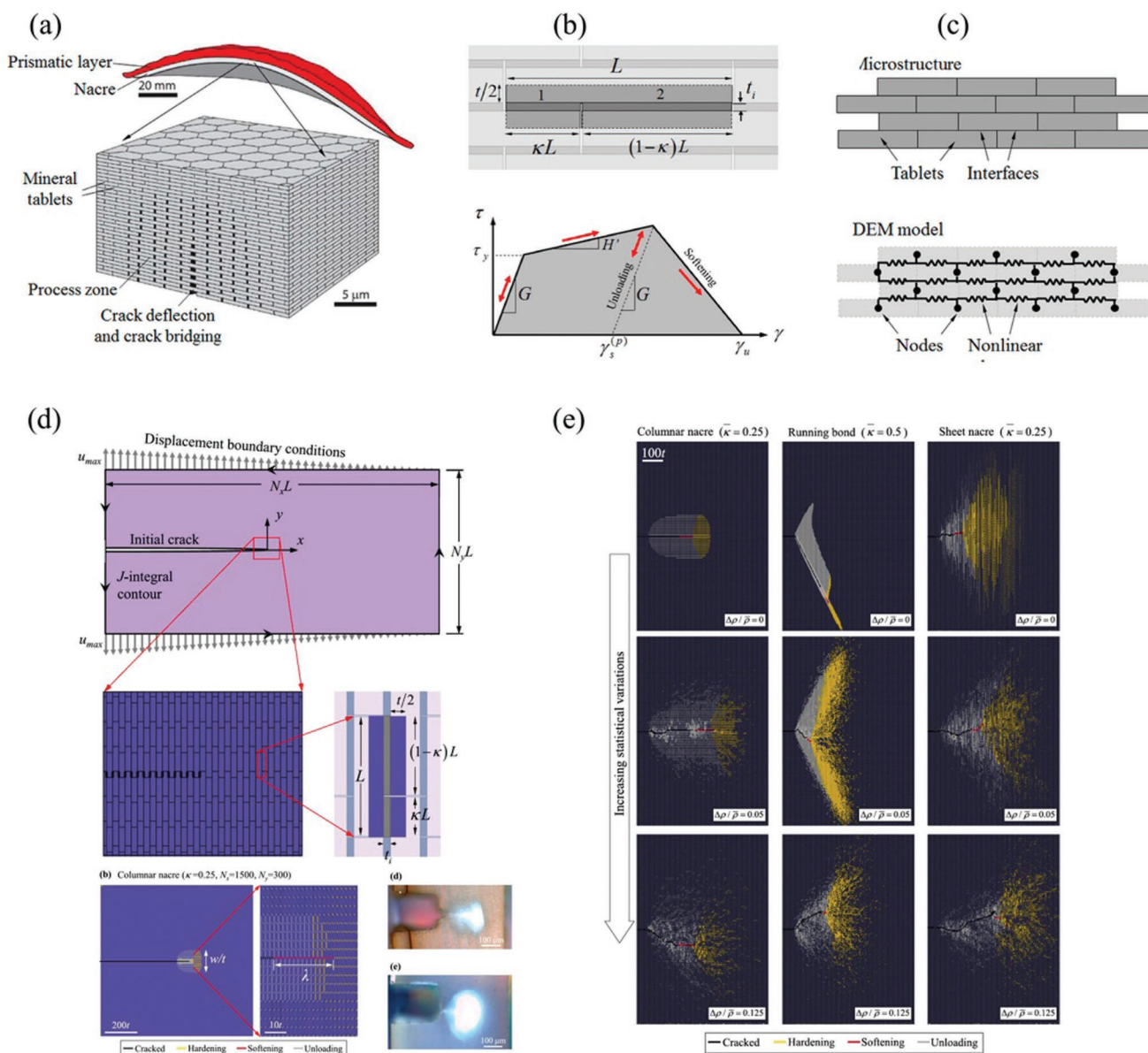


**Figure 19.** a) Staggered structure in nacre showing the delocalization effect around the main crack tip. b) Single cell RVE with key dimensions, and shear stress–strain behavior of the interfaces with local hardening. c) 1D DEM representation of the staggered structure based on (b). d) Fracture specimen problem definition and comparison with experiments showing the spread of damage around the crack tip. e) Snapshots of the DEM simulations with different degrees of statistical variations and different types of behaviors, clearly showing the delocalization effect around the crack tip. a–c) Reproduced with permission.<sup>[111a]</sup> Copyright 2018, Elsevier. d,e) Reproduced with permission.<sup>[111b]</sup> Copyright 2019, Elsevier.

or “ingredients” of the hypotheses that need to be evaluated. In the particular case of Barthelat’s work, DEM is a powerful tool that can be applied to extend existing design guidelines of brick and mortar structures.<sup>[10a,e,112]</sup>

## 7. Bioinspired Designs at Different Length-Scales

The biological materials with multiscale toughening mechanisms found in Nature present a wealth of ideal paradigms about how materials can be made strong and tough using simple building elements—this differs markedly from the general

design protocol of man-made materials where the properties stem largely from the complexity of chemical compositions or constituents. The lessons generated from these natural systems may provide significant inspiration and potential for developing outstanding properties in artificial materials, especially for solving the problem of embrittlement encountered in many high-strength materials<sup>[1a,5a,113]</sup> The idea of bioinspired design is not confined to a rigid mimicry of the structural intricacy of biological materials; indeed, it extends to the translation into man-made materials of the underlying design motifs at multiple length-scales, particularly those responsible for the extraordinary properties of biological materials.<sup>[114]</sup>

The realization of such designs relies essentially on the desired architectural construction and control of material characteristics, especially over different length-scales. This necessitates though an improved exploitation of the well-established materials processing methods and the development of new processing techniques.

### 7.1. Freeze Casting and Slip Casting for Microscale Control

Freeze casting, also known as ice templating, presents an effective approach for fabricating bioinspired materials

with layered or laminated architectures, specifically mimicking nacre.<sup>[12a,115]</sup> During the directional freezing process, the inclusions in an aqueous suspension are continuously expelled from the growing ice crystals into the microspaces between them, as shown in **Figure 20a**. The subsequent freeze drying and sintering (in the case of metal or ceramic systems) processes create scaffolds with aligned pores that replicate the ice crystals. The nano- to microscale structural characteristics of the scaffolds, including the lamellar thickness and interlamellar spacing, the nanoasperities growing on the lamellae, and the interconnectivities between lamellae, can be readily modulated during the freezing process. This can be realized

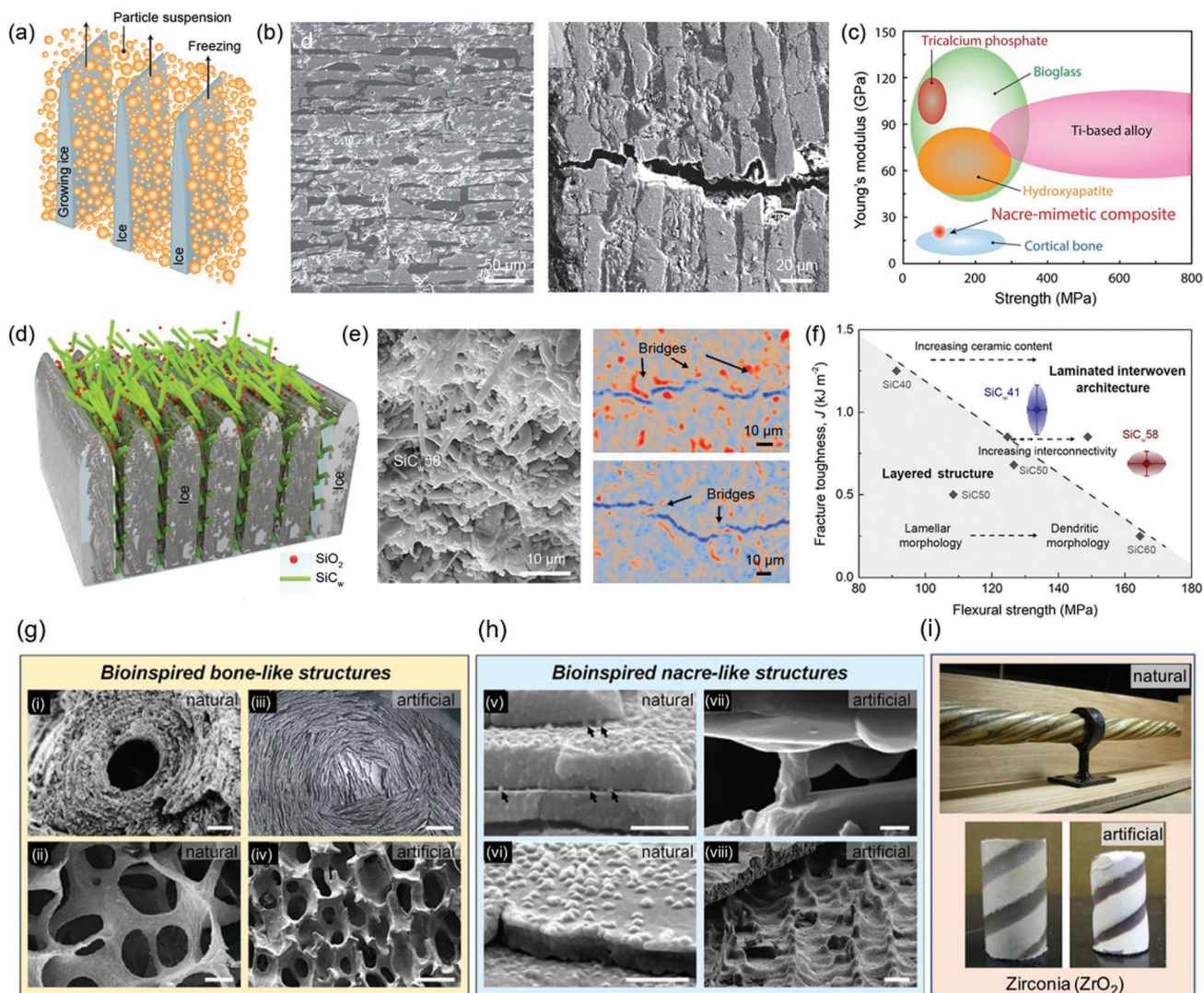


**Figure 20.** Bioinspired designs at nano- to microlength scales by freeze casting. a) Illustration of the self-assembly process of freezing suspension at the growing ice front. b) Brick-and-mortar structure of nacre-like hydroxyapatite–PMMA composites and its effect in resisting crack propagation. c) The mechanical properties of nacre-like hydroxyapatite–PMMA composites and its comparison with other commonly used implant materials. d) Illustration of the realignment of high-aspect-ratio constituents in suspension during the freezing process. SiC<sub>w</sub> refers to silicon carbide whiskers. e) Laminated interwoven architecture of freeze-cast scaffold and the toughening mechanisms of infiltrated composites visualized by X-ray tomography. f) Strength-toughness combinations of silicon carbide–PMMA composites with bioinspired laminated interwoven architectures and layered structures. g,h) Comparison of actual and artificial bone (g) and nacre (h). Scale bars: i) 20  $\mu\text{m}$ ; ii) 250  $\mu\text{m}$ ; iii) 500  $\mu\text{m}$ ; iv) 50  $\mu\text{m}$ ; v) 500 nm; vi) 600 nm; vii) 600 nm; and viii) 10  $\mu\text{m}$ . i) Museum specimen of narwhal tusk and narwhal tusk inspired scaffold made using magnetic freeze casting. a) Adapted with permission.<sup>[5a]</sup> Copyright 2015, Springer Nature. b,c) Adapted with permission.<sup>[12d]</sup> Copyright 2016, Wiley-VCH. d–f) Adapted with permission.<sup>[117b]</sup> Copyright 2019, American Chemical Society. g,h) Reproduced with permission.<sup>[156]</sup> Copyright 2013, Springer. i) Reproduced with permission.<sup>[121]</sup> Copyright 2012, Elsevier.

by controlling the processing parameters, e.g., the solid concentration and viscosity of slurry, the kinds and contents of additives, the cooling rate, and external fields during freezing.<sup>[115a–d,116]</sup>

Ceramic scaffolds can be directly used as reinforcements to strengthen and toughen materials by liquid infiltration of them with polymers or metals. Nacre-like lamellar composites have been fabricated following such routes, for example, in alumina–PMMA,<sup>[12a,115e]</sup> silicon carbide–PMMA,<sup>[117]</sup> alumina–aluminum alloy,<sup>[115g]</sup> and titanium carbide–aluminum alloy<sup>[118]</sup> systems. These composites outperform the simple mixtures of their constituents in terms of the strength–toughness combinations owing to the replication of the nano- to microscale structures of nacre and, in particular, the introduction of potent toughening strategies, including the inelastic deformation of the ductile phase, the crack deflection along interfaces, and the uncracked-ligament bridging in the crack wake.

The mechanical properties of the nacre-like composites by freeze casting can be further improved by densifying the scaffolds before infiltration and increasing the interfacial bonding strength between constituent phases. A prime example is the alumina–PMMA composites which possess ceramic contents up to 80 vol.% and display strong interfaces by grafting.<sup>[12a,115e]</sup> The composites exhibit brick-and-mortar architecture with abundant bridges of micrometer and sub-micrometer dimensions existing between the alumina bricks. This resembles the multiscale structural designs of nacre to a larger extent as compared to the lamellar composites.<sup>[119]</sup> In addition to the toughening effects by the extrinsic mechanisms of crack deflection and bridging, interfacial sliding is permitted within the polymeric phase but is restricted by the limited interfacial thickness, the pre-existing mineral bridges, and the roughness of the ceramic interfaces, thereby leading to efficient energy dissipation. This endows the composites with characteristic *R*-curve behavior and excellent fracture toughness that is markedly higher than its constituents—the toughest alumina material reported to date. Similar approach has also been employed in fabricating nacre-like hydroxyapatite–PMMA composites,<sup>[12d]</sup> as shown in Figure 20b). The resultant materials exhibit unique Young's modulus and strength similar to human cortical bone in combination with high work of fracture (as shown in Figure 20c), thus demonstrating a potential for applications as bone replacements.

In the case of particles with high aspect ratio and large anisotropy in the slurry, the particles can be reorganized by the encapsulating force generated from the moving ice front during the freeze casting process,<sup>[115b,c]</sup> as illustrated in Figure 20d. The long axes of particles are preferentially realigned to be parallel to the growing ice profile. This offers the possibility for building new bioinspired architectures by mimicking other biological materials in addition to nacre via freeze casting. A good case in point is the silicon carbide composites containing PMMA as a compliant phase inspired by the crustacean exoskeleton.<sup>[117b]</sup> Silicon carbide whiskers and minimal nanometer-sized silica are utilized to make the suspension for freeze casting; the former are realigned by the freezing ice with the latter forming nano-interconnectivities between the whiskers in the sintering process (Figure 20e). The resultant composites after infiltration display nano- to microscale architectures replicating the main

structural designs of crustacean exoskeleton, i.e., the laminated arrangement of constituents, the varying orientations within laminates, and the three-dimensional interconnection.<sup>[117b,120]</sup> This creates an enhancement of crack deflection/twisting in the composites and uncracked-ligament bridging by fiber or fiber bundles (Figure 20e), as compared to the layered composites mimicking nacre (Figure 20e),<sup>[117a]</sup> thus resulting in more superior strength–toughness combinations (Figure 20f).

Microstructural alignment in freeze casting can be controlled through extrinsic methods, such as external fields, to improve compressive mechanical properties in the direction of alignment. This has been shown in magnetically aligned scaffolds studied by Porter et al.<sup>[121]</sup> Magnetic alignment has also been used to create two directions of lamellar alignment as seen in trabecular bone.<sup>[122]</sup> In addition to synthesizing bioinspired bone and nacre (Figure 20g,h), freeze casting has been used to create a bioinspired narwhal tusk (Figure 20i) that showed enhanced torsional resistance due to the helical reinforcement.<sup>[121,123]</sup> Electric fields have also been used to increase pore size in hydroxyapatite scaffolds<sup>[124]</sup> or increase scaffold wall thickness in alumina scaffolds.<sup>[125]</sup> Electrophoretic deposition was found to create fine lamellar structure in scaffolds.<sup>[126]</sup> Finally, recent work has been done on ultrasound-controlled freeze casting to create concentric ring structures with high and low porosity rings,<sup>[127]</sup> opening up many avenues to control hierarchical features at the microscale.

Freeze casting has also been used for biomedical applications since microscale porosity is essential for nutrient flow and cell proliferation and macroscale porosity is required for vascularization. Bai et al.<sup>[128]</sup> created hierarchical, bioinspired nacre by freeze casting a hydrogel with dispersed clay platelets to form aligned platelets at the nanometer scale and polymer lamellae at the microscale. The improved mechanical performance, porous structure, and thermoresponsive property of the hydrogel component make this composite promising for use in controlled drug release and smart scaffolds. Porous hydroxyapatite scaffolds which possess micropores (1–10 μm) and macropores (90–110 μm) by changing the solvent compositions (water–glycerol for micropores and water–dioxane for macropores) have been reported.<sup>[129]</sup> More recently, collagen was freeze cast to create scaffolds for permanent female sterilization that was tested on successfully with rats.<sup>[130]</sup> The effect of processing conditions was further tested and showed that lower freezing rate produced larger pores and thicker lamellar walls, resulting in decreased modulus but higher yield strength.<sup>[131]</sup> Across multiple materials, freeze casting has showed promise for creating controlled micro- and macroporosity.

A significant shortcoming to freeze casting is its reproducibility, which has been shown to be poor in a study on zirconia slurry freeze casting, since the properties between samples with the same processing conditions exhibited statistically significant differences.<sup>[132]</sup> Therefore, more work needs to be done to fine-tune the freeze casting process to achieve the reproducibility needed for engineering applications. Additionally, the samples dimensions are limited by homogeneity of temperature fields, which inhibits the scalability of freeze casting as a synthesis method.<sup>[133]</sup> Porosity morphologies and length scales are also limited by solid loading and its effect on solidification kinetics.<sup>[134]</sup>

Another promising strategy to control the multiscale architectures of man-made composites is to regulate the orientation and local distribution of anisotropic constituents in suspension using external magnetic fields followed by consolidation of the fluid phase.<sup>[135]</sup> This necessitates the constituents to be magnetically responsive which can be realized by surface decoration using superparamagnetic nanoparticles, such as iron oxide. Such method has been proven to be effective in modulating the local reinforcements of polymer-based composites such as to generate tailored properties, e.g., strength, wear resistance, and even shape-memory effects.<sup>[135b-d]</sup> The combination of this technique with the aqueous-based slip casting process offers new possibilities for the efficient fabrication of heterogeneous composites in bulk size and complex shapes and with varying types of matrices, i.e., ceramic, metal and polymer.<sup>[136]</sup> The multiscale architectures of composites can be finely programmed to implement various bioinspired designs, potentially as intricate as the tooth-like bilayer components with site-specific composition/texture and the periodic patterns of microreinforcement orientation.

## 7.2. Multiscale Designs Using Additive Manufacturing

Additive manufacturing (AM), as represented by 3D printing, has become a popular tool for studying the features that give rise to the exceptional mechanical properties of biological materials at different length-scales. In particular, AM has been useful for studying architectures of composites and structures since it provides design and material property flexibility. The most commonly used printers are extrusion or UV-cured polymer-based printers. Multimaterial printers can blend different polymers to achieve more fine-tuned material properties.<sup>[137]</sup> However, given that the field is still immature, there are shortcomings and artifacts present in the resulting prints. For example, Yap et al.<sup>[138]</sup> found that dimensional accuracy was dependent on printing orientation, position on the printing surface, and surface finish of the print (glossy or matte). Material properties of 3D printed materials are dependent on print conditions, AM technique used, dimensions of the sample, and other factors.<sup>[139]</sup> In addition, little is known about the interface properties between separate materials that are printed simultaneously. Nonetheless, AM has become a unique tool for exploring microstructural features that provide strengthening and toughening mechanisms in bioinspired materials.

Among AM tools, 3D printing has presented great advantages for rapid construction of complex 3D architectures and shapes out of a variety of materials.<sup>[12c,135d,140]</sup> This technique has been utilized to recreate bioinspired macroscale structures. At the macroscale, a 3D printed seahorse tail with a square cross-section was mechanically tested and compared to a 3D printed model with a round cross-section (**Figure 21a**).<sup>[96b]</sup> The mouth structure of the sea urchin (Aristotle's lantern), was also prototyped using AM to adapt the design for use as a sediment sampler.<sup>[141]</sup> The keel feature of Aristotle's lantern was modeled and found to contribute to the resilience of the sea urchin tooth. The impact resistance through stress deflection in the woodpecker skull was explored by placing a 3D printed woodpecker skull in a drop tower apparatus shown in **Figure 21a,b**.<sup>[142]</sup> The

influence of a structural feature known as the frontal overhang was investigated by producing two types of additively manufactured prototypes: one with the frontal overhang present and one without. Fish scales have inspired some designs exploring puncture resistance and flexibility tradeoffs.<sup>[143]</sup> The effect of arrangement of 3D printed fish scales (**Figure 21c**) on puncture resistance was tested, showing that minor differences in angle and geometry of scales can influence puncture resistance significantly.<sup>[143b]</sup> One of the shortcomings to multimaterial 3D printers, which have been used for many microstructural studies, is that they are generally most available for printing polymers. 3D printed polymers have a limited disparity in modulus that cannot accurately represent the differences in stiffness between natural organic and inorganic phases. Additionally, printing resolution is limited and is unable to reflect the increase in strength of nanoscale inorganic crystals that arise from increased ratio of defects at the nanoscale. Finally, the size and scale effects of samples have not been thoroughly examined. However, this technology is fast moving and continued improvements in printers and inks are currently in development.

At the microstructural level, 3D printed materials inspired by nacre and bone have been tested to better understand their fracture toughness,<sup>[12c,144]</sup> impact resistance,<sup>[145]</sup> and energy dissipation mechanisms.<sup>[107]</sup> A 3D printed nacre-inspired composite showed that the mineral bridges in nacre play an important role in maintaining stiffness and improving toughness.<sup>[146]</sup> In addition, the incorporation of an additional level of hierarchy in a nacre-inspired design is demonstrated, shown in **Figure 21d–g**, with an improved impact resistance in an higher level of hierarchy sample.<sup>[147]</sup>

In addition to microscale and macroscale feature printing capabilities, the potency of such approach in architectural regulation of composites at multiple length scales, especially down to finer dimensions, can be significantly strengthened by coupling with the real-time colloidal assembly directed by magnetic fields.<sup>[12b,148]</sup> By applying programmable magnetic fields in 3D printing platform (**Figure 22a**) and using active material (e.g., ink) containing magnetically responsive constituents (**Figure 22b**), the orientation of reinforcements can be precisely controlled during the printing process in tiny space down to each individual voxel, as illustrated in **Figure 22c**.<sup>[148a]</sup> This technique, termed as 3D magnetic printing, makes it possible to realize complex bioinspired designs, as exemplified by the architectures mimicking the abalone shell, the dactyl club of mantis shrimp and the bone osteon, in developing enhanced material properties. In particular, such modulation can be operated at a series of different length-scales, as represented by the hierarchy of the printed block shown in **Figure 22d**. This allows for an effective architectural manipulation ranging from the micro-/nanostructures to macroscopic shapes and geometries, thereby enabling the translation of multiscale toughening mechanisms of biological materials into man-made systems.

In a recent review, Velasco-Hogan et al.<sup>[17a]</sup> provide a framework for using AM for bioinspiration. This process involves using AM to optimize designs inspired from Nature. First, inspiration from Nature is used to create a design template. It is then fabricated using AM to create 3D printed prototypes.

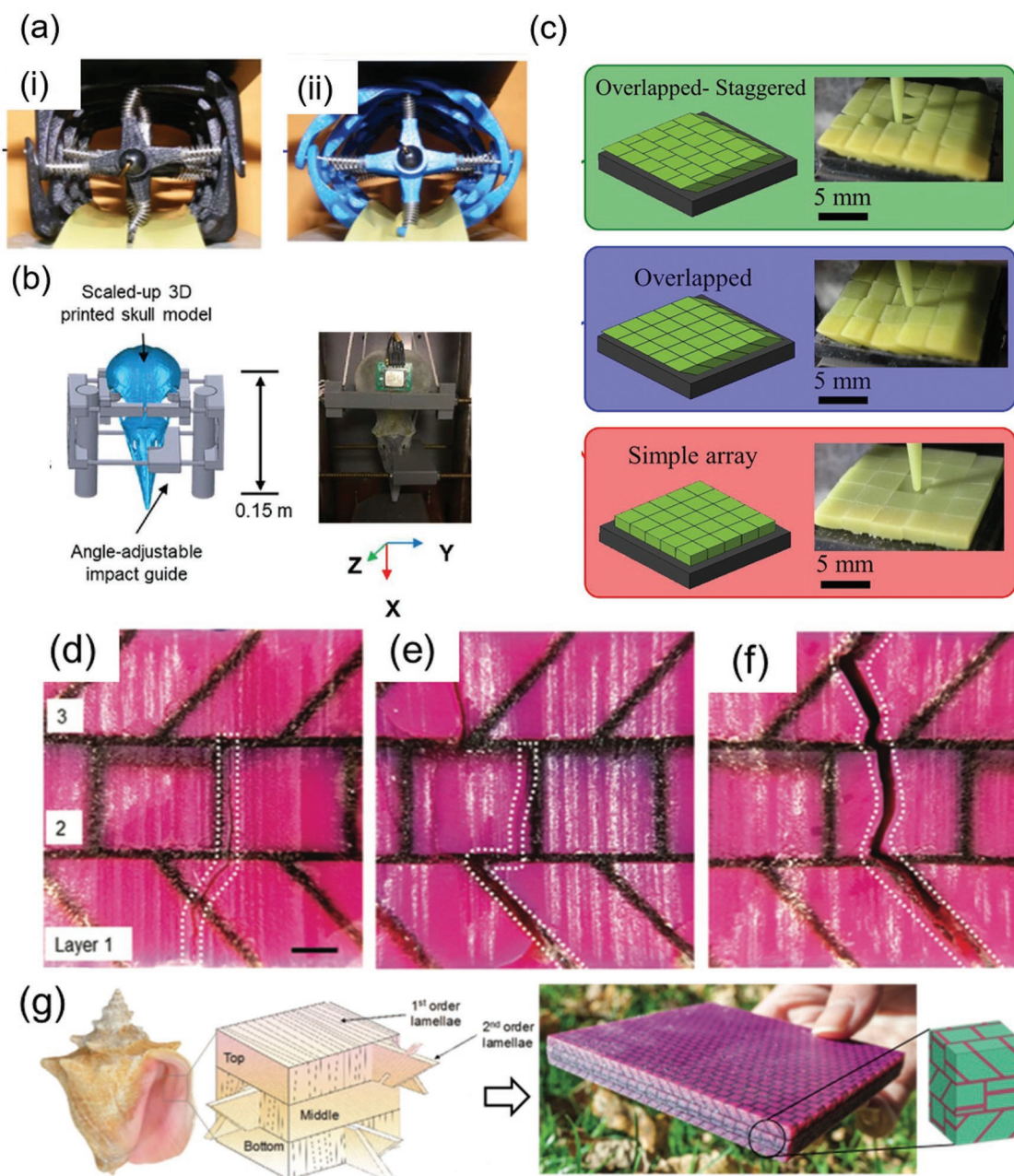


**Figure 21.** a) 3D printed square cross-section seahorse tail and round cross-section model as a comparison. b) Model and photograph of a 3D printed woodpecker skull in an angle-adjustable impact guide for use in a custom drop tower. c) 3D printed scale arrays for puncture testing. Nacre inspired 3D printed composite with two layers of hierarchy, showing the following crack paths of the same sample type: d) a crack that is deflected by the soft interface in layer one and is arrested in layer 2, e) a crack that follows the soft interface in layers 1 and 2 and changes direction in layer 3, and f) a crack that propagates from layer 1 to part of layer 3. Scale bar is 1 mm. g) Schematic of conch shell hierarchy and photograph of overall 3D printed composite. a) Reproduced with permission.<sup>[96b]</sup> Copyright 2015, American Association for the Advancement of Science. b) Reproduced with permission.<sup>[142]</sup> Copyright 2019, Wiley-VCH. c) Reproduced with permission.<sup>[143b]</sup> Copyright 2017, Elsevier. d–g) Reproduced with permission.<sup>[147]</sup> Copyright 2017, Wiley-VCH.

Characterization through mechanical testing then allows optimization of the template design to take place and refinement or optimization of these designs with subsequent testing help researchers to further understand biological materials and therefore, engineering designs. While more work is needed to increase the reliability of printing processes, AM has already proved itself to be irreplaceable as a technique for exploring biological materials and their toughening mechanisms.

### 7.3. Other Bioinspired Synthesis Methods

In addition to freeze casting and AM, a few other techniques have been used to create bioinspired materials. Laser etching of glass combined with polyurethane infiltration can increase toughness of glass composites<sup>[149]</sup> (Figure 23a). These materials are easy to pattern and manufacture compared to laminated composites. Laser etched composites displayed deformation

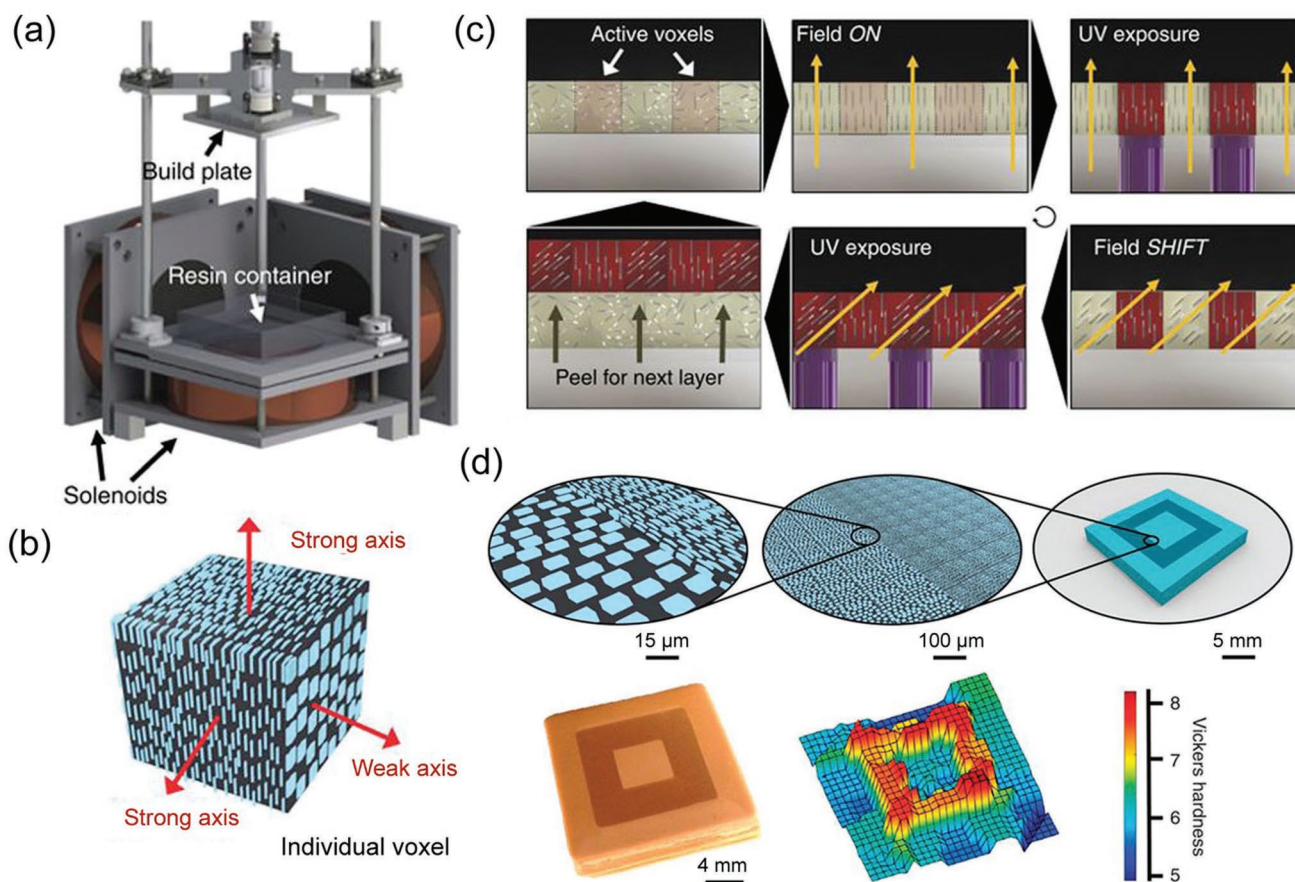


**Figure 22.** 3D magnetic printing technique for recreation of bioinspired multiscale structures. a) 3D magnetic printer setup equipped with electromagnetic solenoids to allow for the application of magnetic fields. b) Schematic of an individual voxel containing oriented reinforcement microplatelets by magnetic fields. c) 3D magnetic printing process involving repeated steps of the programmed alignment of reinforcements within active voxels using magnetic fields, the polymerization of the matrix by ultraviolet (UV) exposure, and the successive printing of additive layers. d) The multiscale structure and site-specific hardness of a block containing a concentric square pattern fabricated by 3D magnetic printing. a–d) Adapted with permission.<sup>[148a]</sup> Copyright 2015, Springer Nature.

mechanisms seen in nacre and have increased toughness. Drawing inspiration from fish scales and arthropod cuticles, this technique has also been used to create crossply patterns in glass-polymer composites.<sup>[150]</sup> These composites allow large deformation and avoid brittle fracture when compared to standard laminated glass while maintaining transparency<sup>[150]</sup> (Figure 23b). Since transparency is not affected, there are a variety of engineering applications for this laser etched glass composite, including use in car windshields to localize damage. Laser etching has also been used to create trenches in aluminum oxide plates to channel cracks to certain paths, a phenomenon seen in many biological materials such as bone, teeth, and mollusk shells.<sup>[151]</sup> These bioinspired designs increase toughness by guiding and localizing damage in the material. This has also been shown in fiber-reinforced composites mimicking the Bouligand structure of the mantis shrimp dactyl club.<sup>[152]</sup> As seen in the 3D printed Bouligand structure described previously,<sup>[109b]</sup> mantis shrimp inspired fiber-reinforced composites (Figure 23c) display a crack redirection behavior, and impact tests of the helicoidal composites demonstrated reduced dent depth when compared to quasi-

isotropic control specimens.<sup>[152]</sup> Finally, the woodpecker head served as inspiration for a high-shock-absorbing system for micromachined devices made using a conventional hard-resin method.<sup>[153]</sup> The hierarchical features in biological materials have generally been applied to engineering designs to increase damage tolerance with at most two levels of hierarchy. The next step in the field is to apply more than two levels of hierarchy in engineered materials to increase toughness and strength while better understanding biological materials.

## 8. Conclusions

Lightweight and high-performance nano- and microstructured materials that exhibit both strength and toughness are highly desirable for a number of applications including energy, defense, homeland security, industrial safety, medicine, and the aerospace and automotive industries. Researchers have been searching for solutions to address these challenges for decades. Nature has provided multiple examples of tough and strong biological materials found in both animal and plant species.

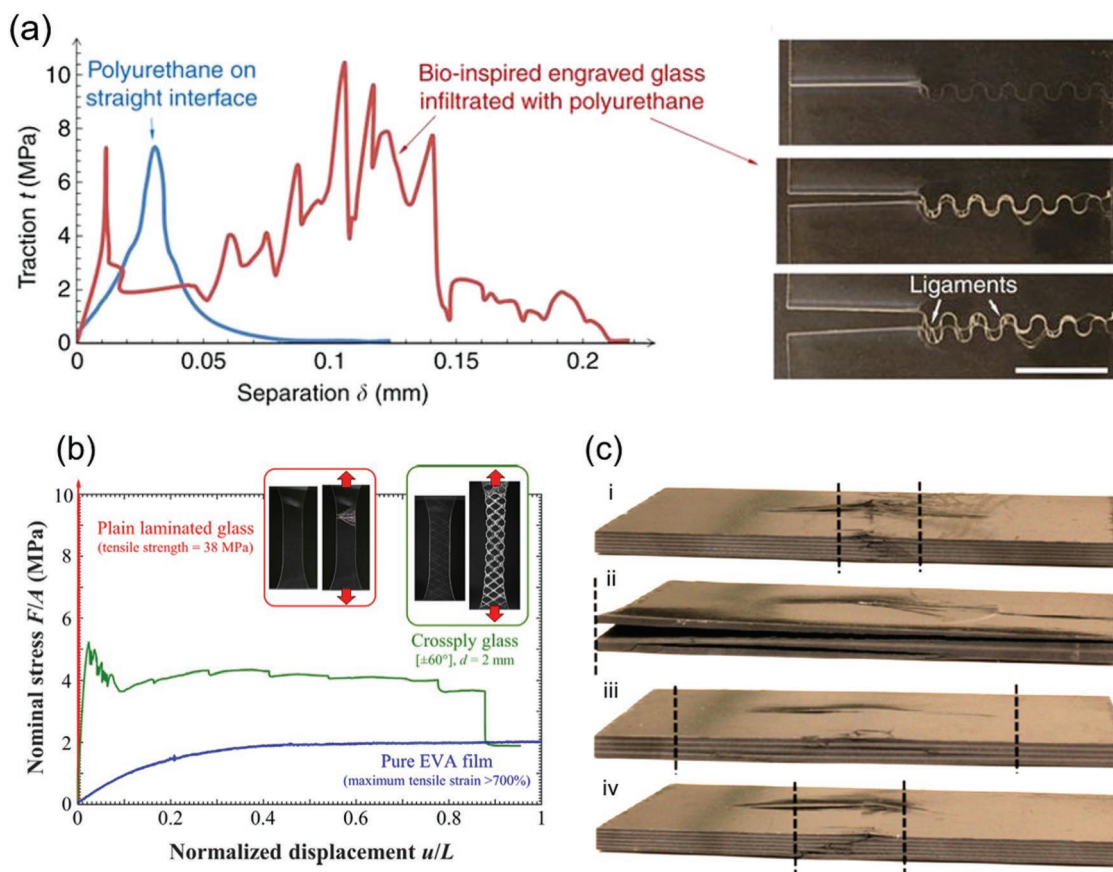


**Figure 23.** Other methods to create bioinspired materials. a) Traction-separation curves of nacre-inspired laser etched borosilicate glass infiltrated with polyurethane. b) Nominal stress versus normalized displacement of fish scale-inspired crossply glass. c) Damage from compression testing to i) quasi-isotropic, ii) small-angle, iii) medium-angle, and iv) large-angle composites. after compression tests. a) Reproduced with permission.<sup>[149b]</sup> Copyright 2014, Springer Nature. b) Reproduced with permission.<sup>[150]</sup> Copyright 2018, Elsevier. c) Reproduced with permission.<sup>[152]</sup> Copyright 2014, Elsevier.

Although these biological composites are constructed from a limited number of materials, they often demonstrate remarkable mechanical properties that are similar, and many times better than, mechanical properties of many engineering materials. These organisms have accomplished this often through a directed synthesis and a well-orchestrated hierarchical assembly of organic structures and nanoscale minerals. In the current work, characteristic features as well as the toughening mechanisms at multilength scales in representative organisms are identified and summarized. At the atomic-scale, macromolecule reconfiguration, deformation and phase transformation are common energy dissipation mechanism in biopolymers such as collagen, keratin, chitin and cellulose. Chemical bonds (hydrogen bonds) breakage and reforming are also important mechanisms. While in biominerals (calcium carbonate, hydroxyapatite, magnetite, silica), crystal imperfections such as dislocations, deformation twinning and amorphization caused by low strain-rate compressions or high strain-rate impacts are the main toughening mechanisms at the atomic scale. At the nanoscale, biopolymer nanofibrils composed of collagen, chitin, keratin, and cellulose fibrils straighten, reorient, stretch, and slide, while the combination of crystalline keratin intermediate filaments within an amorphous matrix can deflect

crack propagation. Biomineralized nanoparticles deform, rotate, and translate whereas nanoplatelets slide, and nanorods deflect cracks. In addition, there are multiple microscale features such as tubules, lamellae, and interfaces found deflecting and twisting crack propagation effectively. Plastic deformations of the tubular structures also show efficient energy absorption especially at high strain-rate impacts. The overall mechanical behavior and energy absorption of organisms at macroscale are related to their morphology and structural designs, which are also adaptations to the actual loading conditions in Nature. However, in order to validate these observations, a combination of simulation techniques as well as bioinspired processing has become increasingly popular to enable this understanding and create a link between theoretical descriptions and experimental characterization. Typically, the modeling of biological materials is performed one scale at the time; then, the collection of single-scale descriptions are used to provide practical descriptions of the material. These simulation methods are summarized in this review. In order to bridge the gap between natural materials and synthetic analogs, bioinspired processing methods have been developed. Bioinspired processing, including 3D printing and freeze casting methods provides a scalable pathway into man-made materials containing the underlying design motifs at multiple

length-scales, particularly those responsible for the extraordinary properties of biological materials. The realization of such designs relies essentially on the desired architectural construction and control of material characteristics, especially over different length-scales. This necessitates though an improved exploitation of the well-established materials processing methods and the development of new processing techniques. The combined analysis approach including experimental observation, computational models, and prototyping has accelerated our understanding of fundamental mechanisms, obtain quantitative information, and test hypotheses about the naturally occurring material. The combination of simulations and experiments with the natural material and bioinspired prototypes have given great insight to the delicate interplay between material parameters, microstructure, and size scale showing that, if all the aspects are optimally combined, novel synthetic materials with superior performance can be attained. Therefore, the design principles uncovered through this approach can provide key quantitative information for the development of a new generation of high-performance materials.

## Acknowledgements

All authors would like to acknowledge funding from the Air Force Office of Scientific Research, Multi-University Research Initiative (AFOSR-FA9550-15-1-0009). D.K. and P.Z. acknowledge funding from the Air Force Office of Scientific Research (AFOSR-FA9550-12-1-0245 and AFOSR-FA9550-12-1-0249). D.K. would like to also acknowledge funding from Army Research Office (ARO-W911NF-15-1-0306).

## Conflict of Interest

The authors declare no conflict of interest.

## Keywords

bioinspired designs, biological materials, computational modeling, multiscale materials, toughening mechanisms

Received: March 11, 2019

Revised: April 8, 2019

Published online: July 3, 2019

- [1] a) M. A. Meyers, J. McKittrick, P. Y. Chen, *Science* **2013**, 339, 773; b) P. Y. Chen, J. McKittrick, M. A. Meyers, *Prog. Mater. Sci.* **2012**, 57, 1492.
- [2] R. O. Ritchie, *Nat. Mater.* **2011**, 10, 817.
- [3] J. McKittrick, P. Y. Chen, L. Tombolato, E. E. Novitskaya, M. W. Trim, G. A. Hirata, E. A. Olevsky, M. F. Horstemeyer, M. A. Meyers, *Mater. Sci. Eng., C* **2010**, 30, 331.
- [4] U. Wegst, M. Ashby, *Philos. Mag.* **2004**, 84, 2167.
- [5] a) U. G. K. Wegst, H. Bai, E. Saiz, A. P. Tomsia, R. O. Ritchie, *Nat. Mater.* **2015**, 14, 23; b) M. F. Ashby, L. Gibson, U. Wegst, R. Olive, *Proc. R. Soc. A* **1995**, 450, 123; c) C. Salinas, D. Kisailus, *JOM* **2013**, 65, 473.
- [6] N. A. Yaraghi, A. A. Trikanad, D. Restrepo, W. Huang, S. Herrera, R. L. Caldwell, P. D. Zavattieri, D. Kisailus, *Adv. Funct. Mater.* **2019**, <https://doi.org/10.1002/adfm.201902238>.
- [7] M. A. Meyers, P.-Y. Chen, A. Y.-M. Lin, Y. Seki, *Prog. Mater. Sci.* **2008**, 53, 1.
- [8] M. E. Launey, R. O. Ritchie, *Adv. Mater.* **2009**, 21, 2103.
- [9] a) R. K. Nalla, J. H. Kinney, R. O. Ritchie, *Nat. Mater.* **2003**, 2, 164; b) R. K. Nalla, J. J. Kruzic, J. H. Kinney, R. O. Ritchie, *Biomaterials* **2005**, 26, 217.
- [10] a) F. Barthelat, H. Espinosa, *Exp. Mech.* **2007**, 47, 311; b) J. C. Weaver, Q. Q. Wang, A. Miserez, A. Tantuocci, R. Stromberg, K. N. Bozhilov, P. Maxwell, R. Nay, S. T. Heier, E. DiMasi, D. Kisailus, *Mater. Today* **2010**, 13, 42; c) E. E. de Obaldia, S. Herrera, L. K. Grunenfelder, D. Kisailus, P. Zavattieri, *J. Mech. Phys. Solids* **2016**, 96, 511; d) C. L. Salinas, E. E. de Obaldia, C. Jeong, J. Hernandez, P. Zavattieri, D. Kisailus, *J. Mech. Behav. Biomed. Mater.* **2017**, 76, 58; e) M. R. Begley, N. R. Philips, B. G. Compton, D. V. Wilbrink, R. O. Ritchie, M. Utz, *J. Mech. Phys. Solids* **2012**, 60, 1545; f) A. Y.-M. Lin, M. A. Meyers, *J. Mech. Behav. Biomed. Mater.* **2009**, 2, 607.
- [11] G. Noselli, V. S. Deshpande, N. A. Fleck, *Int. J. Fract.* **2013**, 183, 241.
- [12] a) E. Munch, M. E. Launey, D. H. Alsem, E. Saiz, A. P. Tomsia, R. O. Ritchie, *Science* **2008**, 322, 1516; b) D. Kokkinis, M. Schaffner, A. R. Studart, *Nat. Commun.* **2015**, 6, 8643; c) L. S. Dimas, G. H. Bratzel, I. Eylon, M. J. Buehler, *Adv. Funct. Mater.* **2013**, 23, 4629; d) H. Bai, F. Walsh, B. Gludovatz, B. Delattre, C. Huang, Y. Chen, A. P. Tomsia, R. O. Ritchie, *Adv. Mater.* **2016**, 28, 50.
- [13] a) S. Lee, E. E. Novitskaya, B. Reynante, J. Vasquez, R. Urbaniak, T. Takahashi, E. Woolley, L. Tombolato, P. Y. Chen, J. McKittrick, *Mater. Sci. Eng., C* **2011**, 31, 730; b) M. A. Meyers, *Dynamic Behavior of Materials*, John Wiley & Sons, Hoboken, NJ, USA **1994**.
- [14] a) J. C. Weaver, G. W. Milliron, A. Miserez, K. Evans-Lutterodt, S. Herrera, I. Gallana, W. J. Mershon, B. Swanson, P. Zavattieri, E. DiMasi, D. Kisailus, *Science* **2012**, 336, 1275; b) S. Amini, M. Tadayon, S. Idapalapati, A. Miserez, *Nat. Mater.* **2015**, 14, 943.
- [15] W. Huang, A. Zaheri, J.-Y. Jung, H. D. Espinosa, J. McKittrick, *Acta Biomater.* **2017**, 64, 1.
- [16] a) M. Schaffler, E. Radin, D. Burr, *Bone* **1989**, 10, 207; b) E. A. Zimmermann, B. Gludovatz, E. Schaible, B. Busse, R. O. Ritchie, *Biomaterials* **2014**, 35, 5472.
- [17] a) A. Velasco-Hogan, J. Xu, M. A. Meyers, *Adv. Mater.* **2018**, 30, 1800940; b) N. A. Yaraghi, D. Kisailus, *Annu. Rev. Phys. Chem.* **2018**, 69, 23.
- [18] a) P. Fratzl, *Collagen*, Springer, Berlin, Germany **2008**, p. 1; b) V. R. Sherman, W. Yang, M. A. Meyers, *J. Mech. Behav. Biomed. Mater.* **2015**, 52, 22.
- [19] W. Yang, M. A. Meyers, R. O. Ritchie, *Prog. Mater. Sci.* **2019**, 103, 425.
- [20] M. J. Buehler, *Nanotechnology* **2007**, 18, 295102.
- [21] S. M. Pradhan, D. R. Katti, K. S. Katti, *J. Nanomech. Micromech.* **2011**, 1, 104.
- [22] a) R. S. Erdmann, H. Wennemers, *Angew. Chem.* **2011**, 123, 6967; b) J. Bella, M. Eaton, B. Brodsky, H. M. Berman, *Science* **1994**, 266, 75; c) G. Ramachandran, R. Chandrasekharan, *Biopolymers* **1968**, 6, 1649.
- [23] P. Fratzl, K. Misof, I. Zizak, G. Rapp, H. Amenitsch, S. Bernstorff, *J. Struct. Biol.* **1998**, 122, 119.
- [24] a) J. B. Thompson, J. H. Kindt, B. Drake, H. G. Hansma, D. E. Morse, P. K. Hansma, *Nature* **2001**, 414, 773; b) W. Wang, A. Elbanna, *Bone* **2014**, 68, 20.
- [25] G. E. Fantner, E. Oroudjev, G. Schitter, L. S. Golde, P. Thurner, M. M. Finch, P. Turner, T. Gutschmann, D. E. Morse, H. Hansma, *Biophys. J.* **2006**, 90, 1411.
- [26] G. E. Fantner, T. Hassenkam, J. H. Kindt, J. C. Weaver, H. Birkedal, L. Pechenik, J. A. Cutroni, G. A. Cidade, G. D. Stucky, D. E. Morse, *Nat. Mater.* **2005**, 4, 612.
- [27] a) J. McKittrick, P.-Y. Chen, S. Bodde, W. Yang, E. Novitskaya, M. Meyers, *JOM* **2012**, 64, 449; b) B. Wang, W. Yang, J. McKittrick, M. A. Meyers, *Prog. Mater. Sci.* **2016**, 76, 229.

- [28] M. Kadir, X. Wang, B. Zhu, J. Liu, D. Harland, C. Popescu, *J. Struct. Biol.* **2017**, *198*, 116.
- [29] X. Xiao, J. Hu, *Sci. Rep.* **2016**, *6*, 26393.
- [30] Z. Liu, D. Jiao, Z. Zhang, *Biomaterials* **2015**, *65*, 13.
- [31] A. Kitchener, J. F. Vincent, *J. Mater. Sci.* **1987**, *22*, 1385.
- [32] L. Tombolato, E. E. Novitskaya, P.-Y. Chen, F. A. Sheppard, J. McKittrick, *Acta Biomater.* **2010**, *6*, 319.
- [33] K. Johnson, M. Trim, D. Francis, W. Whittington, J. Miller, C. Bennett, M. Horstemeyer, *Acta Biomater.* **2017**, *48*, 300.
- [34] W. Huang, A. Zaheri, W. Yang, D. Kisailus, R. O. Ritchie, H. Espinosa, J. McKittrick, *Adv. Funct. Mater.* **2019**, 1901077, <https://doi.org/10.1002/adfm.201901077>.
- [35] a) F.-J. Wortmann, H. Zahn, *Text. Res. J.* **1994**, *64*, 737; b) Y. Yu, W. Yang, B. Wang, M. A. Meyers, *Mater. Sci. Eng., C* **2017**, *73*, 152.
- [36] B. Chapman, *Text. Res. J.* **1969**, *39*, 1102.
- [37] M. Rinaudo, *Prog. Polym. Sci.* **2006**, *31*, 603.
- [38] a) P. K. Dutta, J. Dutta, V. S. Tripathi, *J. Sci. Ind. Res.* **2004**, *63*, 20; b) H. O. Fabritius, C. Sachs, P. R. Triguero, D. Raabe, *Adv. Mater.* **2009**, *21*, 391.
- [39] J. F. Vincent, U. G. Wegst, *Arthropod Struct. Dev.* **2004**, *33*, 187.
- [40] M. Kaya, M. Mujtaba, H. Ehrlich, A. M. Salaberria, T. Baran, C. T. Amemiya, R. Galli, L. Akyuz, I. Sargin, J. Labidi, *Carbohydr. Polym.* **2017**, *176*, 177.
- [41] T. Qu, D. Verma, M. Alucozai, V. Tomar, *Acta Biomater.* **2015**, *25*, 325.
- [42] S. Nikolov, H. Fabritius, M. Petrov, M. Friák, L. Lymperakis, C. Sachs, D. Raabe, J. Neugebauer, *J. Mech. Behav. Biomed. Mater.* **2011**, *4*, 129.
- [43] G. T. Beckham, M. F. Crowley, *J. Phys. Chem. B* **2011**, *115*, 4516.
- [44] a) P. Fratzl, *Curr. Opin. Colloid Interface Sci.* **2003**, *8*, 32; b) A. C. O'sullivan, *Cellulose* **1997**, *4*, 173.
- [45] R. Quesada Cabrera, F. Meersman, P. F. McMillan, V. Dmitriev, *Biomacromolecules* **2011**, *12*, 2178.
- [46] a) Y. Nishiyama, P. Langan, H. Chanzy, *J. Am. Chem. Soc.* **2002**, *124*, 9074; b) H. Zhu, S. Zhu, Z. Jia, S. Parvinian, Y. Li, O. Vaaland, L. Hu, T. Li, *Proc. Natl. Acad. Sci. USA* **2015**, *112*, 8971.
- [47] a) L. Li, C. Ortiz, *Nat. Mater.* **2014**, *13*, 501; b) L. Li, J. C. Weaver, C. Ortiz, *Nat. Commun.* **2015**, *6*, 6216; c) Y. A. Shin, S. Yin, X. Y. Li, S. B. Lee, S. M. Moon, J. W. Jeong, M. Kwon, S. J. Yoo, Y. M. Kim, T. Zhang, H. J. Gao, S. H. Oh, *Nat. Commun.* **2016**, *7*, 10772; d) Z. W. Huang, H. Z. Li, Z. L. Pan, Q. M. Wei, Y. J. Chao, X. D. Li, *Sci. Rep.* **2011**, *1*, 148.
- [48] H. D. Espinosa, J. E. Rim, F. Barthelat, M. J. Buehler, *Prog. Mater. Sci.* **2009**, *54*, 1059.
- [49] a) G. Subhash, S. Maiti, P. H. Geubelle, D. Ghosh, *J. Am. Ceram. Soc.* **2008**, *91*, 2777; b) M. Chen, J. W. McCauley, K. J. Hemker, *Science* **2003**, *299*, 1563; c) K. P. D. Lagerlöf, A. H. Heuer, J. Castaing, J. P. Rivière, T. E. Mitchell, *J. Am. Ceram. Soc.* **1994**, *77*, 385.
- [50] a) W. Pompe, H. Worch, W. J. Habraken, P. Simon, R. Kniep, H. Ehrlich, P. Paufler, *J. Mater. Chem. B* **2015**, *3*, 5318; b) P. Simon, D. Grüner, H. Worch, W. Pompe, H. Lichte, T. El Khassawna, C. Heiss, S. Wenisch, R. Kniep, *Sci. Rep.* **2018**, *8*, 13696.
- [51] S. Marković, L. Veselinović, M. J. Lukić, L. Karanović, I. Bračko, N. Ignjatović, D. Uskoković, *Biomed. Mater.* **2011**, *6*, 045005.
- [52] a) A. Zamiri, S. De, *J. Mech. Behav. Biomed. Mater.* **2011**, *4*, 146; b) B. Viswanath, R. Raghavan, U. Ramamurty, N. Ravishanker, *Scr. Mater.* **2007**, *57*, 361; c) S. Saber-Samandari, K. A. Gross, *Acta Biomater.* **2009**, *5*, 2206.
- [53] a) Q. Q. Wang, M. Nemoto, D. S. Li, J. C. Weaver, B. Weden, J. Stegemeier, K. N. Bozhilov, L. R. Wood, G. W. Milliron, C. S. Kim, E. DiMasi, D. Kisailus, *Adv. Funct. Mater.* **2013**, *23*, 2908; b) A. H. Barber, D. Lu, N. M. Pugno, *J. R. Soc., Interface* **2015**, *12*, 20141326; c) J. Aizenberg, J. C. Weaver, M. S. Thanawala, V. C. Sundar, D. E. Morse, P. Fratzl, *Science* **2005**, *309*, 275; d) H. Ehrlich, *Encyclopedia of Geobiology*, Springer, Berlin, Germany **2011**, p. 796.
- [54] B. Devouard, M. Posfai, X. Hua, D. A. Bazylinski, R. B. Frankel, P. R. Buseck, *Am. Mineral.* **1998**, *83*, 1387.
- [55] M. D. Moreno, K. Ma, J. Schoenung, L. P. Dávila, *Acta Biomater.* **2015**, *25*, 313.
- [56] a) M. Wysokowski, T. Jesionowski, H. Ehrlich, *Am. Mineral.* **2018**, *103*, 665; b) H. Ehrlich, R. Deutzmann, E. Brunner, E. Cappellini, H. Koon, C. Solazzo, Y. Yang, D. Ashford, J. Thomas-Oates, M. Lubeck, *Nat. Chem.* **2010**, *2*, 1084.
- [57] H. Ehrlich, D. Janussen, P. Simon, V. V. Bazhenov, N. P. Shapkin, C. Erler, M. Mertig, R. Born, S. Heinemann, T. Hanke, *J. Nanomater.* **2008**, *2008*, 54.
- [58] a) K. Shimizu, J. Cha, G. D. Stucky, D. E. Morse, *Proc. Natl. Acad. Sci. USA* **1998**, *95*, 6234; b) E. Brunner, P. Richthammer, H. Ehrlich, S. Paasch, P. Simon, S. Ueberlein, K. H. van Pée, *Angew. Chem., Int. Ed.* **2009**, *48*, 9724; c) H. Ehrlich, *Int. Geol. Rev.* **2010**, *52*, 661.
- [59] A. Woesz, J. C. Weaver, M. Kazanci, Y. Dauphin, J. Aizenberg, D. E. Morse, P. Fratzl, *J. Mater. Res.* **2006**, *21*, 2068.
- [60] a) H. Ehrlich, M. Motylenko, P. V. Sundareshwar, A. Ereskovsky, I. Zgobicka, T. Noga, T. Plocirski, M. V. Tsurkan, E. Wyroba, S. Suski, *Adv. Funct. Mater.* **2016**, *26*, 2503; b) H. Ehrlich, P. Simon, W. Carrillo-Cabrera, V. V. Bazhenov, J. P. Botting, M. Ilan, A. V. Ereskovsky, G. Muricy, H. Worch, A. Mensch, *Chem. Mater.* **2010**, *22*, 1462; c) H. Ehrlich, E. Brunner, P. Simon, V. V. Bazhenov, J. P. Botting, K. R. Tabachnick, A. Springer, K. Kummer, D. V. Vyalikh, S. L. Molodtsov, *Adv. Funct. Mater.* **2011**, *21*, 3473.
- [61] a) W. Yang, V. R. Sherman, B. Gludovatz, E. Schaible, P. Stewart, R. O. Ritchie, M. A. Meyers, *Nat. Commun.* **2015**, *6*, 6649; b) W. Yang, B. Gludovatz, E. A. Zimmermann, H. A. Bale, R. O. Ritchie, M. A. Meyers, *Acta Biomater.* **2013**, *9*, 5876; c) H. Quan, W. Yang, E. Schaible, R. O. Ritchie, M. A. Meyers, *Adv. Funct. Mater.* **2018**, *28*, 1804237; d) H. Gupta, S. Krauss, M. Kerschnitzki, A. Karunarathne, J. Dunlop, A. Barber, P. Boesecke, S. Funari, P. Fratzl, *J. Mech. Behav. Biomed. Mater.* **2013**, *28*, 366; e) S. Krauss, P. Fratzl, J. Seto, J. D. Currey, J. A. Estevez, S. S. Funari, H. S. Gupta, *Bone* **2009**, *44*, 1105.
- [62] E. A. Zimmermann, B. Gludovatz, E. Schaible, N. K. Dave, W. Yang, M. A. Meyers, R. O. Ritchie, *Nat. Commun.* **2013**, *4*, 2634.
- [63] F. Hang, A. H. Barber, *J. R. Soc., Interface* **2011**, *8*, 500.
- [64] a) M. A. Kasapi, J. M. Gosline, *J. Exp. Biol.* **1999**, *202*, 377; b) M. A. Kasapi, J. M. Gosline, *J. Exp. Biol.* **1997**, *200*, 1639.
- [65] A. Kitchener, *J. Zool.* **1987**, *213*, 621.
- [66] a) P. Fratzl, in *Learning from Nature How to Design New Implantable Biomaterials: From Biomineralization Fundamentals to Biomimetic Materials and Processing Routes* (Proceedings of the NATO Advanced Study Institute, held in Alvor, Algarve, Portugal, 13–24 October 2003), (Eds.: R. L. Reis, S. Weiner), Springer **2005**, pp. 15–34; b) J. Keckes, I. Burgert, K. Frühmann, M. Müller, K. Kölln, M. Hamilton, M. Burghammer, S. V. Roth, S. Stanzl-Tschegg, P. Fratzl, *Nat. Mater.* **2003**, *2*, 810.
- [67] P. Fratzl, R. Weinkamer, *Prog. Mater. Sci.* **2007**, *52*, 1263.
- [68] Y. Zhang, P. De Falco, Y. Wang, E. Barbieri, O. Paris, N. Terrill, G. Falkenberg, N. Pugno, H. Gupta, *Nanoscale* **2017**, *9*, 11249.
- [69] S. E. Naleway, M. M. Porter, J. McKittrick, M. A. Meyers, *Adv. Mater.* **2015**, *27*, 5455.
- [70] N. A. Yaraghi, N. Guarín-Zapata, L. K. Grunenfelder, E. Hintsala, S. Bhowmick, J. M. Hiller, M. Betts, E. L. Principe, J. Y. Jung, L. Sheppard, R. Wuhrer, J. McKittrick, P. D. Zavattieri, D. Kisailus, *Adv. Mater.* **2016**, *28*, 6835.
- [71] a) T. Sumitomo, H. Kakisawa, Y. Owaki, Y. Kagawa, *J. Mater. Res.* **2008**, *23*, 3213; b) X. D. Li, Z. H. Xu, R. Z. Wang, *Nano Lett.* **2006**, *6*, 2301.

- [72] a) R. Menig, M. H. Meyers, M. A. Meyers, K. S. Vecchio, *Acta Mater.* **2000**, *48*, 2383; b) H. D. Espinosa, A. L. Juster, F. J. Latourte, O. Y. Loh, D. Gregoire, P. D. Zavattieri, *Nat. Commun.* **2011**, *2*, 173.
- [73] G. Mayer, *Science* **2005**, *310*, 1144.
- [74] L. K. Grunenfelder, E. E. de Obaldia, Q. Q. Wang, D. S. Li, B. Weden, C. Salinas, R. Wuhrer, P. Zavattieri, D. Kisailus, *Adv. Funct. Mater.* **2014**, *24*, 6093.
- [75] a) D. Bajaj, D. D. Arola, *Biomaterials* **2009**, *30*, 4037; b) M. Yahyazadehfar, D. Bajaj, D. D. Arola, *Acta Biomater.* **2013**, *9*, 4806.
- [76] K. J. Koester, J. Ager III, R. Ritchie, *Nat. Mater.* **2008**, *7*, 672.
- [77] M. E. Launey, P.-Y. Chen, J. McKittrick, R. Ritchie, *Acta Biomater.* **2010**, *6*, 1505.
- [78] P.-Y. Chen, A. Stokes, J. McKittrick, *Acta Biomater.* **2009**, *5*, 693.
- [79] a) R. M. Kulin, P.-Y. Chen, F. Jiang, K. S. Vecchio, *Mater. Sci. Eng., C* **2011**, *31*, 1030; b) R. M. Kulin, P.-Y. Chen, F. Jiang, J. McKittrick, K. S. Vecchio, *JOM* **2010**, *62*, 41.
- [80] L. Szewciw, D. De Kerckhove, G. Grime, D. S. Fudge, *Proc. R. Soc. B: Biol. Sci.* **2010**, *277*, 2597.
- [81] B. Wang, T. N. Sullivan, A. Pissarenko, A. Zaheri, H. D. Espinosa, M. A. Meyers, *Adv. Mater.* **2018**, 1804574.
- [82] B. Wang, W. Yang, V. R. Sherman, M. A. Meyers, *Acta Biomater.* **2016**, *41*, 60.
- [83] P. Fratzl, H. S. Gupta, F. D. Fischer, O. Kolednik, *Adv. Mater.* **2007**, *19*, 2657.
- [84] S. Walter, B. Flinn, G. Mayer, *Acta Biomater.* **2007**, *3*, 377.
- [85] A. Lin, M. A. Meyers, *Mater. Sci. Eng., A* **2005**, *390*, 27.
- [86] M. J. Chon, M. Daly, B. Wang, X. Xiao, A. Zaheri, M. A. Meyers, H. D. Espinosa, *J. Mech. Behav. Biomed. Mater.* **2017**, *76*, 30.
- [87] J.-Y. Jung, S. E. Naleway, N. A. Yaraghi, S. Herrera, V. R. Sherman, E. A. Bushong, M. H. Ellisman, D. Kisailus, J. McKittrick, *Acta Biomater.* **2016**, *37*, 1.
- [88] X. Dong, N. Ruse, *J. Biomed. Mater. Res.* **2003**, *66A*, 103.
- [89] a) Parts of a tooth, including the enamel (cross section), [https://en.wikipedia.org/wiki/Tooth\\_enamel#/media/File:Blausen\\_0863\\_ToothAnatomy\\_02.png](https://en.wikipedia.org/wiki/Tooth_enamel#/media/File:Blausen_0863_ToothAnatomy_02.png) (accessed: June 2019); b) V. Imbeni, J. Kruzic, G. Marshall, S. Marshall, R. Ritchie, *Nat. Mater.* **2005**, *4*, 229.
- [90] a) W. Yang, S. E. Naleway, M. M. Porter, M. A. Meyers, J. McKittrick, *Acta Biomater.* **2015**, *23*, 1; b) B. Achrai, H. D. Wagner, *Acta Biomater.* **2013**, *9*, 5890.
- [91] N. Lee, L. N. Williams, S. Mun, H. Rhee, R. Prabhu, K. R. Bhattarai, M. Horstemeyer, *Biomed. Phys. Eng. Express* **2017**, *3*, 035025.
- [92] A. Drake, T. L. H. Donahue, M. Stansloski, K. Fox, B. B. Wheatley, S. W. Donahue, *Acta Biomater.* **2016**, *44*, 41.
- [93] L. K. Grunenfelder, G. Milliron, S. Herrera, I. Gallana, N. Yaraghi, N. Hughes, K. Evans-Lutterodt, P. Zavattieri, D. Kisailus, *Adv. Mater.* **2018**, *30*, 1705295.
- [94] M. J. Connors, H. Ehrlich, M. Hog, C. Godeffroy, S. Araya, I. Kallai, D. Gazit, M. Boyce, C. Ortiz, *J. Struct. Biol.* **2012**, *177*, 314.
- [95] W. Huang, W. Hongjamrassilp, J.-Y. Jung, P. A. Hastings, V. A. Lubarda, J. McKittrick, *Acta Biomater.* **2017**, *51*, 393.
- [96] a) M. M. Porter, E. Novitskaya, A. B. Castro-Ceseña, M. A. Meyers, J. McKittrick, *Acta Biomater.* **2013**, *9*, 6763; b) M. M. Porter, D. Adriaens, R. L. Hatton, M. A. Meyers, J. McKittrick, *Science* **2015**, *349*, aaa6683.
- [97] a) E. B. Tadmor, R. E. Miller, *Modeling Materials: Continuum, Atomistic and Multiscale Techniques*, Cambridge University Press, Cambridge, UK **2011**; b) S. Yip, *Handbook of Materials Modeling*, Springer Science & Business Media, Berlin, Germany **2007**.
- [98] M. J. Buehler, S. Ketten, T. Ackbarow, *Prog. Mater. Sci.* **2008**, *53*, 1101.
- [99] M. J. Buehler, *Atomistic Modeling of Materials Failure*, Springer Science & Business Media, Berlin, Germany **2008**.
- [100] a) A. K. Nair, A. Gautieri, S.-W. Chang, M. J. Buehler, *Nat. Commun.* **2013**, *4*, 1724; b) M. J. Buehler, *Proc. Natl. Acad. Sci. USA* **2006**, *103*, 12285; c) M. J. Buehler, *J. Mater. Res.* **2006**, *21*, 1947; d) M. J. Buehler, *J. Mech. Behav. Biomed. Mater.* **2008**, *1*, 59.
- [101] a) S. Ketten, M. J. Buehler, *Appl. Phys. Lett.* **2010**, *96*, 153701; b) S. Ketten, M. J. Buehler, *J. R. Soc., Interface* **2010**, *7*, 1709; c) A. Nova, S. Ketten, N. M. Pugno, A. Redaelli, M. J. Buehler, *Nano Lett.* **2010**, *10*, 2626.
- [102] S. Nikolov, M. Petrov, L. Lympirakis, M. Friák, C. Sachs, H. O. Fabritius, D. Raabe, J. Neugebauer, *Adv. Mater.* **2010**, *22*, 519.
- [103] a) R. Hambli, *Finite Elem. Anal. Des.* **2011**, *47*, 835; b) R. Hambli, H. Katerchi, C.-L. Benhamou, *Biomech. Model. Mechanobiol.* **2011**, *10*, 133; c) J. Ghanbari, R. Naghdabadi, *J. Biomech.* **2009**, *42*, 1560.
- [104] M. Shishhebor, P. D. Zavattieri, *J. Mech. Phys. Solids* **2019**, *124*, 871.
- [105] J. E. Rim, P. Zavattieri, A. Juster, H. D. Espinosa, *J. Mech. Behav. Biomed. Mater.* **2011**, *4*, 190.
- [106] E. E. de Obaldia, C. Jeong, L. K. Grunenfelder, D. Kisailus, P. Zavattieri, *J. Mech. Behav. Biomed. Mater.* **2015**, *48*, 70.
- [107] P. Zhang, M. A. Heyne, A. C. To, *J. Mech. Phys. Solids* **2015**, *83*, 285.
- [108] E. Lin, Y. Li, C. Ortiz, M. C. Boyce, *J. Mech. Phys. Solids* **2014**, *73*, 166.
- [109] a) N. Suksangpanya, N. A. Yaraghi, D. Kisailus, P. Zavattieri, *J. Mech. Behav. Biomed. Mater.* **2017**, *76*, 38; b) N. Suksangpanya, N. A. Yaraghi, R. B. Pipes, D. Kisailus, P. Zavattieri, *Int. J. Solids Struct.* **2018**, *150*, 83.
- [110] M. Moini, J. Olek, J. P. Youngblood, B. Magee, P. D. Zavattieri, *Adv. Mater.* **2018**, *30*, 1802123.
- [111] a) N. Abid, M. Mirkhalaf, F. Barthelat, *J. Mech. Phys. Solids* **2018**, *112*, 385; b) N. Abid, J. W. Pro, F. Barthelat, *J. Mech. Phys. Solids* **2019**, *124*, 350.
- [112] a) F. Barthelat, *J. Mech. Phys. Solids* **2014**, *73*, 22; b) H. Gao, *Int. J. Fract.* **2006**, *138*, 101.
- [113] a) A. R. Studart, *Adv. Mater.* **2012**, *24*, 5024; b) L. K. Grunenfelder, S. Herrera, D. Kisailus, *Small* **2014**, *10*, 3207.
- [114] a) P. Fratzl, *J. R. Soc., Interface* **2007**, *4*, 637; b) Z. Liu, Z. Zhang, R. O. Ritchie, *Adv. Mater.* **2018**, *30*, 1705220.
- [115] a) S. Deville, E. Saiz, R. K. Nalla, A. P. Tomsia, *Science* **2006**, *311*, 515; b) F. Bouville, E. Maire, S. Deville, *Langmuir* **2014**, *30*, 8656; c) M. C. Gutierrez, M. L. Ferrer, F. del Monte, *Chem. Mater.* **2008**, *20*, 634; d) S. Deville, E. Saiz, A. P. Tomsia, *Acta Mater.* **2007**, *55*, 1965; e) M. E. Launey, E. Munch, D. Alsem, H. Barth, E. Saiz, A. P. Tomsia, R. O. Ritchie, *Acta Mater.* **2009**, *57*, 2919; f) F. Bouville, E. Maire, S. Meille, B. Van de Moortèle, A. J. Stevenson, S. Deville, *Nat. Mater.* **2014**, *13*, 508; g) M. E. Launey, E. Munch, D. H. Alsem, E. Saiz, A. P. Tomsia, R. O. Ritchie, *J. R. Soc., Interface* **2010**, *7*, 741.
- [116] a) V. Naglieri, H. A. Bale, B. Gludovatz, A. P. Tomsia, R. O. Ritchie, *Acta Mater.* **2013**, *61*, 6948; b) M. M. Porter, R. Imperio, M. Wen, M. A. Meyers, J. McKittrick, *Adv. Funct. Mater.* **2014**, *24*, 1978; c) E. Munch, E. Saiz, A. P. Tomsia, S. Deville, *J. Am. Ceram. Soc.* **2009**, *92*, 1534; d) P. M. Hunger, A. E. Donius, U. G. Wegst, *Acta Biomater.* **2013**, *9*, 6338; e) K. L. Scotti, D. C. Dunand, *Prog. Mater. Sci.* **2018**, *94*, 243.
- [117] a) V. Naglieri, B. Gludovatz, A. P. Tomsia, R. O. Ritchie, *Acta Mater.* **2015**, *98*, 141; b) M. Zhang, D. Jiao, G. Tan, J. Zhang, S. Wang, J. Wang, Z. Liu, Z. Zhang, R. O. Ritchie, *ACS Appl. Nano Mater.* **2019**.
- [118] R.-f. Guo, P. Shen, C. Sun, Y. Wang, A. Shaga, Q.-c. Jiang, *Mater. Des.* **2016**, *106*, 446.
- [119] a) F. Song, Y. Bai, *J. Mater. Res.* **2003**, *18*, 1741; b) S. Xia, Z. Wang, H. Chen, W. Fu, J. Wang, Z. Li, L. Jiang, *ACS Nano* **2015**, *9*, 2167.
- [120] D. Raabe, C. Sachs, P. Romano, *Acta Mater.* **2005**, *53*, 4281.

- [121] M. M. Porter, M. Yeh, J. Strawson, T. Goehring, S. Lujan, P. Siripapasotorn, M. A. Meyers, J. McKittrick, *Mater. Sci. Eng., A* **2012**, *556*, 741.
- [122] M. B. Frank, S. E. Naleway, T. Haroush, C.-H. Liu, S. H. Siu, J. Ng, I. Torres, A. Ismail, K. Karandikar, M. M. Porter, *Mater. Sci. Eng., C* **2017**, *77*, 484.
- [123] M. M. Porter, L. Meraz, A. Calderon, H. Choi, A. Chouhan, L. Wang, M. A. Meyers, J. McKittrick, *Compos. Struct.* **2015**, *119*, 174.
- [124] Z. Cheng, K. Zhao, Z. Wu, *Ceram. Int.* **2015**, *41*, 8599.
- [125] Y. Zhang, L. Hu, J. Han, *J. Am. Ceram. Soc.* **2009**, *92*, 1874.
- [126] A. Preiss, B. Su, S. Collins, D. Simpson, *J. Eur. Ceram. Soc.* **2012**, *32*, 1575.
- [127] T. A. Ogden, M. Prsbrey, I. Nelson, B. Raeymaekers, S. E. Naleway, *Mater. Des.* **2019**, *164*, 107561.
- [128] H. Bai, A. Polini, B. Delattre, A. P. Tomsia, *Chem. Mater.* **2013**, *25*, 4551.
- [129] Q. Fu, M. N. Rahaman, F. Dogan, B. S. Bal, *Biomed. Mater.* **2008**, *3*, 025005.
- [130] P. Divakar, I. Caruso, K. L. Moodie, R. N. Theiler, P. J. Hoopes, U. G. Wegst, *MRS Adv.* **2018**, *3*, 1685.
- [131] P. Divakar, K. Yin, U. G. Wegst, *J. Mech. Behav. Biomed. Mater.* **2019**, *90*, 350.
- [132] S. E. Naleway, K. C. Fickas, Y. N. Maker, M. A. Meyers, J. McKittrick, *Mater. Sci. Eng., C* **2016**, *61*, 105.
- [133] S. Deville, *J. Mater. Res.* **2013**, *28*, 2202.
- [134] S. Deville, *Adv. Eng. Mater.* **2008**, *10*, 155.
- [135] a) R. M. Erb, H. S. Son, B. Samanta, V. M. Rotello, B. B. Yellen, *Nature* **2009**, *457*, 999; b) R. M. Erb, R. Libanori, N. Rothfuchs, A. R. Studart, *Science* **2012**, *335*, 199; c) M. Grossman, F. Bouville, F. Erni, K. Masania, R. Libanori, A. R. Studart, *Adv. Mater.* **2017**, *29*, 1605039; d) A. R. Studart, *Chem. Soc. Rev.* **2016**, *45*, 359.
- [136] H. Le Ferrand, F. Bouville, T. P. Niebel, A. R. Studart, *Nat. Mater.* **2015**, *14*, 1172.
- [137] H. Cho, J. C. Weaver, E. Pösel, P. J. in't Veld, M. C. Boyce, G. C. Rutledge, *Adv. Funct. Mater.* **2016**, *26*, 6938.
- [138] Y. L. Yap, C. Wang, S. L. Sing, V. Dikshit, W. Y. Yeong, J. Wei, *Precis. Eng.* **2017**, *50*, 275.
- [139] V. Slesarenko, S. Rudykh, *Int. J. Eng. Sci.* **2018**, *123*, 62.
- [140] a) J. R. Raney, J. A. Lewis, *MRS Bull.* **2015**, *40*, 943; b) F. P. Melchels, M. A. Domingos, T. J. Klein, J. Malda, P. J. Bartolo, D. W. Huttmacher, *Prog. Polym. Sci.* **2012**, *37*, 1079.
- [141] M. B. Frank, S. E. Naleway, T. S. Wirth, J.-Y. Jung, C. L. Cheung, F. B. Loera, S. Medina, K. N. Sato, J. R. Taylor, J. McKittrick, *J. Visualized Exp.* **2016**, *110*, e53554.
- [142] J. Y. Jung, A. Pissarenko, A. A. Trikanad, D. Restrepo, F. Y. Su, A. Marquez, D. Gonzalez, S. E. Naleway, P. Zavattieri, J. McKittrick, *Adv. Theory Simul.* **2019**, *2*, 1800152.
- [143] a) S. Rudykh, C. Ortiz, M. C. Boyce, *Soft Matter* **2015**, *11*, 2547; b) R. Martini, Y. Balit, F. Barthelat, *Acta Biomater.* **2017**, *55*, 360.
- [144] F. Libonati, G. X. Gu, Z. Qin, L. Vergani, M. J. Buehler, *Adv. Eng. Mater.* **2016**, *18*, 1354.
- [145] G. X. Gu, M. Takaffoli, A. J. Hsieh, M. J. Buehler, *Extreme Mech. Lett.* **2016**, *9*, 317.
- [146] G. X. Gu, F. Libonati, S. D. Wettermark, M. J. Buehler, *J. Mech. Behav. Biomed. Mater.* **2017**, *76*, 135.
- [147] G. X. Gu, M. Takaffoli, M. J. Buehler, *Adv. Mater.* **2017**, *29*, 1700060.
- [148] a) J. J. Martin, B. E. Fiore, R. M. Erb, *Nat. Commun.* **2015**, *6*, 8641; b) R. L. Truby, J. A. Lewis, *Nature* **2016**, *540*, 371.
- [149] a) S. M. M. Valashani, F. Barthelat, *Bioinspiration Biomimetics* **2015**, *10*, 026005; b) M. Mirkhalaf, A. K. Dastjerdi, F. Barthelat, *Nat. Commun.* **2014**, *5*, 3166.
- [150] Z. Yin, A. Dastjerdi, F. Barthelat, *Acta Biomater.* **2018**, *75*, 439.
- [151] I. A. Malik, F. Barthelat, *Int. J. Solids Struct.* **2016**, *97-98*, 389.
- [152] L. Grunenfelder, N. Suksangpanya, C. Salinas, G. Milliron, N. Yaraghi, S. Herrera, K. Evans-Lutterodt, S. Nutt, P. Zavattieri, D. Kisailus, *Acta Biomater.* **2014**, *10*, 3997.
- [153] S.-H. Yoon, S. Park, *Bioinspiration Biomimetics* **2011**, *6*, 016003.
- [154] a) W. Ching, P. Rulis, A. Misra, *Acta Biomater.* **2009**, *5*, 3067; b) V. Imbeni, R. Nalla, C. Bosi, J. Kinney, R. Ritchie, *J. Biomed. Mater. Res., Part A* **2003**, *66*, 1; c) E. A. Zimmermann, E. Schaible, B. Gludovatz, F. N. Schmidt, C. Riedel, M. Krause, E. Vettorazzi, C. Acevedo, M. Hahn, K. Püschel, *Sci. Rep.* **2016**, *6*, 21072.
- [155] F. L. Dri, X. Wu, R. J. Moon, A. Martini, P. D. Zavattieri, *Comput. Mater. Sci.* **2015**, *109*, 330.
- [156] M. M. Porter, J. McKittrick, M. A. Meyers, *JOM* **2013**, *65*, 720.
- [157] L. J. Gibson, M. F. Ashby, *Cellular Solids: Structure and Properties*, Cambridge University Press, Cambridge, UK **1999**.
- [158] H. Wei, N. A. Yaraghi, W. Yang, A. Velazquez-Olivera, Z. Li, R. O. Ritchie, D. Kisailus, S. M. Stover, J. McKittrick, *Acta Biomater.* **2019**, <https://doi.org/doi.org/10.1016/j.actbio.2019.04.003>.